

DYNAMICS AND REGULATION AT THE TIP  
A HIGH RESOLUTION VIEW ON MICROTUBULE ASSEMBLY



**Dynamics and regulation at the tip:  
A high resolution view on microtubule assembly**

PROEFSCHRIFT

ter verkrijging van  
de graad van Doctor aan de Universiteit Leiden,  
op gezag van de Rector Magnificus prof. mr. P. F. van der Heijden,  
volgens besluit van het College voor Promoties  
te verdedigen op dinsdag 24 juni 2008  
klokke 15.00 uur

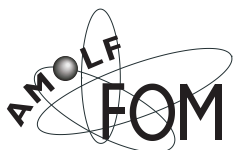
door

EMILIA LAURA MUNTEANU

geboren te Comănești, Romania  
in 1978

## Promotiecommissie

Promotor:	Prof. dr. M. Dogterom
Referent:	Prof. dr. K. Visscher (University of Arizona, Tucson, AZ)
Overige leden:	Prof. dr. J. P. Abrahams Dr. A. Akhmanova (Erasmus MC Rotterdam) Prof. dr. M. E. Janson (Wageningen University) Dr. ir. J. van Noort Prof. dr. J. M. van Ruitenbeek



© 2008 by Emilia Laura Munteanu. All rights reserved.

Nederlandse titel: Dynamica en regulatie aan de tip. Een hoge-resolutie-visie op de assemblage van microtubuli.

The work described in this thesis was performed at the FOM Institute for Atomic and Molecular Physics (AMOLF) in Amsterdam, The Netherlands. This work is part of the research programme of the 'Stichting voor Fundamenteel Onderzoek der Materie' (FOM), which is financially supported by the 'Nederlandse Organisatie voor Wetenschappelijk Onderzoek' (NWO).

Cover by Julien Husson.

ISBN: 978-90-77209-24-0

A digital version of this thesis can be obtained from <http://ub.leidenuniv.nl/>. Printed copies can be obtained by addressing the library at the FOM Institute for Atomic and Molecular Physics (AMOLF): [library@amolf.nl](mailto:library@amolf.nl); Kruislaan 407, 1098 SJ, Amsterdam, The Netherlands.

Printed in the Netherlands by Ponsen & Looijen BV graphical company, Wageningen.

This is the beginning of a beautiful friendship.

*Black Cat, White Cat*

**This thesis is partly based on the following articles:**

Kerssemakers JWJ, Munteanu EL, Laan L, Noetzel TL, Janson ME, Dogterom M (2006) Assembly dynamics of microtubules at molecular resolution. *Nature* **442**: 709-712 (chapter 2 and 3)

Bieling P, Laan L, Schek HT III, Munteanu EL, Sandblad L, Dogterom M, Brunner D, Surrey T (2007) Reconstitution of a microtubule plus-end tracking system *in vitro*. *Nature* **450**: 1100-1105 (chapter 4)

Munteanu EL, Laan L, Brunner D, Surrey T, Dogterom M. Regulation of microtubule dynamics, *in vitro*, by the autonomous microtubule-end tracker Mal3. *to be submitted* (chapter 5)

**Other articles:**

Laan L, Husson J, Munteanu EL, Kerssemakers JWJ, Dogterom M. (2008) Force generation and dynamic instability of microtubule bundles. *Proc Natl Acad Sci*: accepted

Dogterom M, Husson J, Laan L, Munteanu EL, Tischer C (2007) Microtubule forces and organization. In: Lenz P, editor, *Cell Motility*, Springer New York. pp. 93-115

Laan L, Munteanu EL, Kerssemakers JWJ, Dogterom M (2006) Meten aan microbuisjes met moleculaire resolutie. *Nederlands Tijdschrift voor Natuurkunde* **72**: 388-391

Tolic-Nørrelykke IM, Munteanu EL, Thon G, Oddershede L, Berg-Sørensen K (2004) Anomalous diffusion in living yeast cells. *Phys Rev Lett* **93**: 078102.1-4

---

# Contents

<b>1</b>	<b>Introduction</b>	<b>11</b>
1.1	Microtubules . . . . .	13
1.1.1	Structural features . . . . .	13
1.1.2	Dynamics . . . . .	15
1.1.3	Force generation . . . . .	18
1.2	Microtubule plus-end tracking proteins, +TIPs . . . . .	19
1.2.1	End-tracking mechanisms . . . . .	21
1.2.2	Regulation of microtubule dynamics . . . . .	24
1.3	This thesis . . . . .	24
<b>2</b>	<b>Measuring microtubule dynamics with near molecular resolution</b>	<b>27</b>
2.1	Experimental method . . . . .	28
2.2	'Keyhole' optical trap . . . . .	31
2.2.1	Optical tweezers set-up . . . . .	31
2.2.2	'Keyhole' trap design and features . . . . .	31
2.2.3	Determining the trap stiffness . . . . .	32
2.3	Experimental considerations . . . . .	33
2.3.1	Mechanics of microtubules under load . . . . .	33
2.3.2	Finite stiffness of the bead-axoneme construct . . . . .	34
2.4	Dynamic instability of microtubules measured with optical tweezers . . . . .	35
2.4.1	High-resolution details of microtubule dynamics . . . . .	35
2.4.2	Dynamics and force generation of multiple microtubules . . . . .	35
<b>3</b>	<b>Influence of XMAP215 on microtubule dynamics</b>	<b>39</b>
3.1	Microtubule assembly in the presence of XMAP215 . . . . .	40
3.1.1	XMAP215 enhances microtubule growth and catastrophes . . . . .	40
3.1.2	Assembly dynamics at molecular resolution . . . . .	41
3.2	Discussion . . . . .	46
3.3	Methods . . . . .	47
3.3.1	Measuring microtubule dynamics . . . . .	47
3.3.2	Step fitting algorithm . . . . .	50
3.4	XMAP215-tubulin interactions . . . . .	53

3.4.1	Speckled microtubules . . . . .	53
3.4.2	FCS measurements on XMAP215-tubulin complex formation . .	59
3.5	Additional remarks and discussion . . . . .	63
<b>4</b>	<b>Reconstitution of a microtubule plus-end tracking system <i>in vitro</i></b>	<b>67</b>
4.1	Results and discussion . . . . .	68
4.1.1	Mal3 recognizes and autonomously tracks microtubule growing ends . . . . .	70
4.1.2	Tea2 and Tip1 need each other and Mal3 for efficient plus-end tracking . . . . .	73
4.1.3	Mal3 acts as a loading factor for the Tea2-Tip1 complex . . . . .	77
4.1.4	Microtubule dynamics in the presence of Mal3, Tea2 and Tip1 . .	77
4.2	Conclusions . . . . .	78
4.3	Methods . . . . .	79
4.3.1	End-tracking assay using TIRF microscopy . . . . .	79
4.3.2	End-tracking assay using confocal microscopy . . . . .	80
4.3.3	+TIPs on static microtubules analyzed by confocal microscopy . .	81
4.3.4	DIC assay to measure microtubule dynamics . . . . .	81
<b>5</b>	<b>Microtubule dynamics in the presence of Mal3</b>	<b>83</b>
5.1	Introduction . . . . .	84
5.2	Results . . . . .	84
5.2.1	Mal3 enhances the dynamic instability of microtubules <i>in vitro</i> . .	84
5.2.2	Mal3 interacts differentially with the tip and with the lattice of growing microtubules. . . . .	87
5.2.3	Mal3 promotes formation of microtubule end-structures. . . . .	89
5.3	Discussion . . . . .	94
5.4	Additional remarks . . . . .	97
5.5	Experimental procedures and data analysis . . . . .	98
5.5.1	Measuring the parameters of microtubule dynamic instability by DIC microscopy. . . . .	98
5.5.2	Evaluating the amount of Mal3 bound on microtubules by confocal microscopy . . . . .	100
5.5.3	Microtubule end dynamics measured with optical tweezers . . .	104
<b>6</b>	<b>Microtubule catastrophes at molecular resolution</b>	<b>107</b>
6.1	Results . . . . .	108
6.1.1	Is there a molecular signature of catastrophes? . . . . .	109
6.1.2	Microtubule catastrophes in the presence of XMAP215 and Mal3	109
6.2	Discussion on the mechanism of catastrophes . . . . .	112



<b>7 Discussion and future directions</b>	<b>115</b>
7.1 Discussion . . . . .	115
7.2 Future directions . . . . .	117
7.2.1 Regulation of microtubule dynamics by the plus-end tracking complex Mal3-Tea2-Tip1 . . . . .	117
7.2.2 End-tracking of dynamic microtubules by EB proteins . . . . .	119
7.2.3 Influence of +TIPs on force generating microtubules . . . . .	120
<b>Bibliography</b>	<b>123</b>
<b>Summary</b>	<b>137</b>
<b>Samenvatting</b>	<b>141</b>
<b>Acknowledgements</b>	<b>145</b>
<b>Curriculum vitae</b>	<b>149</b>



---

## Introduction

*Fundamental processes like cell division, internal cell organization and intracellular transport rely on the proper functioning of microtubules. The microtubule cytoskeleton is a dynamic network of filaments that interact with and influence other cytoskeletal components (for example the actin network localization and organization). In turn, microtubule dynamics is highly regulated both spatially and temporally by a wide family of microtubule associated proteins. Microtubules have a complex architecture and dynamic behavior. To understand how microtubule associated proteins influence and regulate microtubule dynamics, information on the molecular mechanisms involved is required. Of special interest are a particular class of proteins that are specialized in tracking only the tips of the microtubules, the so called +TIPs. In this thesis, an *in vitro* approach was used in order to shed light on the molecular details of the microtubule self-assembly process itself, as well as the molecular mechanism by which selected microtubule associated proteins interact and influence microtubule dynamics.*

Tubulin [1–3], the protein that forms microtubules, is a highly conserved protein. It is perhaps the most ubiquitous throughout the eukaryotic kingdom and homologs can even be found in bacteria (FtsZ [4] and bacterial tubulins [5]). Tubulin self-assembles into hollow tubes, microtubules, in the presence of GTP both *in vivo* and *in vitro* [6]. *In vivo* microtubules form a dynamic array of filaments that confer structural support and shape to the cell, and are involved in intracellular organization and fundamental processes like division and transport. In most eukaryotic interphase cells, the microtubule cytoskeleton radiates from a nucleating center near the nucleus (the centrosome) forming a filament network with various morphologies (figure 1.1 left). Before mitosis this array is rapidly disassembled and reorganized to form the mitotic spindle (figure 1.1 right). This remarkable ability to switch between different morphologies relies on the intrinsic property of microtubules: dynamic instability [7]. Dynamic instability is the microtubule behavior of switching between periods of growth and shrinkage [8]. This property makes microtubules unique among polymers. Microtubule dynamics are highly regulated within cells in order to achieve specific functions at the right time and the right place within the cell. This coordinated regulation is done by a large network of microtubule associated proteins. Regulation occurs at all levels during a microtubule lifetime: tubulin monomer folding, microtubule nucleation, growth and shrinkage, and post translational modification of the microtubule lattice.

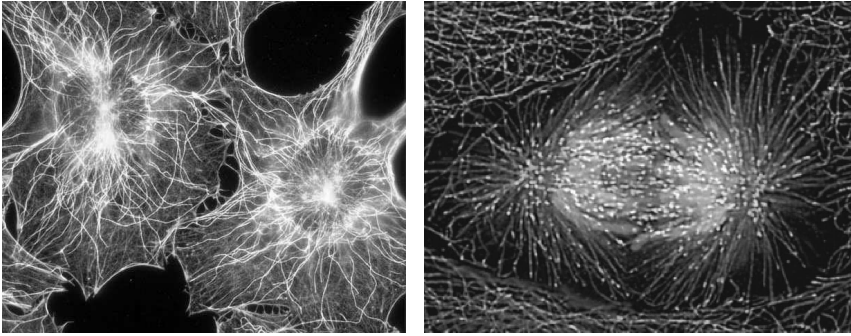


**Figure 1.1: Microtubule organization *in vivo*.** Left: interphase mouse fibroblasts cell displaying the aster like network of microtubules radiating from a nucleating center close to the nucleus. The fine network of actin filaments can also be observed throughout the cell. Right: a dividing kangaroo epithelial cell with the microtubules rearranged to form the mitotic spindle. The extra signal from the spindle region comes from the chromosomes. One major microtubule role in the spindle is to align the chromosomes and pull apart (this snapshot) the sister chromatids. The punctate pattern is due to the signal from EBI, an end binding protein that localizes at the growing microtubule ends. Images were acquired by Torsten Wittmann (images from <http://www.ucsf.edu/sciencecafe/2007/wittmann.html>).

Large effort is put into understanding the specific interactions between regulatory factors and microtubules. Malfunction in the regulation of microtubule dynamics results in erroneous mitosis and cell morphologies that are characteristic features in cancer and neurodegenerative diseases. It is established that the main players in microtubule regulation are microtubule associated proteins (MAPs) that function by targeting both soluble tubulin and microtubules [9–11]. Recent studies emphasized the importance of a special class of MAPs that are able to accumulate at and follow microtubule growing ends, the so called +TIPs [12–20]. Due to their specific localization at the microtubule tip, +TIPs have profound effects on the dynamics of the growing end. At the same time, +TIPs at microtubule ends could be delivered at specific locations in the cell or function as linkers to various cellular structures (e.g. the cell cortex or the kinetochores). Therefore, +TIPs are the main candidates to investigate when trying to understand microtubule regulation in cells. Current knowledge about +TIPs comprises important information about their function, the structure-function relationship and about the regulation of their activity [12, 21–24]. However, there is limited information about the end-tracking mechanism employed by individual +TIPs and the molecular mechanisms underlying their function. Also, +TIP influence on microtubule dynamics is usually inferred from experiments performed in living cells and in cell extracts, where it is hard to decouple the effect of other regulators. Recent *in vivo* and *in vitro* studies ([25–30] and work presented in this thesis) start to reveal the mechanisms of +TIP end-tracking and the regulation of microtubule dynamics by individual +TIPs. The advantage of an *in vitro* investigation is the minimal environment in which the influence of

various +TIPs can be dissected individually. The next logical step is to combine multiple +TIPs in order to reconstitute the *in vivo* microtubule dynamics and observe the collective effect of +TIPs.

This introductory part is focused on the the system we investigated: dynamic microtubules in the presence of associated proteins (XMAP215 and the fission yeast Mal3, Tea2 and Tip1). I will present the current state of knowledge and open questions about the self-assembly process of microtubules and about the molecular mechanism used by associated proteins to interact with microtubules and influence their dynamics. The work presented in this thesis is based on *in vitro* experiments, in a minimal environment. In these experiments, growing microtubules are sometimes subject to opposing forces. At the end I will discuss the questions that fueled the research contained in this thesis and the approach taken to answer them.

## 1.1 Microtubules

### 1.1.1 Structural features

**Microtubule architecture.** Microtubules are hollow tubes of 25 nm in diameter, made of parallel protofilaments that comprise  $\alpha\beta$ -tubulin heterodimers arranged in a head-to-tail fashion [31] (figure 1.2 a). *In vivo*, microtubules are typically comprised of 13 protofilaments, but *in vitro*, the protofilament number can vary from 9 to 17, even within the same microtubule [32, 33]. Tubulin dimers are arranged in a helical pattern within the microtubule wall, with a typical pitch of 1.5 the dimer size. The pitch results in a discontinuity in the lateral interactions, called the seam, where  $\alpha$ - and  $\beta$ -tubulin monomers neighbor each other (figure 1.2 a). At the seam, the lateral interactions between the adjacent protofilaments are therefore weaker and it was proposed that microtubules grow as protofilament sheets that zipper closed at the seam [34]. Recently it was also shown that the seam might have a functional role because an end-binding protein, fission yeast Mal3, specifically recognizes and binds the microtubule seam [25].

In cells, the microtubule lattice is subject to post-translational modification (PTM) that alters the surface properties [35]. The older the microtubules are, the more PTMs they accumulate. The modified lattice was shown to have an influence on the microtubule associated proteins: the plus-end-tracking protein CLIP-170 (cytoplasmic linker protein), known to stabilize microtubules by increasing rescues, is no longer properly localized on the modified microtubules [36]. Different kinesin motors are sensitive to specific PTMs and sometimes bind preferentially to the modified lattice [37], or, on the contrary, they have a lower affinity for microtubules [38].

**Microtubules have polarity.** Polarity is a feature of the microtubules derived from the intrinsic polarity of the tubulin heterodimer. The  $\beta$ -tubulin monomer is exposed at the dynamic and fast growing microtubule plus end, whereas  $\alpha$ -tubulin is exposed at the slower and less dynamic minus end (figure 1.2 a). In cells, minus ends are usually capped (by the nucleating templates in the centrosomal matrix) and are often non-

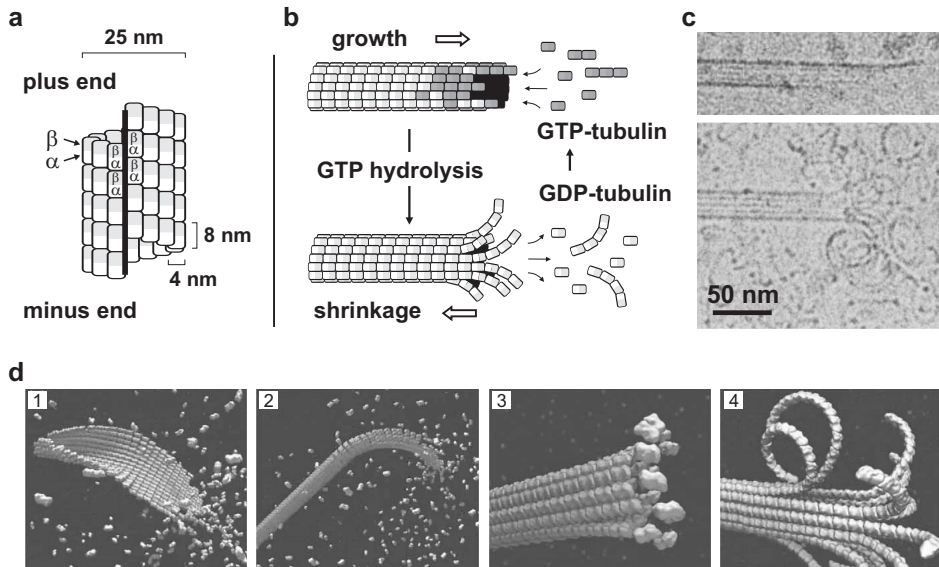


**Figure 1.2: Microtubule structure and dynamic instability.** (a) Schematic drawing of microtubule structure showing the arrangement of  $\alpha\beta$ -tubulin dimers within the lattice. The discontinuity marked by the thick black line represents the seam. (b) Schematic drawing of dynamic instability. GTP-tubulin assembles at the end of a microtubule forming a stabilizing structure that prevents microtubules from switching to a shrinking state. Upon assembly GTP is hydrolyzed. A catastrophe occurs when the stabilizing 'GTP cap' is lost (the molecular details of this process are not well understood). The cycle is completed by exchanging, upon depolymerization, the GDP of the tubulin subunits with GTP. (c) Electron microscopy images of what are believed to be growing (top) and shrinking (bottom) microtubules. Slightly outward curved sheet-like structures are often observed at the ends of growing microtubules. Shrinking microtubules are recognized by individual tightly-curved protofilaments peeling from the end. In addition, blunt ends are also observed and they are believed to represent an intermediate, the paused state of microtubules. Images adapted from [39]. (d) Artistic impression of structural intermediates of a dynamic microtubule: 1) nucleation starts by protofilament lateral association to form a sheet like structure that spontaneously closes into a cylinder. 2) A similar sheet intermediate forms at the ends of growing microtubule. 3) Loss of the GTP cap induces 4) rapid microtubule disassembly by protofilament peeling. Images adapted from [40].

dynamic. Microtubule plus ends radiate throughout the cell continuously exploring the cytoplasmic space while growing and shrinking. Microtubule polarity is exploited within the cell to create gradients by local accumulation of proteins or signaling agents: motor proteins such as kinesin and dynein follow the orientation of the microtubules and transport cargo either towards the plus end (to the cell periphery) or towards the minus end of the microtubules (to the cell interior). These motor proteins and their cargo can accumulate at the microtubule ends and be delivered at specific locations in the cell, for example when the microtubules come in contact with the cell membrane (see, for example, [41]).

**Microtubules are stiff polymers.** Due to their architecture microtubules are quite rigid polymers [42] conferring structural support and form to the cell. Microtubules have a persistence length  $l_p$  in the order of millimeters.  $l_p$  defines the length at which a filament displays significant bending due to thermal fluctuations. The persistence length,  $l_p$ , of a filament is related to its stiffness,  $\kappa$ :  $l_p = \kappa/k_B T$ , where  $k_B$  is Boltzmann's constant and  $T$  is the temperature ( $1 k_B T$  corresponds to 4.1 pN nm at room temperature). For microtubules  $\kappa \approx 25 \text{ pN } \mu\text{m}^2$ , although values measured in different studies vary over an order of magnitude. Recent work showed that short microtubules are easier to bend [43] and slow-growing microtubules are more stiff [44]. The length dependence was interpreted based on the complex architecture of the microtubules: shearing between adjacent protofilaments is non-negligible for short microtubules and contributes to their fluctuations [43, 45]. External factors could also affect stiffness. For example taxol-stabilized microtubules have lower stiffness [46] and it was suggested that MAPs increase microtubule rigidity [25, 46–48]. The matter, though, needs further investigation. It is clear that microtubules can not be seen as simple cylinders and that the details of the molecular lattice are important for their rigidity.

### 1.1.2 Dynamics

**Microtubule nucleation.** Microtubules are known to self-assemble from GTP-tubulin dimers. At high enough temperatures and tubulin concentrations, nucleation of new microtubules is a spontaneous process [49]. It has been proposed that nucleation starts with lateral association of short protofilaments to form a sheet, which spontaneously closes into a cylinder [50, 51] (figure 1.2 d-1). Below a critical concentration nucleation needs to be seeded by a nucleation site. In cells the soluble amount of tubulin is below critical concentration and microtubule nucleation is restricted primarily to  $\gamma$ -tuRC (tubulin ring complexes that include the  $\gamma$ -tubulin isoform and other stabilizing proteins) [52]. In *in vitro* experiments the typical nucleation sites are purified centrosomes, axonemes or short stabilized microtubules.

**Microtubule dynamic instability.** Dynamic microtubules switch stochastically between periods of assembly and disassembly [6]. This non-equilibrium behavior is known as dynamic instability [8]. Transition from a growing phase to rapid shortening is termed catastrophe and the reverse transition is called rescue. Figure 1.3 shows dynamic instability of a microtubule visualized with differential interference contrast (DIC) microscopy. Dynamic instability is best described by four parameters: growth speed ( $v_{\text{gro}}$ ), shrinkage speed ( $v_{\text{shr}}$ ) and the two transition frequencies ( $f_{\text{cat}}$  and  $f_{\text{res}}$ ).

$$v_{\text{gro}} = \delta(k_{\text{on}}c_{\text{tub}} - k_{\text{off}}) \quad (1.1)$$

$$v_{\text{shr}} = -\delta^* k_{\text{off}}^* \quad (1.2)$$

$$f_{\text{cat}} = N_{\text{cat}}/t_{\text{gro}} \quad (1.3)$$

$$f_{\text{res}} = N_{\text{res}}/t_{\text{shr}} \quad (1.4)$$

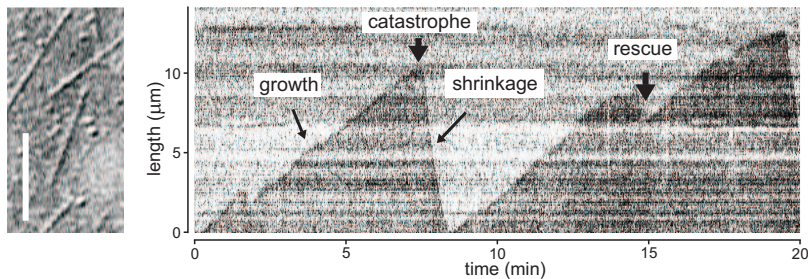


**Figure 1.3: Microtubule dynamic instability.** Left: Microtubules visualized by differential interference contrast (DIC) microscopy. Scale bar is  $5\mu\text{m}$ . Right: A kymograph (length vs time plot) showing microtubule length changes in time. The microtubule switches back and forth between periods of growth and shrinkage. One catastrophe (transition from growth to shrinkage) and a rescue (transition from shrinkage to growth) are indicated. The kymograph was constructed from a time sequence of DIC images by measuring in each frame the intensity profile along a chosen microtubule (automated in ImageJ). The microtubule was assembled in the presence of a microtubule associated protein, Mal3.

$\delta$  is the average microtubule length increase after one tubulin subunit incorporation. Because of the helical pattern of tubulin dimers within the microtubule wall for a 13 protofilament microtubule and single dimer addition, on average,  $\delta = 8/13$  nm. The growth speed depends on the soluble tubulin concentration ( $c_{\text{tub}}$ ) available for polymerization and on the rate constants for GTP-tubulin association ( $k_{\text{on}}$ ) and dissociation ( $k_{\text{off}}$ ) during net growth. The shrinkage speed is independent of tubulin concentration and it is characterized only by the dissociation rate of GDP-tubulin from the depolymerizing end ( $k_{\text{off}}^*$ ). Usually  $v_{\text{shr}}$  is an order of magnitude higher than  $v_{\text{gro}}$ . It is believed that shrinking is described by detachment of multiple subunits (oligomers) with average size  $\delta^*$ . The molecular details of tubulin addition and loss is still not fully understood. The catastrophe frequency is given by the number of catastrophes observed ( $N_{\text{cat}}$ ) during the total time growing microtubules were monitored ( $t_{\text{gro}}$ ). Rescues are defined in a similar way. The rescue rate of dynamic microtubules is extremely low *in vitro* and cannot be reliably measured. Only an upper bound can be estimated [53].

Dynamic microtubules have been directly observed by light microscopy both *in vivo* [54, 55] and *in vitro* [56, 57]. These studies show discrepancies in the measured dynamic instability parameters. Microtubule growth speed can be up to 10 times faster *in vivo* than *in vitro* and highly dynamic microtubules are a signature of mitosis. These observations reflect the regulation of microtubule dynamics by microtubule associated proteins.

**GTP hydrolysis fuels dynamics.** Microtubule dynamic instability is driven by binding, hydrolysis and exchange of GTP on the  $\beta$ -tubulin monomer [58] (figure 1.2 b). The following paradox exists: tubulin binds and hydrolyzes GTP, though there is no energy requirement for assembly of tubulin. Only GTP binding is required for tubulin assem-



bly. GTP hydrolysis takes place after a tubulin subunit has been incorporated into the lattice, tubulin acting as its own GTPase. Studies with a slow hydrolyzable GTP analogue, GMPCPP, demonstrated the role of GTP hydrolysis: it is essential for the dynamic behavior of microtubules, the switching between growth and shrinkage. The GMPCPP-microtubules continuously assembled without transitions to a shrinkage phase [59]. The disassembly of microtubules is a fast process that does not require energy and releases GDP-tubulin back to the soluble pool of tubulin. In solution, GDP can be exchanged for GTP and the tubulin dimer is thus reconverted into a polymerization competent subunit.

***Structural transitions associated with dynamics.*** It has been shown that GTP hydrolysis changes the conformation of the tubulin dimer from a slightly curved GTP-tubulin to a more kinked GDP-bound conformation [51]. Yet, in the microtubule lattice the GDP-tubulin dimer can not relax to its preferred curved conformation and is forced to remain straight. The free energy of the GTP hydrolysis is stored in the lattice as mechanical strain [60], which is released when the GDP-tubulin subunits are exposed at the microtubule end and provides the driving force for the rapid depolymerization phase of the dynamic instability. The straighter conformation of GTP-tubulin allows for lateral contacts between protofilaments and thus it is believed that a 'GTP cap' exists at the end of growing microtubules and stabilizes the labile microtubule lattice. Although generally accepted, the structural and biochemical details of a stabilizing cap at the microtubule growing end are still unclear. Figure 1.2 d-2 shows a possible microtubule end-structure, an open sheet of protofilaments extending while the microtubule is growing. When the GTP cap is stochastically lost (due to detachment of GTP-tubulin subunits at the end and by GTP hydrolysis catching up with addition of new subunits) (figure 1.2 d-3), the protofilaments peel outwards and the microtubule lattice collapses by rapid depolymerization (figure 1.2 d-4). This scenario is supported by the observation from electron microscopy studies that revealed the structural difference between growing and shrinking microtubule ends [34, 39] (figure 1.2 c). Growing microtubules often terminate in sheet-like structures of laterally connected protofilaments that appear to slightly bend outwards, corresponding to GTP-tubulin. At the end of shrinking microtubules individual protofilaments curl outward more strongly indicating the conformational change of GDP-tubulin. What exactly are the molecular events that trigger the switching between growing and shrinking states (catastrophes and rescues), remains poorly understood. Recent models and computer simulations based on the energetics of tubulin-tubulin bonds and the elastic properties of tubulin protofilaments are able to reproduce the growing and shrinking phases of microtubules [61–63]. They also predict a metastable intermediate state, which suggests a mechanism for rescue [61, 63] and that the GTP-cap can be composed of only a couple of GTP-tubulin subunits [62, 63].

The differences in the tubulin conformation at the growing end, shrinking end, and within the microtubule lattice could be seen as a fine-tuned mechanism of regulating

interactions with microtubule associated proteins (MAPs). MAPs could directly detect and make use of structural differences in the microtubule growing or shrinking state, a possible mechanism employed by +TIPs that recognize and follow microtubule growing ends (discussed below in section 1.2.1).

**Regulation of microtubule dynamics.** Many cellular functions of microtubules require that their dynamic properties are precisely controlled. The regulation is primarily done by MAPs. How could MAPs change microtubule dynamic instability parameters? If we look at equations 1.1-1.4 there are several options. Enhanced growth speed could be achieved by i) a biochemical increase in the affinity of tubulin association rate ( $k_{\text{on}}$ ). The MAP could either bind first at the microtubule tip or form a tubulin-MAP complex in solution. ii) Increasing the added subunit size ( $\delta$ ) would also result in faster growth. This implies that MAPs would be capable of templating formation of oligomers that subsequently are incorporated at the growing microtubule end. There are experimental studies indicating that XMAP215/TOGp [64, 65] and CLIP-170 [29, 66, 67] could bind and induce formation of tubulin oligomers *in vitro*. XMAP215 and the budding yeast homologue Stu2 were also shown to destabilize microtubules [68, 69]. It is possible that a protein like XMAP215 increases both rates of tubulin association ( $k_{\text{on}}$ ) and dissociation ( $k_{\text{off}}$ ). Depending on the exact conditions (temperature, salt, tubulin concentration) the protein can accelerate growth or, on the contrary, enhance tubulin dissociation that could result in, for example, more frequent catastrophes. It is less obvious how MAPs could increase or reduce  $k_{\text{off}}^*$ , the dissociation rate of tubulin from a depolymerizing end. Most probably there is a correlation with the lattice stability and the interaction between protofilaments. Also the transition frequencies might depend on the stability of the lateral interactions between protofilaments and on the details of tubulin association and dissociation. We still miss information about the molecular details accompanying regulation of microtubule dynamics by MAPs. The research presented in this thesis includes new insights into the molecular mechanism of microtubule dynamics influence by two MAPs: XMAP215, known to dramatically enhance growth speed (chapter 3) and Mal3, a microtubule end-binding protein, known to have an important role in maintaining microtubule stability within cells (chapter 5).

### 1.1.3 Force generation

Several studies show that microtubules can produce both pushing and pulling forces [70, 71]. On one hand, during microtubule polymerization, the free energy gain associated with addition of tubulin subunits is sufficient to generate a force of several tens of piconewton. On the other hand, the mechanical strain stored in the GDP-lattice can fuel pulling forces on a target coupled to shrinking microtubule ends. Microtubules can thus perform mechanical work [72, 73] and drive intra-cellular movement of organelles. A well known example is chromosome separation during anaphase in dividing cells, which is partly powered by depolymerization of kinetochore-attached microtubules [74]. Also, microtubule growth generates forces that help position organelles

and microtubule organizing centers within the cell [75]. The biophysical aspects of microtubule force generation have been studied in experimental [70, 76, 77] and theoretical [78–80] work by several groups.

The simplest mechanistic way to think about force generation by growing microtubules is provided by the Brownian ratchet model [81]. In this model, thermal fluctuations of a confining barrier allow for occasional addition of new subunits to a growing filament. The filament can grow even in the presence of an opposing external force. Since the amplitude of the fluctuations reduces as the force increases, the rate at which new subunits can insert slows down. The force at which no net growth occurs anymore and subunits only occasionally detach is defined as the stall force. The Brownian ratchet predicts an exponential dependence of the filament growth rate on the applied force ( $F$ ):

$$v_{\text{gro}}(F) = \delta(k_{\text{on}}c_{\text{tub}}e^{-F\delta/k_{\text{B}}T} - k_{\text{off}}) \quad (1.5)$$

For microtubules, more elaborate models accounting for multiple filaments predict a slightly different force-velocity curve, whose functional details depend on the assumed structure of the growing microtubule end [78–80].

Microtubule growth is influenced by force in the crowded intracellular environment. In the cell, microtubules often grow against obstacles like organelles, membranes and the cell cortex. In mitosis, microtubules push and pull chromosomes in order to align and separate them. There is still a lack of quantitative knowledge about the magnitude of these forces. A recent study analyzed the shapes of bent microtubules in the cell and concluded that microtubules can withstand much higher loads than expected from *in vitro* studies [82]. The authors explain this discrepancy by microtubule mechanical reinforcement from the surrounding elastic cytoskeleton [82, 83]. Although not studied from this perspective, the microtubule end-binding proteins that decorate the tips of growing microtubules could also influence microtubule stability under force. There is still an open question: do MAPs regulate the force generation of microtubules and if so, what is the molecular mechanism underlying this regulation?

## 1.2 Microtubule plus-end tracking proteins, +TIPs

*In vivo*, the regulation of microtubule dynamics is largely the responsibility of microtubule associated proteins (MAPs) [9–11]. As their name says, the shared feature is the affinity for tubulin and microtubules. Their activity covers a wide range of regulation. There are MAPs that control microtubule nucleation and microtubule bundle organization. MAPs, like Op18/stathmin, have been proposed to sequester soluble tubulin [84, 85]. Classical MAPs such as tau and MAP2 bind to the microtubule lattice and stabilize it, but other lattice binding MAPs have the opposite effect (e.g. the severing protein katanin [86]). Microtubule associated motors are a class of MAPs that have the ability to walk along the microtubules (kinesins and dyneins). Motor proteins transport

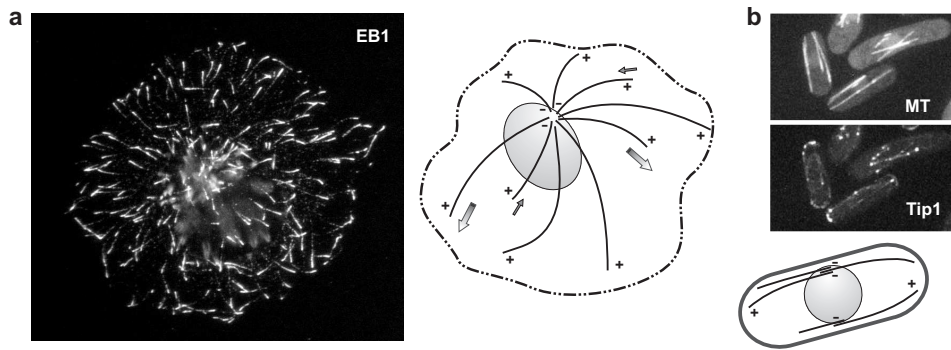


**Figure 1.4: Plus-end tracking proteins, +TIPs.** (a) Fluorescent comets of EB1, a mammalian plus end-binding protein, at the growing microtubule ends in an interphase COS-7 cell. The cell shows immunofluorescence staining of endogenous EB1. Image courtesy of Anna Akhmanova. Right: Schematic drawing of microtubule organization in a similar fibroblast cell in interphase. Dynamic microtubule plus ends radiate towards cell periphery. +TIPs, like EB1, are able to specifically localize at the growing plus ends. (b) Fluorescence images of microtubules (top image) and Tip1-GFP decorating the microtubule plus ends (lower image) in fission yeast cells. Tubulin was tagged with mCherry. Images courtesy of Christian Tischer. Below: Schematic drawing of microtubule organization in an interphase fission yeast cell. Microtubules are organized in parallel bundles and grow with the plus ends towards the cell poles.

and deliver material throughout the cell [87,88], they are involved in maintaining the integrity and function of microtubule bundles, for example, in the mitotic spindle [89] or in the beating flagella. Motors can anchor microtubules at the cell cortex [90] or to kinetochores [91], and by themselves can influence the stability of microtubules [92–95].

An important class of MAPs are the end-binding proteins, generally termed +TIPs [12–20], including both microtubule associated motors and non-motor proteins. Their distinguishing feature is the microtubule end localization (figure 1.4). When marked with a fluorescent tag, the +TIPs appear as comets at microtubule tips moving throughout the cell as the microtubules are growing. Some +TIPs also have the ability to follow the shrinking microtubule ends.

The +TIPs most obvious function is the regulation of microtubule plus-end dynamics, where tubulin is incorporated and forms the stabilizing cap. 'Traveling' on microtubule ends provides a mechanism for cargo delivery at specific locations in the cell. An emerging role for +TIPs is in cell motility and polarized cell growth where signals are delivered to the cortex to control actin assembly, organization and contractility (one example can be found in fission yeast [96]). A scenario for protein delivery at the cell periphery would require the combined effect of several +TIPs: stabilization of the growing end such that the microtubules reach the target and continuous presence of the cargo at the plus end. As a consequence the +TIPs form a highly interactive protein network where several +TIPs act together to achieve one function [12, 21, 24]. Some +TIPs can

directly interact with membrane proteins, actin associated proteins and kinetochore proteins and thus provide coupling between microtubules and other cellular components [14, 24]. For example, EB1, a microtubule plus-end-tracking protein, interacts with a transmembrane protein STIM1, which is localized to the endoplasmic reticulum (ER) (membranous network within cells). EB1-STIM1 interaction mediates ER remodeling by coupling the dynamic microtubule plus-ends to the ER membrane [97]. Some of the coupling +TIPs have been proposed to transduce the pulling forces generated by the microtubule disassembly during chromosome segregation. A peculiar example of force coupling through a +TIP is the alignment and positioning of the mitotic spindle in the budding yeast [98]. In this example the +TIP is dynein, a minus end directed motor. Here, the force is produced by both the +TIP motor tracking the shrinking microtubule ends and by disassembly of microtubules. The force generated results in spindle motion through coupling of dynein to the cell cortex.

### 1.2.1 End-tracking mechanisms

Structural and cellular studies together with recent *in vitro* experiments (including part of the work presented in this thesis) start to unravel the molecular mechanisms of plus-end localization. Possible mechanisms are described below.

**Copolymerization** implies that a +TIP is incorporated together with tubulin at the growing microtubule end (figure 1.5-1). There are some requirements in order to get tip tracking through copolymerization. The +TIP should have high affinity for soluble tubulin to form relatively stable complexes with tubulin in solution. +TIP affinity for the microtubule lattice should be low. Upon end incorporation the +TIP releases from the older parts of the filament by stochastic detaching or induced by a conformational (straightening of protofilaments) and/or biochemical (GTP hydrolysis) change. Modification of +TIP affinity for the microtubule by other proteins is also possible. In the copolymerization scenario the +TIP would appear stationary on the microtubule while the end elongates. After a delay, the +TIP would then release its fixed point on the microtubule. As defined above, the copolymerizing +TIPs would only follow growing microtubules.

Among +TIPs, CLIP-170 was shown to bind tubulin *in vitro* and copolymerization was suggested to be a likely mechanism of CLIP-170 end-tracking [29, 66, 67]. This conclusion was recently challenged in a study showing rapid turnover of the protein at microtubule ends *in vivo* [30]. The underlying mechanism of CLIP-170 end-tracking was suggested to be, therefore, a tip recognition mechanism.

**Tip recognition** requires the existence of a specific structure at the growing microtubule end that is recognized by +TIPs (figure 1.5-2). Cryo-EM studies show the existence of slightly curved protofilaments at the ends of growing microtubules. Further, GTP-tubulin is assembled at the tip, while GDP-tubulin represents the majority within the microtubule lattice. The structural and biochemical details of the microtubule end-structure remain to be clarified. Assuming the existence of such a struc-

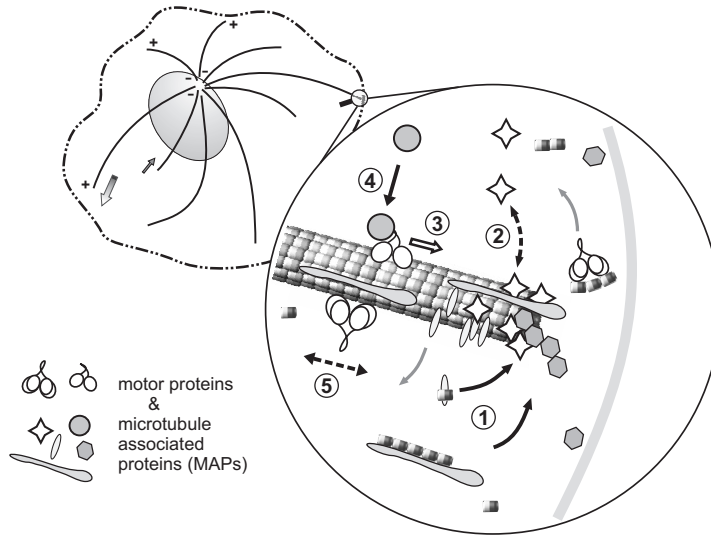


**Figure 1.5: Microtubule end-tracking mechanisms.** Cartoon of a cell with dynamic microtubules radiating from the centrosome. The enlarged image gives an artistic impression of the complex interactions at the growing microtubule plus-end. Specialized proteins, so called +TIPs, can bind and track dynamic microtubule ends, where they control microtubule dynamics, deliver cargo or mediate interactions with the cell cortex. Possible end-tracking mechanism of +TIPs include: (1) copolymerization with tubulin and later detachment from the microtubule lattice, (2) specific end-structure recognition, (3) direct movement of kinesins and dyneins, (4) hitchhiking on other motor or non-motor +TIPs already present at the tip, and (5) 1-D diffusion on the lattice to facilitate end-finding.

ture, +TIPs could recognize either the presence of GTP-tubulin, specific protofilament arrangement, protofilament curvature and/or might bind to exposed tubulin sites otherwise hidden in the rest of the tube. Also, the +TIPs should not prevent the progressive conversion of the end structure into a regular lattice conformation (a closed tube). The GTP-cap was predicted to be quite small ( $< 0.5 \mu\text{m}$ ) [56, 99–101], while in cells +TIP comets are in general covering a more extended area ( $0.5\text{--}2 \mu\text{m}$ ). However, biochemical recognition of the tip cannot be excluded as the GTP-cap size prediction is based on limited experimental evidence. A structural recognition of the growing end by EB proteins is supported by a recent electron microscopy study of Mal3 [25]. Mal3, the fission yeast EB homologue, showed specific binding at the microtubule seam. At the seam, the lateral interactions between adjacent protofilaments are different than elsewhere in the lattice. It is possible that the EB binding sites of tubulin are only available at the seam. A similar picture can be envisioned at the growing end. An open structure of protofilaments could provide exposed EB binding sites. Experimental results presented in chapter 4 and chapter 5 bring new information about the molecular mechanism of Mal3 end-tracking.

Some +TIPs are able to follow shrinking microtubules, commonly known as backtracking. In this case, the proteins would recognize the highly curved protofilaments observed at the ends of disassembling microtubules. The budding yeast Bik1 (CLIP-170 homologue) and kinesin Kip2 were observed to follow shrinking microtubules [102]. The backtracking of Bik1 was dependent on the kinesin Kip2 that seems to transport Bik1 to the plus end. It is possible that the two yeast +TIPs together or independently recognize the curved disassembling protofilaments. Future experimental investigations are needed to fully understand the mechanism of Bik1 and Kip2 backtracking.

**Directed motion** is a potential end-tracking mechanism used by motors, provided that the motors walk faster than the microtubules grow (figure 1.5-3). A simple explanation for motor accumulation at the tip could be that newly formed parts of the microtubule 'receive' motors both from solution and from the older lattice. The extent of the end accumulation would depend on the run length of individual motors. Some of the kinesins, like the fission yeast Tea2 [103], are known to end-track growing microtubules. It is not yet established if their directed movement is solely responsible for their end-tracking behavior. It is possible that once reaching the ends, these motors are retained due to specific affinity for the end-structure or by interaction with other +TIPs already present there. A motor dependent end-tracking mechanism does not exclude tracking of shrinking ends. The protein directed motion would be sufficient to produce accumulation. The Kip2 kinesin shows backtracking in budding yeast, but the molecular mechanism has not yet been investigated.

**Hitchhiking** by association with motors and other microtubule end-binding proteins seems to be common for many +TIPs [17] (figure 1.5-4). This type of mechanism involves an intermediate protein at the microtubule tip, implying that hitchhikers do not efficiently interact with tubulin or microtubules. Several +TIPs were proposed to be transported as cargo to the growing microtubule ends. For example, the yeast homologs from the CLIP family, Bik1 and Tip1, are moved processively by the Kip2 and Tea2 kinesin, respectively [102, 103]. STIM1 is another example of hitchhiker that is involved in linking the ER membrane to microtubule tips by direct binding to EB1 [97].

**1-D diffusion** on microtubules is common for nonprocessive motors or proteins that have weak affinity for the microtubule lattice. Affinity for the microtubule will target these MAPs to the lattice where they diffuse for a short period exploring the 1-D space (figure 1.5-5). If they land close to the tip they might accumulate at the microtubule end but only through another mechanism (tip recognition or interaction with other +TIPs). 1-D diffusion is therefore not per se an end-tracking mechanism. It can rather be seen as a microtubule-end targeting mechanism employed by proteins that do not use active motion. The kinesin-13 MCAK was shown to target microtubule ends by lattice diffusion [26], together with recognition of the protofilament curvature at the microtubule tips.

One common feature of the end-tracking mechanisms is that +TIPs are transiently present at the microtubule end. Interaction with the tip is dynamic and new proteins

from solution are constantly repopulating the tip. The majority of +TIPs have low affinity for tubulin in solution and most +TIPs are dimers (EBs, CLIPs, tip tracking kinesins) or have multiple binding sites for tubulin indicating that cooperativity might be necessary for end-tracking [21]. Some interactions within the +TIP network seem to be based on similar amino acid motifs as some +TIP-tubulin interactions [104, 105]. The competition raised by this similarity could prevent overcrowding at the microtubule tip and, more importantly, could induce sequential recruitment of +TIPs at the microtubule end.

### 1.2.2 Regulation of microtubule dynamics

+TIPs in general promote microtubule growth and/or enhance the dynamic behavior of microtubules. The first +TIP discovered, CLIP-170, was found to stabilize microtubule growth. CLIP-170 functions as a rescue factor [106] and the fission yeast homologue, Tip1, suppresses microtubule catastrophes [107, 108]. The mechanism of rescuing shrinking microtubules remains puzzling as CLIP-170 does not seem to bind the depolymerizing ends. The EB (end binding) family members are also known as stabilizers. EB proteins were reported to suppress catastrophes in fission yeast [109] and in *Xenopus* egg extracts [110]. In extract experiments, stabilization of microtubules was achieved also by EB1 increasing the rescue rate. *In vitro* experiments supported the idea that the EBs promote polymerization [25, 111, 112], but might depend on the presence of other +TIPs [111]. On the other hand, in budding yeast [113] and *Drosophila* [114], EB1 enhances both the catastrophe and the rescue rate. However, it remains unclear if EBs can modulate microtubule dynamics on their own and if the *in vivo* effects can be attributed solely to the EB proteins. Among the destabilizers are kinesin-8 (Kip3 [115, 116]), kinesin-13 (MCAK [117], KLP10A [118]) and kinesin-14 (Kar3 [119]) family members that are known to catalyze microtubule depolymerization. One possible mechanism is based on structural changes at the microtubule tip where these kinesins can force protofilaments into a more bent conformation.

## 1.3 This thesis

The work presented in this thesis concerns the regulation of microtubule dynamics by microtubule associated proteins. Our effort was directed towards understanding the molecular mechanisms underlying this regulation. We chose to investigate a number of representative MAPs, individually, *in vitro*. The advantage of an *in vitro* minimal system is the possibility it offers to uncouple the regulation of different MAPs. If desired, the level of complexity can be increased by introducing a combination of MAPs.

In order to achieve molecular resolution on the microtubule assembly process, we developed a high resolution technique based on optical tweezers. Chapter 2 contains a detailed description of the technique. Dynamic microtubules could be followed with unprecedented resolution of a few nanometers and allowed us to zoom in on micro-



tubule assembly process. In chapter 3, molecular details of microtubule growth are discussed and how this process is altered, on a molecular scale, by the microtubule associated protein XMAP215. XMAP215, a *Xenopus* MAP, attracted our attention due to its effect on microtubule assembly, XMAP215 being probably the most potent microtubule growth enhancer known [120]. Previous *in vitro* experiments showed that XMAP215 sped up microtubule growth up to 10-fold [121, 122], similar with its behavior *in vivo*. Using our high-resolution technique we observed fast length changes during microtubule growth, that correspond to the size of the XMAP215 protein itself. The implications of this new finding are discussed. Triggered by the observations at high-resolution, we further attempted to investigate XMAP215-tubulin interactions in solution and the possibility that XMAP215 templates formation of tubulin oligomers (XMAP215 could bind multiple tubulin dimers along its length [64, 123]). Our observations using two independent techniques, fluorescence speckle microscopy and fluorescence correlation spectroscopy, are presented and discussed.

Chapters 4 and 5 present experiments related to a set of end-tracking proteins, namely three fission yeast +TIPs: the EB1 homologue Mal3, the kinesin Tea2 and the CLIP-170 homologue Tip1. These +TIPs were shown to have an important role in regulating microtubule dynamics *in vivo*. However, due to lack of *in vitro* investigations, it is not clear if EBs, for example, can regulate microtubule dynamics independently or if they only modulate the influence of other +TIPs. First *in vitro* reconstitution of microtubule plus-end tracking by the three fission yeast +TIP system is presented in chapter 4. We found experimental evidence for the molecular mechanisms utilized by the three proteins, individually and together, to specifically end-track microtubule growing ends [124]. Among the three +TIPs only Mal3 was able to autonomously end-track microtubule growing ends. Tea2 and Tip1 needed each other and Mal3 to end-track. As Mal3 is able to localize at microtubule growing ends on its own, it is possible that the EB1 homologue has also an effect on microtubule dynamics. Chapter 5 contains our results on Mal3 regulation of microtubule dynamics *in vitro*. The experimental work includes quantification of microtubule dynamic instability parameters by light microscopy, quantification of Mal3 localization on microtubules by fluorescence microscopy, and investigation with the optical tweezers based technique of the modifications induced by Mal3 at the microtubule dynamic tip. The sole presence of Mal3 induced a surprising and complex effect on microtubule dynamics. Combining results from the three independent techniques, we propose a mechanism of Mal3-regulation.

Chapter 6 focuses on microtubule catastrophes, the transitions from a growing to a shrinkage phase. Knowledge about a mechanism for catastrophes has been limited to models based on structural details of the microtubule ends imaged with cryo electron-microscopy. Information about how MAPs act on a molecular level to regulate catastrophes is even less extensive. Using our optical tweezers based technique we followed dynamic microtubule ends with near molecular resolution. When zooming in at the events just before microtubule fast disassembly, we observed a slow decrease in micro-

tubule length of several tens of nanometers. Our observations suggest that catastrophes are represented by loss of the stabilizing end-structure or a conformational change at the microtubule tip. The influence of XMAP215 and Mal3 on the molecular details preceding fast depolymerization were also investigated. First observations are presented.

Chapter 7 includes a general discussion of the results comprised in this thesis and future directions of investigation:

(i) From the *in vitro* end-tracking experiment we found that Tea2 and Tip1 need Mal3 to localize at the plus end. It is possible that the presence of Tea2 and Tip1, individually or in combination, at the microtubule tip affect Mal3-induced regulation. Preliminary experiments were done to assess the interplay between the two +TIPs (Tea2 and Tip1) and Mal3 and their combined regulation of microtubule dynamics.

(ii) Mal3 is the fission yeast homologue of mammalian EB proteins. The high sequence homology between Mal3 and EB1/EB3 would suggest a similar behavior of the three proteins on microtubules, but *in vivo* studies indicated that EB1 effect on microtubule dynamics might depend on the presence of another +TIP, the dynactin component p150<sup>Glued</sup> [125]. First *in vitro* reconstitution of the EB3 end-tracking is presented. Fluorescently tagged EB3 autonomously end-tracked growing microtubules, similarly with Mal3, but also showed an intriguing interaction with the microtubule lattice at high concentrations.

(iii) An important aspect of microtubule dynamics is regulation by force. This effect has relevance for the intracellular crowded environment where microtubules often encounter barriers. The presence of MAPs might affect the behavior of microtubules growing against force. Our high-resolution technique involves optical tweezers allowing for quantification of the force generation by growing microtubules. The first observations of microtubule force generation in the presence of XMAP215 and Mal3 are presented.

---

## Measuring microtubule dynamics with near molecular resolution

*To gain insight into the molecular mechanism of microtubule self-assembly process and its regulation by MAPs we developed a high resolution technique that allows us to follow dynamic microtubules with near molecular resolution in vitro. The technique combines optical tweezers, microfabricated rigid barriers and high-resolution video tracking of microbeads. The experimental method, the special features of the optical trap and considerations regarding microtubules in the context of our set-up are presented. The unprecedented resolution provided by our technique allowed us to observe details of growth and shrinkage of dynamic microtubules.*

Microtubule self-assembly process is a dynamic, complex phenomenon. Another level of complexity is added by the fact that microtubule dynamics is regulated by physical (force) and cellular (microtubule associated proteins) factors. Our understanding of both microtubule dynamic instability and influence of microtubule associated proteins on the assembly process of microtubules has been limited to low-resolution light microscopy studies and static electron microscopy imaging. As a consequence, we still miss an understanding of the molecular events underlying these dynamic processes. The advent of single molecule techniques based on optical tweezers allowed us to design a new experimental method with which we can follow the microtubule assembly dynamics with near molecular resolution. Optical tweezers [126, 127] have been proven a powerful technique to detect piconewton forces and nanometer features describing the mechanics and movement of biological molecules: stepping of motors [128–135], interaction of proteins with DNA and RNA [136–138], folding/unfolding of proteins [139–141] being few examples. In an optical tweezers set-up a trapped micrometer-sized bead is used as a sensor. Traditionally, the protein of interest is attached to the bead and details in the motion of the bead reflects the action of the protein. The bead position can be detected with nanometer resolution using light microscopy or optical interferometry of the trapping beam. In this way molecular resolution can be achieved without directly imaging the protein of interest.

Based on these known facts, we developed a method integrating optical tweezers, micro-fabricated rigid barriers and high-resolution video tracking of micro-beads

[142, 143] (figure 2.1). The rigid barriers were used to obstruct microtubule growth. By detecting the position of a bead attached to a microtubule nucleating object instead of imaging the end of the growing microtubule, we could follow microtubule polymerization with near molecular resolution ( $\sim 10$  nm as compared with the  $\sim 200$  nm, the resolution of light microscopy). In our experiments the bead was held by optical tweezers allowing us to also measure the force experienced by the growing microtubule.

## 2.1 Experimental method

The optical tweezers set-up is schematically shown in figure 2.1 a. Microtubules were nucleated by a naturally occurring microtubule bundle, an axoneme, to which a polystyrene bead was attached near one end. The bead-axoneme construct was suspended in a 'keyhole' optical trap and positioned nearby a microfabricated rigid barrier. The keyhole trap was used to control both the position of the bead and the direction of the axoneme. After positioning the construct in front of the barrier, the microtubule growth from the axoneme was triggered by flowing a polymerization mix into the sample. When a growing microtubule encountered the barrier, subsequent length increases lead to displacement of the bead in the trap. In (statistically) half of the cases, the minus end of the axoneme was pointing towards the barrier. In these cases slow or no microtubule growth was observed. In the other cases, after some time, the bead started to move away from the barrier at a speed that was comparable to the microtubule growth speed. Displacement of the bead in the optical trap lead to an increasing restoring force on the bead that pushed the growing microtubule tip against the barrier. In all experiments the microtubules were kept short ( $< 1 \mu\text{m}$ ) to avoid buckling under the compressive load exerted by the optical trap (discussed below in section 2.3.1). The relation between the microtubule length increase and the bead displacement depends on the stiffness of the bead-axoneme construct, which we measure independently (described in section 2.3.2).

**The rigid barriers.** Photoresist barriers were made using standard microlithography techniques [144] (figure 2.1 b). A layer of SU-8 photoresist (MicroChem),  $7 \mu\text{m}$  in height, was deposited on pre-cleaned glass coverslips and soft-baked. The SU-8 layer was exposed to UV light through a chromium mask containing the chamber pattern and post-exposure baked. The illuminated areas were removed with developer (XP SU8-developer, MicroChem) leaving on the coverslip an array of chambers with slightly negative side walls. The SU-8 layer with chambers was hard-baked to further cross-link and increase the rigidity of the photoresist. One corner of a chamber was typically used as the rigid barrier against which microtubules were grown (figure 2.1 b, right).

**The axonemes.** Microtubules were nucleated from axonemes, naturally occurring microtubule bundles (figure 2.1 c). The axonemes were kindly prepared by Matthew Footer from sea urchin sperm following published protocols [145, 146] and stored frozen with a method modified from [147]. Purified axonemes have a  $9 + 2$  microtubule con-

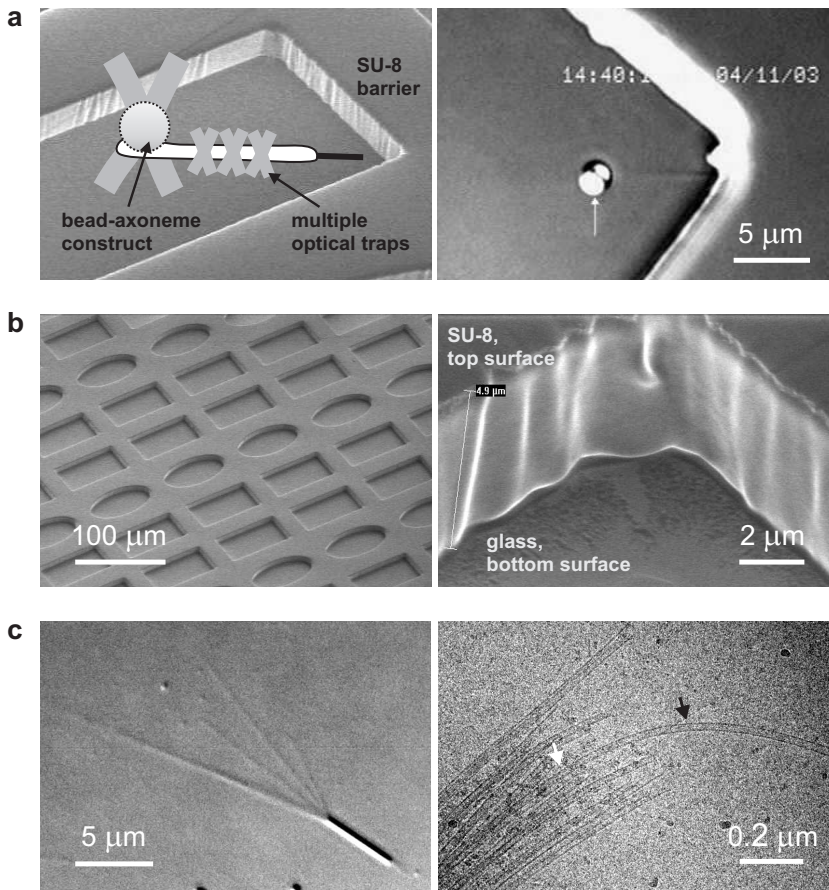


**Figure 2.1: Experimental set-up.** (a) Schematic drawing (left, not to scale) and DIC image (right) of a bead-axoneme construct held by optical tweezers near a rigid barrier. The arrow in the DIC image indicates the position of the optical trap on the bead. (b) Scanning electron micrographs of an overview on microfabricated chambers (left), and a detail view on the corner of a chamber showing the rather smooth vertical wall (right). The chambers were fabricated using standard micro-lithography techniques in a layer of SU-8 photoresist (5 - 7 μm high) deposited on a glass coverslip. The corner of such a chamber was typically used as the rigid barrier against which microtubules were grown. (c) DIC image (left) and cryo-EM picture (right) of microtubules nucleated from an axoneme piece. The high-resolution micrograph of the axoneme-end frozen in polymerization conditions (right) reveals that the doublets comprised in the axoneme nucleate normal microtubules. The black arrow points to one microtubule that was nucleated from a doublet (white arrow).

figuration consisting of nine microtubule doublets that surround two singlet microtubules [148]. The outer membranes and most of the microtubule associated motors and proteins were removed during the purification process. Cryo-EM imaging<sup>1</sup> showed that the axoneme doublets nucleate normal singlet microtubules when exposed to microtubule polymerization conditions (figure 2.1 c, right). As a result, an axoneme could nucleate up to 11 parallel microtubules depending on the tubulin concentration and the temperature in the sample. We tuned these parameters such that most of the time only one or two microtubules were growing from the plus end of the axoneme.

**Sample preparation.** A coverslip carrying SU-8 barriers was assembled into a home-built flow chamber. The chamber allowed injection of small samples (a couple of microliters by pipetting at an entrance opening) and continuous slow flow by adjusting the height of the drain. The drain and the chamber were connected by teflon tubing and a computer-linked flow sensor (Seyonic, Switzerland) was inserted between the drain and the chamber in order to monitor the flow magnitude. Prior to any sample injection, the flow chamber was passivated by applying a layer of 0.2% agarose and by incubation with 50 mg/ml BSA. The surface coating prevented undesired sticking of beads and axonemes on the glass and SU-8 surfaces. Streptavidin coated polystyrene beads (2  $\mu\text{m}$  in diameter, Spherotech) were flowed in the chamber together with axoneme pieces. Using the optical trap a construct was assembled by non-specific attachment of a bead to one end of an axoneme and then positioned in front of a barrier. Before introducing the polymerization mix, the chamber was incubated for 5 min with 1 mg/ml  $\kappa$ -casein to avoid non-specific attachment of axoneme and microtubule tips when in contact with the SU-8 walls. After passivation of the chamber surfaces, microtubule growth was initiated and maintained by flowing the polymerization mix that typically contained tubulin, GTP, with or without microtubule associated proteins, in assay buffer (MRB80: 80 mM K-Pipes, 1 mM EGTA, 4 mM  $\text{MgCl}_2$ , pH 6.8). The polymerizing conditions are mentioned in the following chapters for each experiment. The measurements were done at constant temperature, 25°C.

**Data acquisition.** DIC images of our experiments were recorded at a sampling rate of 25 Hz on DVD using a CCD camera (Kappa) and a commercial DVD recorder (Philips DVD-R80). The displacement of the bead in the trap was measured off-line from the digital images using a standard auto-correlation method (in-house developed image processing software written and run in IDL). Displacements were either multiplied with the trap stiffness to determine the force (section 2.2.3) or corrected for the construct stiffness to determine the microtubule length changes (section 2.3.2).

---

<sup>1</sup>The cryo-EM imaging of axonemes was done together with Linda Sandblad at EMBL, Heidelberg.

## 2.2 'Keyhole' optical trap

### 2.2.1 Optical tweezers set-up

An Nd:YVO<sub>4</sub> laser beam ( $\lambda = 1064$  nm, 10 W, Millennia<sup>tm</sup> IR, Spectra Physics) was coupled into an inverted microscope (DMIRB, Leica) equipped with a 100x/1.4 NA oil immersion lens (PL APO, Leica). The infrared laser beam was used for trapping the bead-axoneme construct. To create the 'keyhole' trap, consisting of multiple traps, the laser beam was time-shared with a pair of orthogonal acousto-optic deflectors (AODs) (DTD-274HA6, Intra Action). The trap position can be accurately controlled with microsecond resolution by changing the sound wave propagating within each AOD crystal. The sound waves were generated by a synthesizer board (DVE-40, Intra Action and later changed with two Direct Digital Synthesizers, DDS8m 100MHz, Novatech Instruments) and amplified before reaching the AODs with a dual RF power amplifier (DPA502, Intra Action). The synthesizer boards were controlled using in-house developed software (LabVIEW, National Instruments). For the calibration of the trap stiffness we used a low-power HeNe laser beam ( $\lambda = 633$  nm, 1125P, Uniphase) that was superimposed after the AODs on the infrared path. The HeNe laser beam was focused on a trapped bead and imaged onto a quadrant-photodiode (QD50-O-SD, Centro Vision) positioned in a plane conjugated with the back focal plane of the microscope condenser. The sample was mounted on a high-resolution *xy*-piezo stage (P-730.4c, Physik Instrumente), providing the ability to move the sample with nanometer precision both manually and automatically (an in-house developed LabVIEW program controls the automation).

### 2.2.2 'Keyhole' trap design and features

The 'keyhole' trap consists of a normal point-trap that holds the bead, which was used as a force sensor and a row of tightly-spaced optical traps of lower power, which together form a line trap [142, 143] (figure 2.2 b). This line trap is used to orient the axoneme in the direction of the barrier, thereby forcing the growing microtubule to encounter the barrier. With the axoneme in the line trap, the bead can resist forces up to tens of piconewton without sideways motion. Figure 2.1 a, right and figure 2.2 a, show DIC microscopy images where such a trap was holding a bead attached to an axoneme close to a wall. The keyhole trap was set up as follows: a single laser trap was quickly moved from one position to another using the acousto-optic deflectors (open markers in figure 2.2 b). The leftmost position is visited most often and is separated from the others to serve as the point trap for the bead. The others are spaced much closer together along a line. In the example shown in figure 2.2, the whole cycle was run at a finite frequency: 2190 Hz over a total distance of about 6  $\mu$ m. In other experiments the cycle frequency was up to 12.5 kHz. This is much faster than a trapped bead or an axoneme can follow given the viscosity of the medium and the stiffness of the trap (which together determine the response time). When a construct suspended in this trap was

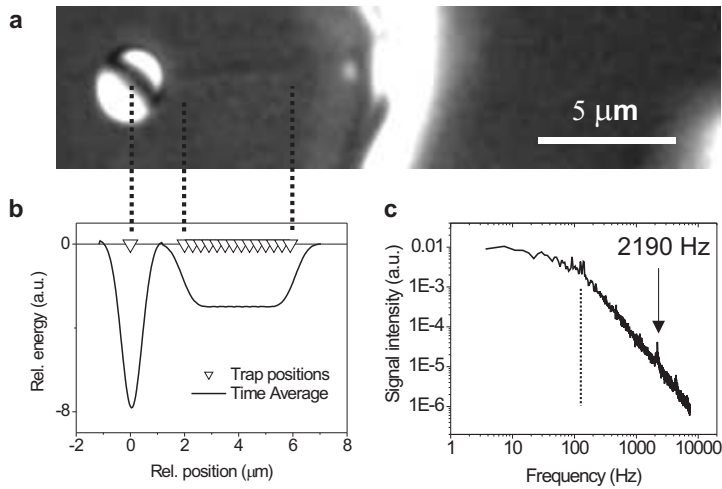


**Figure 2.2: 'Keyhole' trap.** (a) DIC microscopy image of a trapped bead-axoneme construct near a microfabricated wall. The small round object near the barrier is a piece of debris stuck to the axoneme. (b) Time-shared laser positions (open triangles) and potential well (solid line) of the time-averaged keyhole trap. (c) Power spectrum of a bead trapped in the keyhole trap, with the writing frequency of the trap indicated. The dotted line indicates the roll-off frequency, which is used to calculate the trap stiffness.

pushed to the left, only the bead experienced a restoring force from the trap since the axoneme was free to move along its length in the line trap. As shown in figure 2.2 a and b, the outer points of the line trap were kept far from the ends of the axoneme, to minimize a potential influence of the axoneme ends on the force-displacement behavior of the whole construct. Keeping the laser away from the barrier also prevented interference with the vertical edges. The potential well of the keyhole trap was determined as follows. First, loose beads were repeatedly trapped and released in a highly viscous medium and their velocity was measured as a function of distance from the trap center. At every position, the viscous drag force on the bead  $F = \gamma v$  is equal to the trap force. Integrating the force-distance profile gives us a measure of the effective trap potential of a single isolated trap. The total well shape of the keyhole trap (solid line in figure 2.2 b) was obtained by simply time-averaging the trap potential for all the individual trap positions. Note that the interaction of the trapping laser with the axoneme will be less and the axoneme will therefore experience a shallower potential well.

### 2.2.3 Determining the trap stiffness

To determine the trap stiffness and confirm that the writing frequency of the trap is much faster than the response time of the bead, we measured the power spectrum of the motion of a loose bead trapped in the leftmost point of the keyhole trap using a



low power HeNe laser and a quadrant photo diode (QPD) as detector ( $f_{\text{sampling}} = 30$  kHz) (figure 2.2 c). This spectrum gives the trap stiffness  $k_{\text{trap}} = 2\pi\gamma f_c$ , where  $\gamma = 6\pi\eta a$  is the viscous drag (for viscosity  $\eta$ ) on the bead (with radius  $a$ ) and  $f_c$  is the roll-off frequency (indicated by the dotted line). The trap stiffness was typically between 0.01 and 0.03 pN/nm. In addition, the power spectrum shows some sharp peaks, of which the lowest in frequency (arrow) indicates the writing frequency of the keyhole trap. In the experiments with higher cycle frequency ( $> 10$  kHz), these peaks did not appear in the spectrum as the QPD signals were filtered through an anti-aliasing filter ( $f_{\text{filter}} = 10$  kHz). At the cycle frequency the bead will experience very small regular excursions due to the fact that the trap is periodically moved to another position. We note that the magnitude of these excursions is proportional to the surface below the peak, whereas the total Brownian motion is proportional to the surface below the whole spectrum. This implies that in a displacement vs time plot such as in a microtubule growth experiment, these excursions are entirely negligible and the keyhole trap can be considered smooth and continuous as in figure 2.2 b.

## 2.3 Experimental considerations

### 2.3.1 Mechanics of microtubules under load

When trying to measure microtubule growth under load, an experimental difficulty that needs to be overcome is the finite rigidity of the polymer. In our experimental set-up, when a growing microtubule is pushing against the rigid wall, a compressive force is generated that may cause the microtubule to bend or buckle. If a microtubule buckles or bends under the compressive force, the increase in length cannot be detected anymore by the response of the bead. Elasticity theory tells us that a filament of finite length  $L$  and stiffness  $\kappa$  will only remain straight as long as the force stays below a critical buckling force given by  $F_c = A\kappa/L^2$  [149], where the prefactor  $A$  depends on how the filament is attached at its extremities. For a filament that is clamped at one end and free to fluctuate at its other end this prefactor is approximately 20. This means that for microtubules (assuming a stiffness  $\kappa = 25$  pN $\mu\text{m}^2$ ) subjected to a compressive load of a few piconewton, the maximum filament length that remains straight is a few micrometers. Recent results showed that microtubule stiffness is length dependent. For microtubules shorter than 2-3  $\mu\text{m}$ , stiffness can be a factor 500 lower than for 10  $\mu\text{m}$  long microtubules [43]. This effect could be explained by the internal friction between protofilaments that contributes to the fluctuation dynamics [45]. In our experiments, we measured forces below 5 pN and the microtubules were mostly shorter than 600 nm. Due to the complicated geometry in our set-up it is not easy to theoretically predict the conditions at which the microtubules will buckle. In a test experiment we noticed that when a growing microtubule was in contact with the barrier the Brownian noise on the bead was low ( $\sim 5$  nm RMS) as compared to the noise on the bead when the microtubule starts buckling and the situation when there is no contact between the

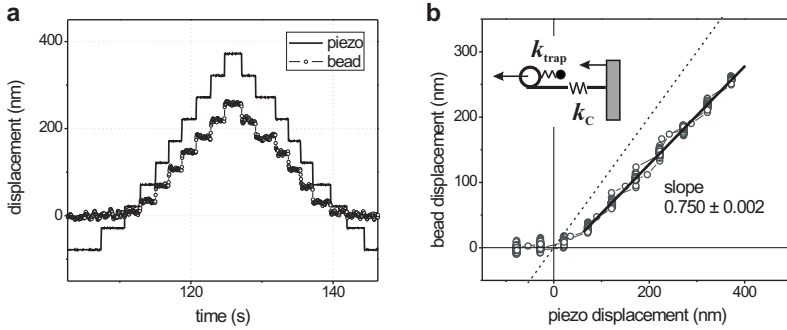


**Figure 2.3: Measuring the construct stiffness.** (a) Response of the trapped bead (open circles) when the rigid barrier is bounced (thick line) against the axoneme. The wall was moved in a controlled way by an automated piezo stage. (b) Bead displacement from the same experiment plotted as a function of the wall displacement. In the linear regime, the slope depends on the of trap stiffness,  $k_{\text{trap}}$ , and the construct stiffness,  $k_c$  (see text). Dotted line indicates a slope of 1.

microtubule and the barrier ( $\sim 10$  nm RMS). Buckling was also accompanied by a drop in force. We therefore only used data that displayed low Brownian noise ( $\sim 5$  nm RMS) during microtubule length changes.

### 2.3.2 Finite stiffness of the bead-axoneme construct

When a microtubule grew or the wall was pushed against the axoneme, the bead moved from the trap center over a distance that was generally smaller than the motion of the axoneme tip (figure 2.3 a). A one-to-one relation is only expected when the bead-axoneme construct is infinitely stiff, which in practice is not the case. The stiffness of the bead-axoneme construct,  $k_c$ , includes the effect of the non-rigid bead-axoneme connection together with the finite stiffness of the axoneme. We measured  $k_c$  by repeatedly pushing the wall against the construct and plotting the subsequent bead displacement,  $\Delta_{\text{bead}}$ , as a function of the wall displacement,  $\Delta_{\text{wall}}$  (figure 2.3 b). In the linear regime, the slope of this plot is given by:

$$\frac{\Delta_{\text{bead}}}{\Delta_{\text{wall}}} = \frac{k_c}{k_c + k_{\text{trap}}} \quad (2.1)$$

Microtubule length changes can therefore be inferred from the bead displacement corrected for the construct stiffness. Before each experiment we performed a similar calibration as shown in figure 2.3 to determine  $\Delta_{\text{bead}}/\Delta_{\text{wall}}$ . We only analyzed bead displacements above the initial non-linear regime due to the softness of the construct at contact (see figure 2.3 b). The main cause of this initial softness is most probable the spatial arrangement of the contact point between the bead and the axoneme. As long as the microtubule remains straight and no buckling occurs, the stiffness of the construct should remain constant and any length increase of the growing microtubule should lead to a proportional displacement of the bead in the trap.

## 2.4 Dynamic instability of microtubules measured with optical tweezers

### 2.4.1 High-resolution details of microtubule dynamics

With our technique we can follow bead displacement and therefore microtubule growth with nanometer resolution, giving unprecedented high-resolution and the possibility to gain insight into the molecular details of how microtubules grow and shrink. Figure 2.4 shows dynamic instability of microtubules measured with our optical tweezers based technique. In these experiments growth (g), stalling (st), catastrophes (c), and subsequent shrinkage (s) of microtubules are readily observed. Microtubule length changes were determined from the bead displacement corrected for the construct stiffness and the force was determined as  $\Delta_{\text{bead}} \times k_{\text{trap}}$ . Growth often stalls at a few piconewton of force before a catastrophe occurs, which is consistent with previous measurements of microtubule stall force [70, 76, 77]. The upper panel shows a couple of growth and shrinking events of individual microtubules. When zooming in on the growth and shrinking phases in our trap data (insets in figure 2.4, top panel), details can be observed that were previously not possible to detect due to the limited resolution of conventional light microscopy, typically used to image microtubules. For example, we observed that microtubule growth does not always occur through a smooth process, but sometimes fast length excursions are observed (figure 2.4, top panel, inset). We could also identify molecular details associated with catastrophes, the transitions from growth to shrinkage. One can see a length reduction of  $\sim 20$  nm before the fast shrinkage in the event plotted in the inset of figure 2.4, top panel. This length decrease might correspond to the depolymerization of the microtubule end-structure, the loss of which triggers microtubule disassembly.

### 2.4.2 Dynamics and force generation of multiple microtubules

One axoneme can nucleate up to 11 microtubules. The average number of microtubules nucleated from the axoneme end can be tuned by adjusting the tubulin concentration and the temperature. In the experiments included in this thesis, we chose the conditions in such a way that only one microtubule was growing on average from the axoneme (inset in figure 2.4, lower panel). At these conditions, multiple microtubules can sometimes simultaneously grow from the axoneme. Lower panel in figure 2.4 shows such an example. The signature of multiple microtubules is occurrence of incomplete shrinkage events (black arrows) followed by immediate resumption of growth that appear as rescues (indicated by open triangles). In our experimental conditions the rescue rate for individual microtubules is extremely low and we do not expect to observe switching events from shortening to elongation. The apparent rescues can be explained as follows. When one microtubule was shrinking, the bead-axoneme construct moved towards the barrier until another growing microtubule was in contact

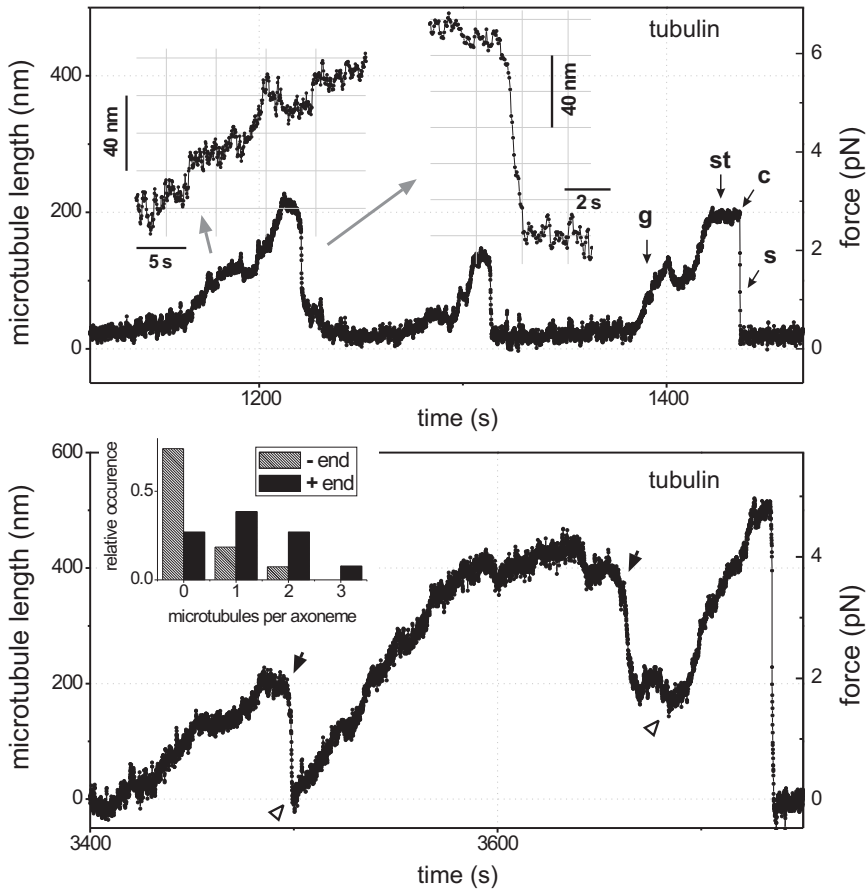


**Figure 2.4: Dynamic instability of microtubules measured with optical tweezers.** Dynamic microtubules were nucleated by an axoneme in the presence of  $15 \mu\text{M}$  tubulin at  $25^\circ\text{C}$ . In these polymerizing conditions, mostly one microtubule was nucleated by the axoneme (upper panel), but sometimes 2-3 microtubules were growing simultaneously from the axoneme end (lower panel). The inset in the lower panel shows the distribution of the number of microtubules growing from the plus and minus ends of  $n = 27$  axonemes. Growth (g), stalling (st), catastrophes (c), and shrinkage (s) of microtubules can be easily identified. Both the microtubule length and the opposing force on the microtubules are indicated. The insets in the upper panel show at higher magnification one growth and one shrinkage event. In the lower panel the presence of multiple microtubules is identified by the incomplete shrinkage events (black arrows) during which an apparent rescue occurred (open triangles). These apparent rescues are due to the growing microtubules that reach the rigid barrier while another microtubule was depolymerizing.

with the barrier. From that moment on the bead moved again away from the barrier following the growth of the second microtubule. During growth we sometimes observed plateaus indicating stalling of the microtubule, followed by short length decrease and resumption of growth. In these cases, it is not clear if we detected growth of multiple microtubules or a single one that posed and resumed growth. Variability during single microtubule growth, without a catastrophic event leading to depolymerization, was also observed in experiments using a similar high-resolution technique [150]. We also noticed that a bundle of microtubules could generate higher forces than we typically observed for single microtubules. This implies that microtubules are able to divide a resisting force between them, allowing them to collectively push more strongly than alone (discussed in [151, 152]).

The optical tweezers based technique enabled us to follow dynamic microtubule ends with unprecedented resolution. We used this technique to gain new information on the sequence of molecular details underlying microtubule dynamic instability and understand how, on a molecular scale, microtubule associated proteins regulate microtubule dynamics.

### ***Acknowledgements***

I would like to thank Jacob Kerssemakers for developing the optical tweezers based method employed to follow dynamic microtubules. I acknowledge Duncan Verheijde for development of the electronics design and Johan Herscheid for software development.



---

## Influence of XMAP215 on microtubule dynamics

*XMAP215 is a microtubule-associated protein that is known to dramatically enhance the microtubule growth velocity. The molecular mechanism by which this effect is achieved is not yet understood. We used optical tweezers to observe the assembly dynamics of individual microtubules at molecular resolution. We find that microtubules can near-instantaneously increase their overall length by amounts exceeding the size of individual dimers (8 nanometer). When the microtubule-associated protein XMAP215 is added, this effect is dramatically enhanced and fast length increases around 60 nanometer are observed (which corresponds to the length of the XMAP215 protein itself). The enhanced addition of tubulin at the growing end of the microtubule in the presence of XMAP215 can have several interpretations: The XMAP215 protein might act as a template to assemble long tubulin oligomers, either in solution or at the microtubule tip. In order to further shed light on the molecular mechanism of interaction between tubulin and XMAP215 we used fluorescence speckle microscopy and fluorescence correlation spectroscopy. In these experiments we attempted to measure XMAP215-tubulin complex formation. We did not detect big size complexes that would correspond to the full length of XMAP215 protein covered with tubulin dimers. Therefore, the fast length increases observed during microtubule growth at high resolution, might be due to a local acceleration of tubulin dimer addition when XMAP215 is present at the microtubule end. Further experiments are necessary to elucidate the molecular mechanism of interaction between XMAP215 and tubulin.*

Microtubules are highly dynamic protein polymers [6] that form a crucial part of the cytoskeleton in all eukaryotic cells. The core structure of a microtubule consists of typically 13 or 14 protofilaments forming a hollow tube (Figure 3.1 a). Microtubule assembly is accompanied by the hydrolysis of tubulin-bound GTP, which occasionally triggers the microtubule to undergo a catastrophe and switch to a state of rapid disassembly [6]. Information about the structure of growing and shrinking microtubule ends as well as the (preferred) conformational state of GTP-bound and GDP-bound tubulin in these situations comes from static electron microscopy studies [34, 50, 51], which indicate that growing microtubule ends consist of sheets of slightly outward-curved protofila-

ments and that shrinking microtubule ends consist of individual protofilaments that curve outwards more strongly. Information on the assembly dynamics of microtubules has been limited, both *in vitro* [56, 57] and *in vivo* [54, 55] to measurements of average growth and shrinkage rates over several thousands of tubulin subunits.

To obtain dynamic information on the growth and shrinkage of microtubules at the resolution of single tubulin dimers (8 nm) we used a technique based on optical tweezers (chapter 2). We show results for microtubule assembly from pure tubulin, and then show how, on a molecular scale, the growth process is altered by the presence of XMAP215, an evolutionary conserved protein [120] that enhances the growth rate of microtubules [121, 122, 153].

### **3.1 Microtubule assembly in the presence of XMAP215**

#### **3.1.1 XMAP215 enhances microtubule growth and catastrophes**

To test the effect of XMAP215 on the dynamics of freely growing microtubules, we followed the growth and shrinkage of microtubules nucleated from axonemes and seeds (short stable microtubules) using DIC microscopy (see section 3.3.1).

The changes in the dynamic instability parameters in the presence of XMAP215 are summarized in table 3.1. As expected from previous observations [121, 122], XMAP215 had a potent effect on the microtubule growth velocity. The growth speed enhancement was stronger with increasing XMAP215 concentration. Microtubules grew 4 times faster when XMAP215 was present in solution at a ratio of 1 : 20 XMAP215 : tubulin. XMAP215 had also a destabilizing effect on microtubules by stimulating catastrophes and increasing the shrinkage speed. This effect can not be explained only by the presence in the sample of extra salts from the protein buffer, which also induced destabilization of microtubules. In the presence of XMAP215 the increase in the catastrophe rate was stronger. We also observed that XMAP215 induces depolymerization of the GMPCPP stabilized microtubules, used as nucleation sites in these experiments. The depolymerization of GMPCPP microtubules by XMAP215 was also reported earlier [68]. XMAP215 was proposed to destabilize the microtubule 'blunt' ends (that are believed to represent a paused microtubule state), which would increase the chance of transition to the shrinkage phase.

It is still not known how XMAP215 can exert a dual effect on microtubule dynamics. It is possible that the protein can enhance both the on- and off-rate of GTP-tubulin assembly at the growing microtubule tip. Depending on the conditions, either microtubule growth or catastrophes would be favored. To find more information on the mechanism by which XMAP215 influences the microtubule growth dynamics, we followed microtubule assembly process at molecular resolution.



tub [ $\mu\text{M}$ ]	XMAP215 [nM]	buffer (+/-)	$v_{\text{gro}}$ ( $\mu\text{m}/\text{min}$ ) mean $\pm$ sem (n)	$v_{\text{shr}}$ ( $\mu\text{m}/\text{min}$ ) mean $\pm$ sem (n)	$f_{\text{cat}}$ ( $\text{min}^{-1}$ ) mean $\pm$ sd ( $N_{\text{cat}}$ )
10	0	-	$0.58 \pm 0.02$ (24)	$19 \pm 2$ (18)	$0.19 \pm 0.04$ (21)
15	0	-	$0.91 \pm 0.19$ (64)	$18 \pm 1$ (23)	$0.16 \pm 0.02$ (63)
20	0	-	$1.08 \pm 0.04$ (27)	$22 \pm 1$ (21)	$0.13 \pm 0.03$ (23)
25	0	-	$1.24 \pm 0.05$ (15)	$10 \pm 1$ (9)	$0.07 \pm 0.02$ (13)
15	0	+	$0.91 \pm 0.03$ (44)	$29 \pm 1$ (44)	$0.35 \pm 0.05$ (47)
15	150	+	$1.40 \pm 0.12$ (8)	$46 \pm 3$ (6)	$0.60 \pm 0.21$ (8)
15	255	+	$1.49 \pm 0.07$ (21)	$38 \pm 4$ (16)	$0.71 \pm 0.15$ (24)
15	675	+	$3.78 \pm 0.39$ (16)	$25 \pm 3$ (13)	$1.40 \pm 0.35$ (16)
				$t_{\text{cat}} = \langle L \rangle / v_{\text{gro}}$ (sec)	MT end
20	0	+	$1.70 \pm 0.14$ (8)	-	plus
20	150	+	$2.30 \pm 0.30$ (11)	140	plus
20	0	+	$0.30 \pm 0.05$ (5)	-	minus
20	150	+	$1.00 \pm 0.15$ (4)	500	minus

**Table 3.1:** Dynamic instability parameters of microtubules growing freely from seeds (upper half) or axonemes (lower half) were measured. Growth velocities,  $v_{\text{gro}}$ , were measured as linear fits to individual growth events (total n). Shrinkage velocities were measured in a similar way from the moment a catastrophe occurred until the microtubule disappeared (no rescues were observed). Errors represent s.e.m. The catastrophe frequency,  $f_{\text{cat}}$ , was calculated by dividing the total number of catastrophes observed,  $N_{\text{cat}}$ , by the total growth time. The errors were evaluated as  $f_{\text{cat}}/\sqrt{N_{\text{cat}}}$ . For the microtubules nucleated by axonemes an estimate for the average catastrophe time,  $t_{\text{cat}}$ , is given as the average microtubule length over the entire observation time,  $\langle L \rangle$ , divided by the growth velocity,  $v_{\text{gro}}$ . Minus ends had very few catastrophes, even in the presence of XMAP215.

### 3.1.2 Assembly dynamics at molecular resolution

To follow dynamic microtubules with high-resolution, we used a method based on optical tweezers (chapter 2). The experimental set-up is shown schematically in figure 3.1 b. Shortly, we allowed dynamic microtubule plus ends to grow and shrink against a micro-fabricated barrier and we monitored the response of a microbead attached at the other end of the microtubule nucleation site, an axoneme. The bead-axoneme construct was held by a 'keyhole' optical trap.

Figure 3.1 c shows the restoring force exerted by the trap during a sequence of microtubule growth and shrinkage events. The upper panel shows regular microtubule growth, with an initial tubulin concentration of  $20 \mu\text{M}$ . The protein concentration slowly decreases as indicated by the smooth curves (as the result of a slow buffer flow). Growth often comes to an apparent halt at a few piconewtons of force before catastrophes occur, which is consistent with what is known for the effect of force on the assembly dynamics of microtubule plus ends [70, 76, 77]. The frequent occurrence of catastrophes confirms that the observed growth is that of a plus end of a microtubule. The

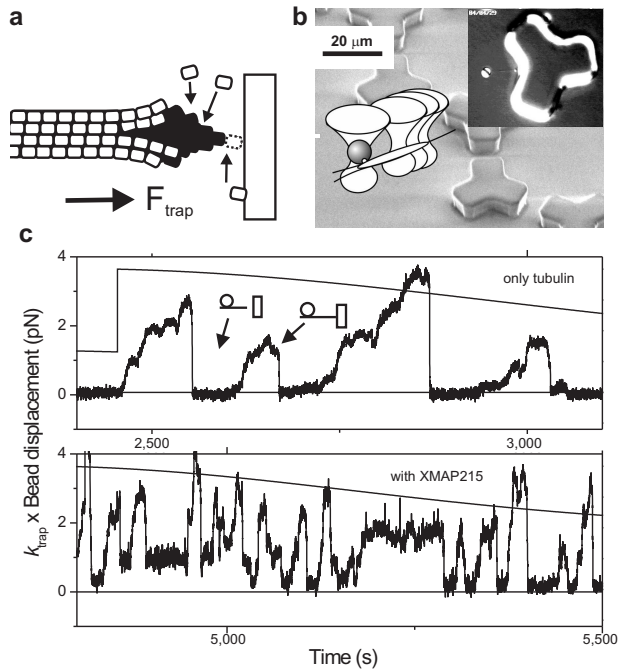


**Figure 3.1: Measuring growth dynamics of microtubules with optical tweezers.** (a) Schematic view of a growing microtubule. (b) Schematic and DIC image of a 'keyhole' optical trap holding a bead-axoneme construct in front of a microfabricated barrier. (c) Growth and shrinkage events of individual microtubules in the absence (upper panel) and presence (lower panel) of XMAP215. The smooth curves give estimates of the gradually decreasing protein concentration (maximum tubulin concentration 20  $\mu\text{M}$ ).

lower panel shows growth from the same construct after replacement of the surrounding solution with 20  $\mu\text{M}$  tubulin and 150 nM XMAP215. With XMAP215 present, growth is faster and catastrophes occur more frequently, in agreement with previous reports [68, 121, 122, 153] and our own observations in the absence of force (section 3.1.1).

Figure 3.2 shows part of the same data at higher resolution, this time with the microtubule length, corrected for the stiffness of the bead-axoneme construct, on the y axis. These data gives us unprecedented resolution on the growth dynamics of individual microtubules, limited only by the thermal noise on the bead in the trap and the stiffness of the bead-axoneme construct (about 5-10 nm root-mean-square in practice). In these data we occasionally observe step-like length increases that are clearly distinguishable from the experimental noise, even by eye (figure 3.2 a, arrows). When we add XMAP215 (figure 3.2 b), fast increases occur more frequently and are also larger, on the order of several tens of nanometers, occurring on a timescale of about 100 ms or less (the average microtubule growth rate under these conditions corresponds to at most

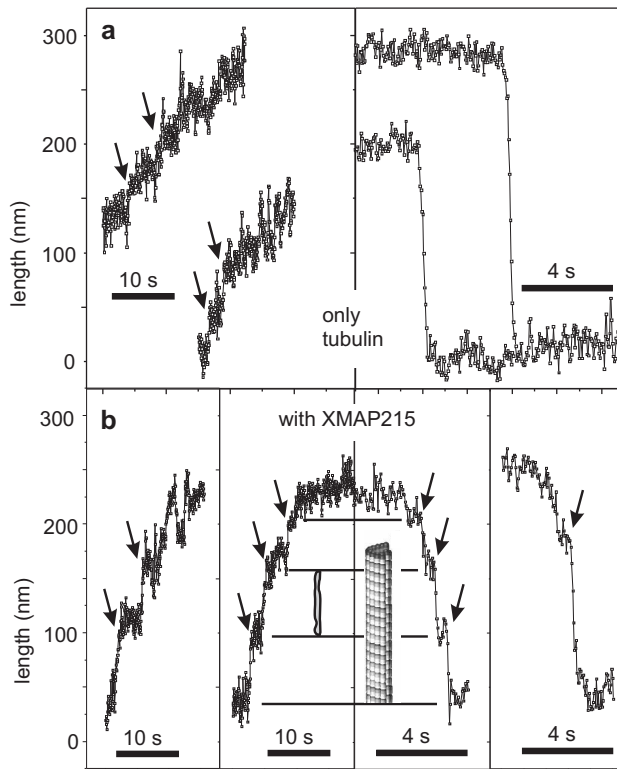


**Figure 3.2: High-resolution details of growth and shrinkage events.** Length traces are shown for events without (a) and with (b) XMAP215. Arrows indicate fast length changes (steps) that are distinguishable from the noise by eye. During subsequent growth and shrinkage events in the presence of XMAP215, steps sometimes appear in register with each other ((b), middle, lines). The insets show schematic drawings of an XMAP215 molecule (left) and a microtubule (right) at the same scale as the length data.

1 or 2 nm per 100 ms). In the presence of XMAP215, steps are also clearly observed during shrinkage events (figure 3.2 b, right). These steps are of similar sizes to those observed during growth, sometimes even in marked registry with previous growth steps (figure 3.2 b, middle). The sizes of the large steps often seem close to the known length of the XMAP215 protein itself [64], as indicated in figure 3.2 b. In addition to steps we observe periods with more gradual increases in length, in which steps are not clearly distinguishable. Given our experimental resolution this is to be expected: microtubule ends are likely to have multiple binding sites for tubulin dimers at unequal positions along the microtubule axis (see figure 3.1 a), and growth due to single dimer additions, for example, should lead to mostly small steps with a maximum of 8 nm.

To be able to analyze in an unbiased way the steps observed by eye, we developed

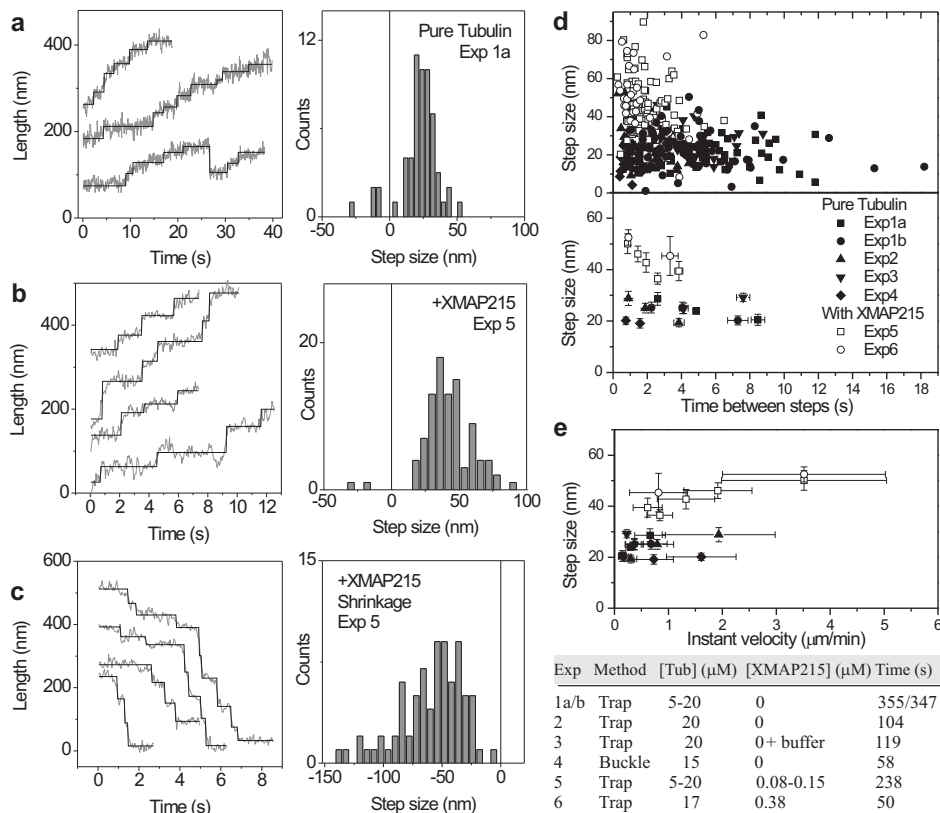


**Figure 3.3: Quantifying the sizes of the large steps with our step-fitting algorithm.** Step fits and associated step histograms are shown for regular microtubule growth (a), growth with XMAP215 present (b) and shrinkage with XMAP215 present (c). (d) Step sizes for six different growth experiments with conditions and analyzed growth times as listed in the table (experiments 1a, 1b and 5 were performed with the same bead-axoneme construct; shrinkage was analyzed only for experiment 5 (63 s); experiment 4 involves data obtained previously with a different 'buckling' method [76]). Top: individual step sizes plotted against the time between steps. Bottom: the same data averaged over 20 steps (the last data point may contain fewer steps). (e) Averaged step sizes as in (d) but plotted against 'instant velocity' (step size divided by time between steps). Error bars in (d) and (e) represent s.e.m.

a step-fitting algorithm as outlined in section 3.3.2. Because in our system many of the steps were smaller than the noise, we could use the algorithm only to find and quantify the largest steps (figure 3.3). In the histograms presented, any steps (or lack thereof) close to or below the noise level are therefore insignificant. For regular tubulin growth, the step fit result and the associated histogram (figure 3.3 a) confirm the presence of steps up to 20 - 30 nm in size. This is significantly larger than the tubulin dimer size of 8 nm. In the presence of XMAP215, the histograms for growth (figure 3.3 b) and shrink-

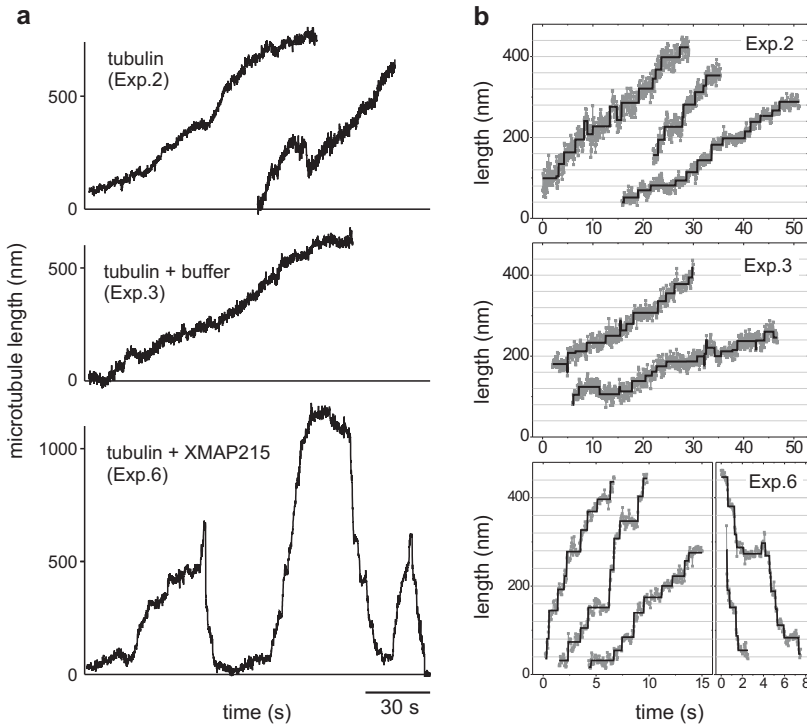


**Figure 3.4: Microtubule growth and shrinkage events.** (a) Length traces of microtubules assembled in the absence (upper panel, experiment 2), in the presence of protein buffer (middle panel, experiment 3), and in the presence of XMAP215 (lower panel, experiment 6) were monitored. The protein concentrations used in these experiments are listed in table in figure 3.3 e. In the experiments without XMAP215 we did not detect catastrophes as the growing microtubule(s) later adhered with the tip non-specifically to the photoresist wall that prevented them from depolymerization. (b) Part of the same data at higher resolution and the step fit result. The starting point of each segment (both length and time) is relative.

age (figure 3.3 c) show larger step-like changes, around 40 - 60 nm in size. The observed step sizes are independent of how quickly steps follow each other (i.e. the rate at which microtubules grow). Our experiments were performed at various tubulin concentrations and forces (both of which affect the average microtubule growth velocity [76]), as well as for two different XMAP215/tubulin ratios. When we plot individual (figure 3.3 d, top) and averaged (figure 3.3 d, bottom) step sizes as a function of the time between steps for six different experiments, we find that the step sizes are always larger in the presence of XMAP215, even when the resulting (instant) growth velocity is the same (plotted in figure 3.3 e). Figure 3.4 shows microtubule growth traces from the experiments used to evaluate step sizes, other than the data included in figure 3.3 a-c (see table in figure 3.3 e).

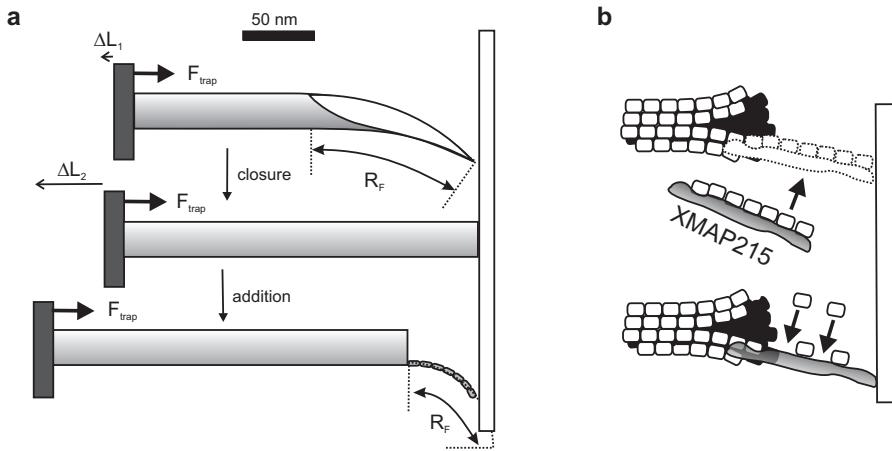


**Figure 3.5: Microtubule end mechanics.** (a) Schematic drawing of a microtubule end under a compressive force (roughly to scale). Top: a microtubule with a sheet-like extension of 125 nm (preferred radius of curvature  $R_0 \approx 250$  nm) adopts a force-induced radius of curvature  $R_F \approx 200$  nm under a compressive force of 2.5 pN (conservative estimate of the sheet stiffness  $1.2 \times 10^5$  pN nm<sup>2</sup>; that is, about 1/100 that of a microtubule). Middle: the same microtubule appears about 8 nm longer ( $\Delta L_1$ ) on full sheet closure. Bottom: the addition of a single, 60-nm-long protofilament (preferred radius of curvature 76 nm; stiffness  $2.4 \times 10^4$  pN nm<sup>2</sup>) under a similar compressive force will lead to an apparent length increase ( $\Delta L_2$ ) of about 50 nm ( $R_F \approx 60$  nm). (b) Possible mechanisms for XMAP215-enhanced addition of long oligomers.

### 3.2 Discussion

The observation of fast increases in length larger than the dimer size might have two interpretations: either we were observing extended closure events of outward-curved sheets existing at the ends of growing microtubules, or we were observing the addition of tubulin oligomers larger than individual tubulin dimers. To estimate the expected length increase in these two cases, we must consider the geometry and rigidity of tubulin oligomers and microtubule sheets as well as the distortions that one expects in the presence of a few piconewtons of force. In our experiments microtubules grew relatively slowly and never very long (typically a few hundred nanometers). In figure 3.5 a we show schematically a reasonable estimate, based on electron microscopy studies [34, 154], of a typical microtubule sheet under these conditions, drawn to scale. The estimates shown in figure 3.5 (see also section 3.3.1) indicate that length increases due to oligomer addition, as opposed to sheet closure events, should be readily detectable.

Our observations therefore indicate that microtubule assembly might not always occur simply by the addition of individual tubulin dimers. Small oligomers of up to three tubulin dimers seem to be able to attach to growing microtubules as well. This is consistent with observations that microtubule assembly is reduced when tubulin oli-

gomers are centrifuged away from microtubule polymerization solutions [51]. The step sizes of 40 - 60 nm in the presence of XMAP215 indicate that XMAP215 might facilitate the addition of even longer oligomers. Again, there are two ways in which this could be accomplished [63, 65]. First, XMAP215 could template the assembly of a tubulin oligomer in solution and this whole complex could subsequently attach to the end of the growing microtubule (figure 3.5 b, top). Because the overall growth velocity of microtubules is enhanced by the addition of even a small amount of XMAP215, this would have to mean that the XMAP215-tubulin complex has a higher affinity for the microtubule end than tubulin alone (possibly because of 'pre-straightening' of the tubulin oligomer by the XMAP215 molecule). To us, this seems a likely mechanism because it is known from electron microscopy studies that XMAP215 can bind free tubulin dimers in a protofilament-like fashion, resulting in XMAP215-tubulin complexes with lengths up to 60 nm [64]. In addition, there is indirect evidence that other microtubule-binding proteins such as CLIP170 bind tubulin dimers before attaching to growing microtubules as well [29, 66, 67].

The second possibility is that XMAP215 could first bind to the microtubule end and then accelerate the build-up of an oligomer along the length of the XMAP215 molecule (figure 3.5 b, bottom). In both cases it is possible that the XMAP215-tubulin complex first binds under an angle to the microtubule end and then straightens out the longitudinal bond in some kind of power stroke. In fact, the instant straight addition of an oligomer 40 - 60 nm long through a purely brownian ratchet mechanism would require an unusually large fluctuation of the microtubule end away from the barrier [76]. Finally, the step-like nature of shrinkage events indicates that XMAP215 might stay attached to the microtubule lattice for at least some time after arrival, where it hampers microtubule depolymerization. The shrinkage phases are further discussed in chapter 6.

The method described here for detecting the molecular details of microtubule assembly also paves the way for understanding the action of other classes of microtubule associated proteins [20, 22, 155]. Microtubule-associated proteins and end-binding proteins mediate the interaction of microtubules with cellular targets such as the kinetochore and the cell cortex. Understanding, at a molecular level, the operating principles of these proteins will be essential for understanding the regulation of microtubule dynamics in cells.

### 3.3 Methods

#### 3.3.1 Measuring microtubule dynamics

***DIC measurements on freely growing microtubules.*** Dynamic microtubules were nucleated from stabilized seeds or axonemes. The stabilized seeds were prepared by incubation of a tubulin mix containing biotin-labelled and non-labelled tubulin (Cytoskeleton) in a ration of 1:5 (total of 100  $\mu$ M tubulin) with 1 mM GMPCPP (Jena Bioscience) at

36°C for 30-60 minutes. The biotin-labelled seeds were specifically bound to a streptavidin functionalized surface in a flow chamber. The surface was realized by incubating the chamber with 2.5 mg/ml biotin-BSA in acetate buffer (21 mM acetic acid, 79 mM  $C_2H_3O_2Na$ , pH 5.2) and after rinsing, subsequent incubation with 1 mg/ml streptavidin in assay buffer (MRB80, pH 6.8). All chemicals were purchased from Sigma, otherwise mentioned. The axonemes, the same as used for the trap experiment, were directly bound to the pre-cleaned glass coverslip by non-specifically interactions and the surface was subsequently passivated by incubation with 10 mg/ml BSA. Microtubules were imaged by video-enhanced differential interference contrast (VE-DIC) microscopy for 60-90 min. Movies of the experiments were recorded on video tape and digitized off-line at a rate of 2 Hz. Microtubule length versus time traces were measured using an in-house developed software written and run in IDL. Growth and shrinkage speeds were evaluated from individual events by a linear fit. More details about the sample preparation and the data analysis are given for a similar experiment in section 5.5.1.

**Optical tweezers based technique** (see chapter 2 for details). We used an Nd:YVO4 1064-nm laser (Spectra Physics) to trap a construct: a bead connected to a rigid axoneme (figure 3.1 b). The laser was time-shared to create a 'keyhole' trap [142], consisting of a point trap holding the bead and a line trap directing the axoneme towards a microfabricated barrier. Photoresist (SU-8) barriers [144] were made using standard microlithography techniques. Axonemes from sea urchin sperm were prepared by M. Footer from published protocols [146] and were bound to streptavidin-coated beads (2  $\mu m$  diameter, Spherotech) by non-specific binding. Microtubule growth was initiated by flowing in a mixture of tubulin and GTP, with or without the addition of XMAP215. The conditions were chosen such that most of the time only one or two microtubules were nucleated by the plus end of the axoneme. When a microtubule reached the barrier, further length increases led to displacement of the bead in the trap. The relation between the increase in microtubule length and the displacement of the bead depends on the stiffness of the bead-axoneme construct, which we measured independently by pushing the barrier against the construct (figure 3.6 a) before growth was initiated. Displacement of the bead in the optical trap led to an increasing restoring force on the bead (given by the trap stiffness,  $k_{trap}$ , multiplied by the bead displacement) that pushes the growing microtubule tip against the barrier. We kept the growing microtubule short (less than 1  $\mu m$ ) to prevent the microtubule from buckling under this compressive load [70]. DIC images of our experiments were recorded on DVD with a charge-coupled device camera (Kappa) and a standard DVD recorder (Philips DVD-R80). The displacement of the bead in the trap was measured from the digital images at a sampling rate of 25 Hz with the use of a standard auto-correlation method (image processing software home-written in IDL).

A step-fitting algorithm was developed and written in MatLab (section 3.3.2). To test how well our set-up is able to distinguish stepped from linear growth and to verify that



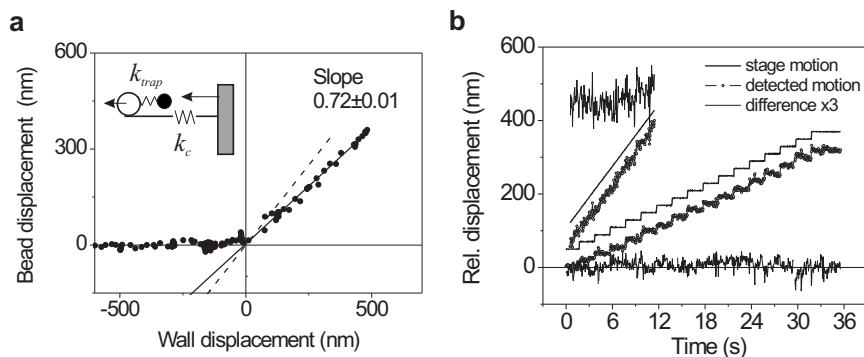


**Figure 3.6: Step detection test.** (a) Measurement of the construct compliance by a bouncing procedure: repeatedly pushing the wall against the construct and monitoring the bead response as a function of the wall displacement. In the linear regime, the slope of this plot is given by  $\Delta_{\text{bead}}/\Delta_{\text{wall}} = k_c/(k_c + k_{\text{trap}})$ . The dotted line indicates a slope of 1. (b) Trap measurements (small open circles) of piezo-stage-induced linear and stepped motions of the wall against the axoneme tip (solid lines). The thin solid lines depict 3-fold enhanced difference signals.

no artificial steps are introduced or detected, we pushed the wall against the construct in a linear, as well as in a stepped manner using a piezo stage. We recorded the bead displacement, corrected for the construct stiffness and compared the detected motion with the wall motion (figure 3.6 b). We used steps of 20 nm and the speed was chosen to be in the range of typical microtubule growth speeds, on the order of 1  $\mu\text{m}/\text{min}$ . The solid lines depict the programmed motion of the piezo stage. The open circles indicate the response of the bead, after the linear correction. The difference between the detected motion and the wall motion (thin solid lines, magnified by a factor 3) shows no significant features that can be interpreted as steps of several tens of nanometer as observed in the microtubule growth experiments. On the other hand, the purposely-introduced steps of 20 nm are all correctly detected.

**Microtubule growth.** Microtubule growth was initiated by flowing tubulin into the sample, which was kept at a constant temperature of  $25 \pm 1^\circ\text{C}$ . Growth solutions contained MRB80 buffer (80 mM K-Pipes, 1 mM EGTA, 4 mM  $\text{MgCl}_2$ , pH 6.8) + 250  $\mu\text{M}$  GTP, and 5-10 mg/ml BSA. Growth solutions with XMAP215 additionally contained small amounts of Tris, Bis-Tris-propane, NaCl, DTT, and glycerol (resp. 0.8 mM, 0.8 mM, 26.4 mM, 80  $\mu\text{M}$ , and 0.8% in Exp 5 and 0.7 mM, 0.7 mM, 5.5 mM, 16  $\mu\text{M}$ , and 0.16% in Exp 6) and some protease inhibitors. Exp 3 in figure 3.3 and 3.4 (the control with buffer) contains data with very similar buffer additions. Recombinant XMAP215 was expressed in Sf+ insect cells, purified as described previously [153] and stored in liquid nitrogen. The protein concentration was determined with a Bradford assay and the molar extinction coefficient at 280 nm. To be able to periodically inject fresh solutions, we kept the sam-

ple open and maintained a small flow of buffer during our experiments, which led to a slow drop in protein concentration. This drop in concentration was estimated separately from the fluorescence changes caused by flow-through of fluorescent proteins. Undesired sticking of microtubule tips to surfaces was prevented by coating the home-built flow chamber with agarose and BSA or casein.

**Microtubule end mechanics.** To estimate the reduction in effective length  $\Delta L$  of a microtubule sheet or short protofilament under a compressive force  $F$  (figure 3.5 a), we use the following estimate of the extra amount of elastic energy that is stored in the sheet or filament:

$$\Delta E = \int_0^{L_{\max}} \frac{\kappa}{2} \left( \frac{1}{R_0} - \frac{1}{R_F} \right)^2 dl, \quad (3.1)$$

where  $R_0$  is the preferred radius of curvature,  $R_F$  is the force-induced (smaller) radius of curvature, and  $\kappa$  is the stiffness of the sheet or protofilament. The projected length, on the direction of detection, of a curved sheet or filament is given by  $L(R) = R \sin(L_{\max}/R)$ , where  $L_{\max}$  is the length of the sheet or filament when it is completely straight. We further use  $\Delta L = L(R_0) - L(R_F)$  and  $F = \Delta E/\Delta L$ . From this we estimate that for a sheet length of 125 nm, with a preferred radius of curvature of 250 nm and estimated stiffness 100 times less than a microtubule, full closure of the sheet under a compressive force of 2.5 pN leads to an observed length increase of only a few nm. On the other hand, the addition of a 60 nm long oligomer (preferred radius of curvature of 76 nm and estimated stiffness 500 times less than a microtubule) leads to an increase of several tens of nm, even when it is not supported by lateral connections to other protofilaments and/or stiffened by an associated XMAP215 molecule.

### 3.3.2 Step fitting algorithm

Evaluating possible step-like processes in otherwise noisy data sets is a returning problem in many biophysics studies. With non-constant step sizes and small numbers of step events, a classical method like evaluating pairwise distance distribution functions does not suffice. Similarly, if there is no clear distinction between noise and very small steps, it is not straightforward to separate background noise from true molecular events. We developed a simple, practical algorithm that allows us to distinguish pronounced step-like behavior from gradual non-stepped growth, and to return the size distribution of the steps that are distinguishable from the noise (see for more details our published article [143]). The sole assumption we make is that the original data is a step train with steps of varying size and duration, hidden in Gaussian noise.

The step-fitting algorithm involves 3 steps:

1. *Finding steps.* The algorithm starts by fitting a single large step to the data, finding the size and location of this first step based on a calculation of the Chi-squared. Subsequent steps are found by fitting new steps to the plateaus of the previous ones, each time selecting the most prominent one first. This eventually leads to a series of 'best'

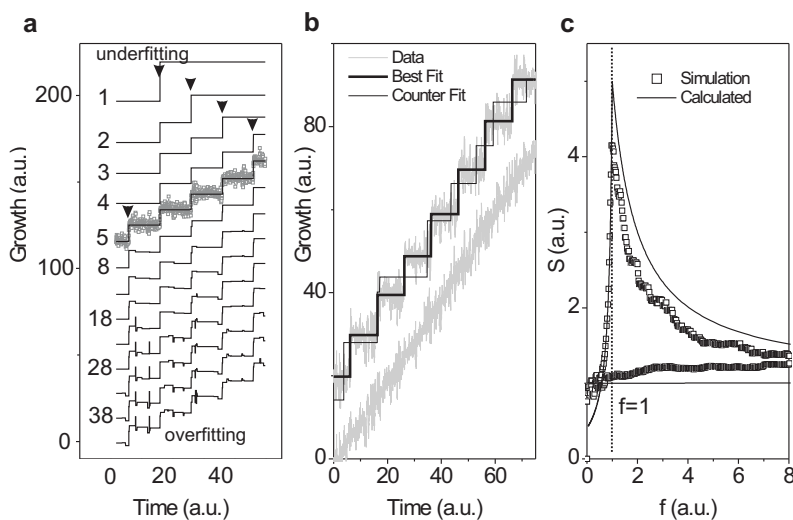


**Figure 3.7: Step fitting procedure.** (a) Iterations of the step-fitting algorithm on a simulated, noisy track of stepped data (step size 10 nm, RMS noise 2.5 nm). Curves are shifted vertically for clarity. The arrowheads point to every new step that is added to the fit. Underfitting means that significant steps in the data are not yet located, while overfitting means that merely noise is fitted. (b) A "best" fit (thick line) to noisy steps (step size 10 nm, RMS noise 2.5 nm) together with a "counter" fit (thin line, see text). The quality of these two fits differs strongly for a stepped signal, while for linear noisy growth (lower curve), the location of any step is arbitrary and the quality is equal. (c) Simulation result and calculation of the quality ratio  $S$  of best fit and counter fit, plotted vs. the relative number of fitted steps  $f$ . Upper curves are for a noisy stepped signal. Lower curve is for a noisy linear signal.  $S$  only peaks sharply if there are steps present, and if the correct number of steps is fitted (when  $f = 1$ ).

fits that differ only by one step (figure 3.7 a). The fits with a very low number of steps are likely to underestimate or 'underfit' the real number of steps in the data, whereas the small steps that are added in the last iterations will merely be fitting the noise, thereby 'overfitting' the data.

*2. Evaluating the quality of the step fits.* Each best fit in the series is compared to a 'counter fit' that has an equal number of steps as the original one but with step locations in between the step locations found by the best fit (figure 3.7 b). We define a 'step-indicator'  $S$  as the ratio between the Chi-squared of the counter fit and the Chi-squared of the best fit. When the number of steps in the best fit is very close to the real number of steps in the data, the value of  $S$  will be large (figure 3.7 c). If however the data are severely under- or overfitted, or when the data consist of gradual non-stepped growth, the value for  $S$  will be close to 1.

*3. Finding step distributions.* To construct a histogram of the step sizes, an 'optimal' fit (the one representing best the real steps in the data) has to be chosen. Ideally this is the one with the number of steps that produces the highest value of  $S$ . In practice, we

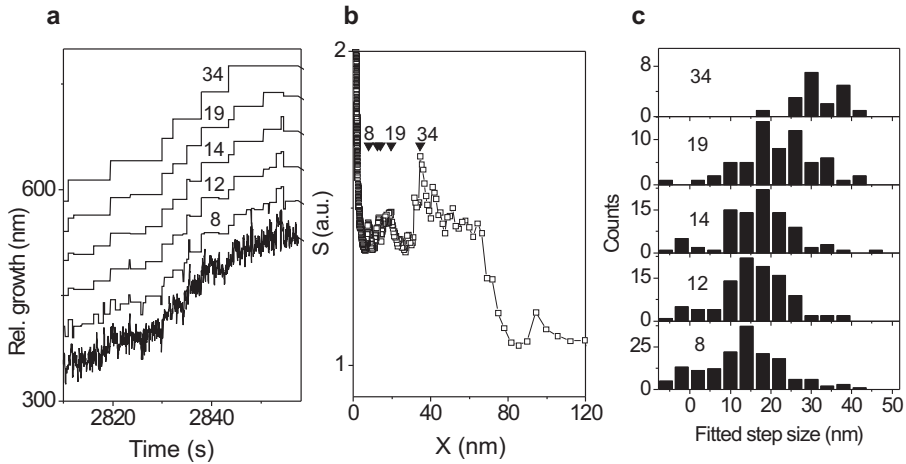


**Figure 3.8: Fitting experimental data for pure tubulin growth.** (a) Part of the raw data of a pushing microtubule with a series of increasingly finer step-fits. The numbers refer to the corresponding value of the parameter  $X$ , which represents the average size of the fitted steps.  $X$  is calculated as  $X = L_{\text{tot}}/N_f$ , where  $L_{\text{tot}}$  is the total length of the data trace and  $N_f$  is the number of fitted steps (b)  $S$  as a function of  $X$  for the complete data set, showing values above 1 over a wide range of length scales. Arrowheads and numbers refer to the specific step-fits shown in (a). (c) Associated step-distributions. Step sizes up to 20 - 30 nm are found even when the data are clearly 'overfitted' (for  $X = 8$ ). Note that overfitting mostly leads to the addition of alternating up and down steps.

usually choose a fit that appears to slightly overfit the data (see figure 3.8).

This procedure allows us to i) distinguish step-like growth from gradual non-stepped increases in length in a quantitative way, and ii) identify and quantify the steps that are distinguishable from the noise. The individual steps do not have to be equal in size or duration, and no a-priori assumptions about the signal to noise ratio are necessary. Of course, if the underlying steps are small compared to the noise, the algorithm will not be able to reliably distinguish a train of steps from linear non-stepped growth, which will manifest itself through a low value of  $S$ . If, as is the case for tubulin growth, the data consist of combinations of steps that are large and small compared to the noise, the algorithm will ensure that we find the sizes of the large ones. However, the optimal fit that we find based on the size of the large steps, will also put arbitrary steps on the rest of the data. A recent study compared the performance of different step detection methods and found that the Chi-squared based algorithm, developed in our group, is the simplest to optimize and has excellent temporal resolution [156].

In figure 3.8 we show the result of this procedure for the growth data with pure tubulin presented in this chapter. Note that in this case a substantial fraction of the growth occurs through steps that are indistinguishable from the noise and/or linear growth. Our algorithm is designed to find the sizes of steps that are distinguishable from the

noise, but also forces steps on the rest of the data. These last step sizes vary strongly when we vary the number of steps fitted to the data, but the 20 - 30 nm peak remains present even when we clearly start to overfit the data (figure 3.8 c).

### 3.4 Towards understanding the molecular mechanism of interaction between XMAP215 and tubulin

Our high-resolution observations suggested that XMAP215 might template formation of long tubulin oligomers. XMAP215 is an elongated protein that could accommodate along its length 7-8 tubulin dimers. Previously, it was shown that incubation of XMAP215 with tubulin at 4°C yielded formation of tubulin partial rings in a complex with XMAP215 [64]. Results from microtubule binding studies suggest that XMAP215 comprises two tubulin binding domains: a 'high-affinity' domain (with dissociation constant  $K_D < 1 \mu\text{M}$ ) near the middle of the protein and a 'moderate-affinity' domain ( $K_D \approx 2\text{-}5 \mu\text{M}$ ) broadly distributed near the N terminus [120, 157].

In an attempt to find out whether XMAP215 could bind multiple dimers along its length, at similar experimental conditions as the high-resolution measurements, we used fluorescently speckled microtubules and fluorescence correlation spectroscopy. The formation of tubulin oligomers with sizes comparable to the XMAP215 protein itself, should be easily observed with both methods. In our experiments, we did not identify big oligomers induced by the presence of XMAP215. An independent technique and further controls would be necessary to exclude a technical artifact. For example, the presence of the fluorescent dye on tubulin might interfere with the XMAP215-tubulin interaction. However, it is still possible that XMAP215 interacts with the fluorescently-labelled tubulin, but binds only 1-3 tubulin dimers. In this case both methods presented here would fail to identify the complex formation due to the limited resolution. Our results and observations are presented in this section.

#### 3.4.1 Speckled microtubules

Fluorescence speckle microscopy (FSM) was developed to visualize movement, assembly and turnover of microtubules and actin filaments in living cells [158, 159]. When a low amount of fluorescently-labelled tubulin is microinjected into cells, microtubules appear 'speckled'. Both *in vivo* and *in vitro* experiments confirmed that microtubules obtain the fluorescent speckle pattern from the stochastic association of labelled and unlabelled tubulin subunits with the growing ends [160, 161].

We used FSM to investigate *in vitro* the assembly of microtubules in the absence and in the presence of XMAP215. XMAP215 was pre-incubated with the labelled fraction of tubulin. By analyzing the speckle pattern along microtubules we were aiming to gain information on the XMAP215-induced oligomerization of tubulin.

**Principles of speckle image formation.** Microtubules assemble by random association of tubulin subunits (figure 3.9 a). When a fraction  $f$  of labelled tubulin is present

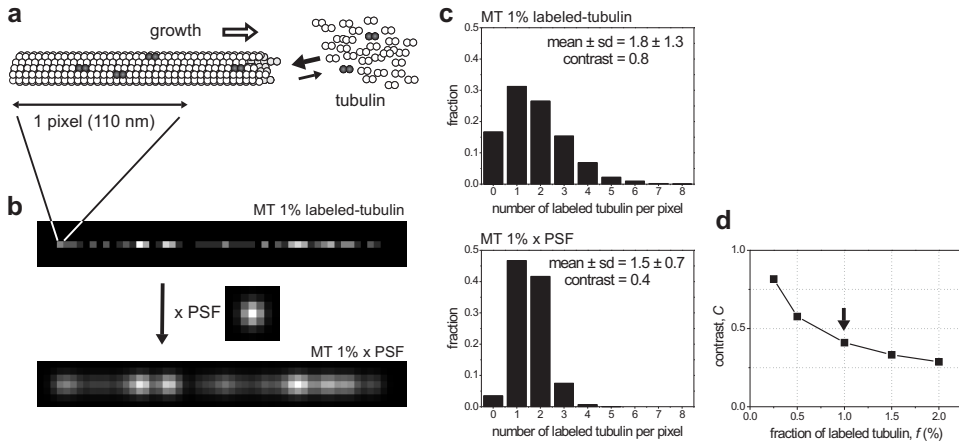


**Figure 3.9: Speckle formation.** (a) Schematic drawing of a microtubule growing in the presence of a small fraction of fluorescently labelled tubulin dimers. The microtubule elongates by random association of tubulin subunits at the growing end. (b) Pixel intensity along a theoretical microtubule 'grown' from a pool of tubulin containing 1% labelled tubulin. Each pixel corresponds to 110 nm microtubule length. The pixel intensity is given by the number of fluorescent subunits and was calculated using a discrete binomial distribution. The microtubule is  $5.5 \mu\text{m}$  in length. When the theoretical microtubule is 'imaged' with our confocal microscope, the pixel distribution is convolved with the microscope point spread function (PSF). The PSF was experimentally determined from images of a surface sparsely coated with rhodamine-labelled tubulin. (c) Distributions of fluorescent subunits per pixel along microtubules, theoretically assembled at similar conditions with the ones shown in (b). The distributions show the percentage of pixels with a corresponding number of fluorescent tubulin subunits and were constructed from theoretical microtubules with a total length of  $550 \mu\text{m}$ . The convolution with the PSF reduces the pixel contrast,  $C = \text{sd}/\text{mean}$ . (d) Calculated speckle contrast,  $C$ , as a function of labelled-tubulin fraction.

in the tubulin pool, the fluorophore distribution along microtubules is described by a discrete binomial distribution (see Methods). The microtubule image through a microscope is a convolution of the fluorophore distribution along the microtubule with the point spread function (PSF) of the microscope. Figure 3.9 b shows an example of a theoretical microtubule and the effect of PSF on the speckle pattern.

The PSF of our confocal microscope can be approximated by a Gaussian with a standard deviation of 1 pixel (110 nm). One pixel corresponds in length to  $N = 180$  tubulin dimers. As  $N$  is sufficiently high, the distribution of fluorescent dimers per pixel can be approximated with a normal distribution with a mean given by  $m = Nf$  and a standard deviation given by  $\text{sd} = \sqrt{Nf(1-f)}$ . Speckle contrast was defined as  $C = \text{sd}/m = \sqrt{(1-f)/(Nf)}$  [160], which can be approximated by  $C = 1/\sqrt{Nf}$  for low fractions of fluorescent subunits,  $f$ . This formula suggests that the contrast,  $C$ , increases when decreasing the fraction of labelled tubulin,  $f$  (figure 3.9 d). In practice, how low  $f$  can be is limited by the fluorophore properties and the imaging system. The convolution with the PSF of the fluorophore distribution per pixel will effectively lower

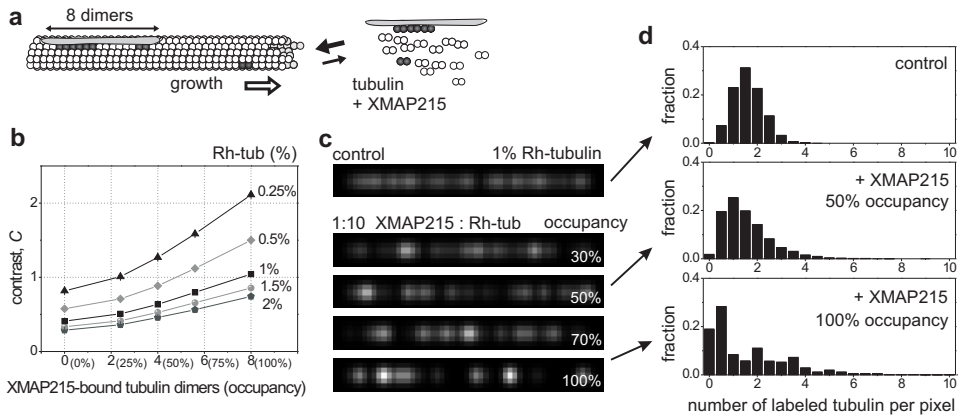


**Figure 3.10: Theoretical speckled microtubules in the presence of XMAP215.** (a) Schematic drawing of a microtubule assembled from a tubulin pool containing a small fraction of fluorescently labelled dimers that was pre-incubated with XMAP215. We assume here that XMAP215 forms stable complexes with the labelled tubulin that are subsequently incorporated into the growing microtubules. (b) Pixel contrast,  $C$ , as a function of the XMAP215 occupancy with labelled tubulin subunits. XMAP215-induced oligomerization results in increased speckle contrast. Calculations were performed using discrete binomial distributions (see Methods) for different labelled tubulin fractions, indicated in the graph. (c) Images and (d) pixel intensity distributions of theoretical microtubules assembled from 1% labelled tubulin in the absence and in the presence of XMAP215 in the pre-incubation step (1:10 XMAP215:labelled-tubulin). When more tubulin binds to XMAP215, fewer and brighter speckles are formed. Maximum occupancy corresponds to 8 tubulin dimers bound to each XMAP215 molecule. The distributions were determined from a total microtubule length of 550  $\mu\text{m}$ .

the speckle contrast (figure 3.9 b and c). Previous studies found that the experimental optimal contrast is obtained when  $f$  is in the range of 0.5% to 2% [161, 162].

**Calculated speckle distributions in the presence of XMAP215.** In our experiments we pre-incubate the labelled tubulin fraction with XMAP215. Our hypothesis is that XMAP215 is inducing oligomerization of tubulin. We assumed that the labelled tubulin subunits bind stochastically to XMAP215 molecules and the XMAP215-tubulin complexes are stable and can incorporate into the growing microtubule. A fully occupied XMAP215 molecule carries 8 tubulin dimers, arranged in a straight line. In our calculations we considered several levels of XMAP215 occupancy with tubulin, occupancy defining the percentage of the molecule length filled with tubulin dimers. 50% occupancy means that, on average, 4 tubulin dimers are bound to one XMAP215 molecule. We further assumed that the number of dimers bound to each XMAP215 molecule also follows a discrete binomial distribution. The XMAP215 molecules carrying labelled-tubulin and the tubulin dimers not associated with XMAP215 bind stochastically to the growing microtubule end (figure 3.10 a).

Figure 3.10 shows the effect of XMAP215-induced oligomerization on the pixel intensity distributions. In our calculations we considered a ratio of XMAP215 to labelled

tubulin of 1:10, similar to the experimental conditions. For various labelled tubulin fractions,  $f$ , and XMAP215 occupancy, we determined an increase in the pixel contrast in the presence of XMAP215, as compared with the absence of the protein (figure 3.10 b). With XMAP215 we expect fewer, but brighter speckles along microtubules (figure 3.10 c and d).

### Experimental results and discussion

We assembled microtubules in the presence of 0.5%-2% rhodamine-labelled tubulin (figure 3.11 a) and we compared the pixel intensity distributions along microtubules in the absence and in the presence of XMAP215.

The pixel intensity contrast and distributions measured in the absence and in the presence of XMAP215 in the pre-incubation step were very similar for all experimental conditions investigated. One example is shown in figure 3.11 b and compared with the expected difference in the theoretical distributions at similar conditions (figure 3.11 c). The difference predicted by the calculations are not observed in the experimental data. This observation could have several explanations. It is possible that upon dilution in the polymerization mix, the rhodamine tubulin bound to XMAP215 is exchanged with the unlabelled tubulin. In our experiments the amount of unlabelled tubulin in solution is typically 1000 fold higher than the amount of XMAP215 molecules. Therefore the kinetics of the XMAP215-tubulin interaction might favor the release of the labelled tubulin and rebinding of unlabelled dimers. The alternative explanation is that XMAP215 does not bind multiple tubulin subunits. We therefore used an additional technique (fluorescence correlation spectroscopy) to investigate directly the interaction between XMAP215 and tubulin in solution (section 3.4.2).

### Methods

**Theoretical distributions.** The number of labelled tubulin dimers per pixel, the number of XMAP215 molecules per pixel, and the number of labelled tubulin bound to each XMAP215 molecule were determined using discrete binomial distributions.

The binomial distribution gives the discrete probability distribution  $P_p(n|N)$  of obtaining exactly  $n$  successes ( $n$  subunits incorporated in a pixel-size length of a microtubule) out of  $N$  trials (total number of tubulin subunits comprised in a pixel-size length,  $N = 108$  for a 110 nm pixel), where the result of each trial is true with probability  $p$  and false with probability  $q \equiv 1 - p$ . In our case, the probability  $p$  is given by the fraction,  $f$ , of labelled subunits or of XMAP215 molecules. The binomial distribution is therefore given by:

$$P_f(n|N) = \frac{N!}{n!(N-n)!} f^n (1-f)^{N-n} \quad (3.2)$$

The number of labelled tubulin dimers bound to each XMAP215 molecule is calculated in a similar way, with  $N = 8$  and probability given by the occupancy (percentage of XMAP215 filled with dimers).



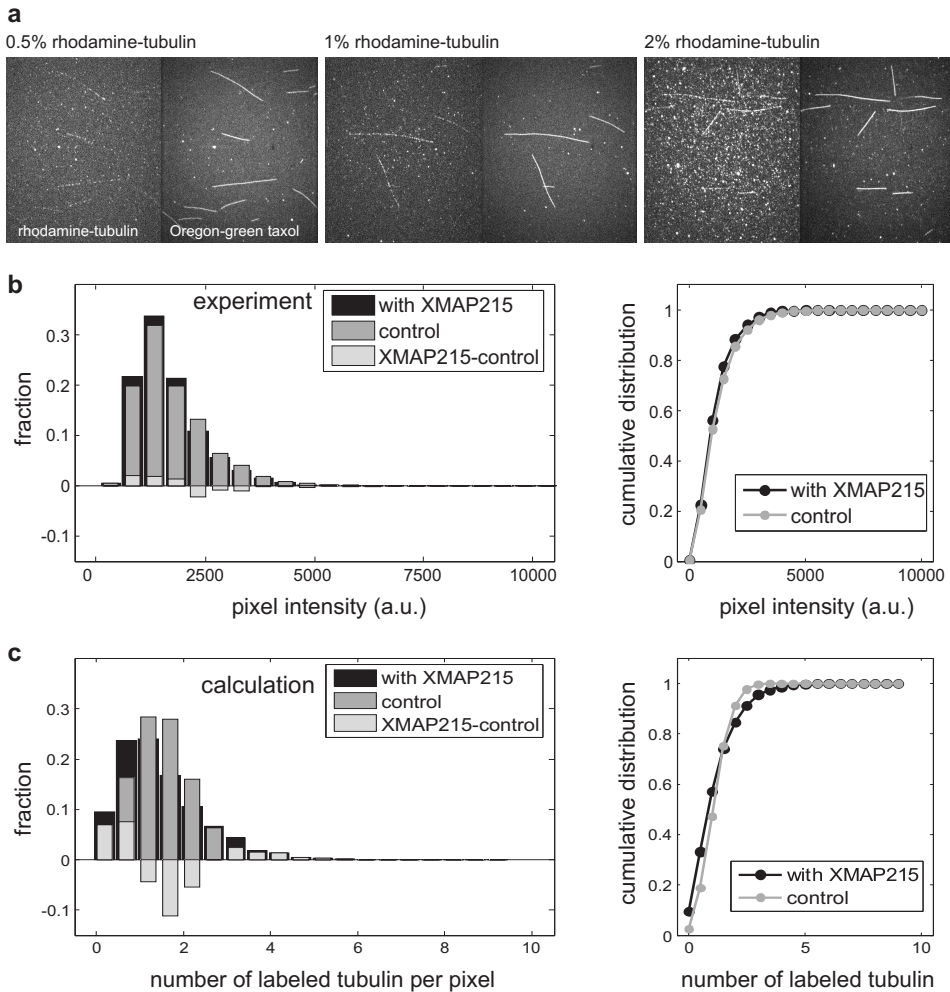


**Figure 3.11: Speckled microtubules assembled *in vitro*.** (a) Dual color images (rhodamine-tubulin and Oregon green taxol) of microtubules assembled from a tubulin pool containing indicated fractions of rhodamine-labelled tubulin. Microtubules were imaged with a spinning-disc confocal microscope. (b) Pixel intensity distributions and cumulative distributions for microtubules assembled in the absence and in the presence of XMAP215. XMAP215 was pre-incubated with the rhodamine-labelled tubulin in a ratio of 1:10 XMAP215:tubulin. In the polymerization mix, the fraction of labelled tubulin was 1%. (c) Pixel intensity distributions and cumulative distributions calculated for theoretical microtubules assembled at similar conditions as in (b). We assumed that each XMAP215 molecule had bound on average 4 tubulin dimers (50% occupancy).

***In vitro assembly of speckled microtubules.*** Microtubules were assembled by incubation of 20  $\mu\text{M}$  tubulin, containing 0.5%, 1%, or 2% rhodamine-labelled tubulin and 10% biotin-labelled tubulin, with 1 mM GMPCPP (Jena Bioscience, Germany) in MRB80 at 36°C for 50 minutes. In the XMAP215 containing samples, the fraction of rhodamine-labelled tubulin was pre-incubated with XMAP215 as follows. A mix of 5  $\mu\text{M}$  rhodamine-tubulin, 0.5  $\mu\text{M}$  XMAP215 and 1 mM GTP was incubated for a couple of minutes at room temperature or, alternatively, for up to 1 h on ice. After incubation, the XMAP215 mix was diluted in the polymerization mix to the final concentration of rhodamine-tubulin. The incubation was done in the presence of GTP to avoid artifacts of oligomer formation due to spontaneous nucleation. The microtubules were assembled in the presence of GMPCPP to suppress dynamic instability. In this way, the possible XMAP215-templated oligomers formed in the incubation step are locked in the microtubule lattice. Otherwise, in the presence of GTP, microtubules will undergo several polymerization-depolymerization cycles and the rhodamine-tubulin comprised in oligomers, if formed, would be randomized. After polymerization, the stable GMPCPP microtubules were diluted with a taxol solution containing 3  $\mu\text{M}$  Oregon green-labelled taxol (Invitrogen) and 7  $\mu\text{M}$  unlabelled taxol. The green taxol marks the entire length of the microtubule, allowing for microtubule localization when imaging the sample. Tubulin and unlabelled taxol were purchased from Cytoskeleton.

***Confocal imaging of microtubules and pixel intensity distributions.*** Speckled microtubules were attached via streptavidin-biotin bonds to a functionalized surface. The surfaces of cleaned coverslips were covered with a compound layer of biotin-BSA and streptavidin as described in section 3.3.1. Microtubules were imaged with a dual-color spinning-disc confocal microscope, as described in section 4.3. Microtubules were localized by imaging the Oregon green taxol and a second image of the rhodamine-tubulin in the same field of view was recorded. Typical exposure was 2 s for the rhodamine image. Images were captured by a cooled EM-CCD camera (C9100, Hamamatsu Photonics) that has 16  $\mu\text{m}$  square pixels and a 14 bit linear range of photon detection. Figure 3.11 a shows images of speckled microtubules grown at different fractions of rhodamine-tubulin.

Digital images were further analyzed in Matlab (MathWorks) to extract the pixel intensity distributions along microtubules. First, the images were corrected for the spatial illumination profile of our set-up, that had a 2D-Gaussian shape. Line profiles were drawn on the Oregon green-taxol images to localize the microtubules. The line coordinates were further used in the red-channel images to measure intensity line profiles of rhodamine-speckles on individual microtubules. One microtubule profile was the sum of three adjacent line scans to account for the PSF of the microscope. In one sample 30-90 microtubules were analyzed, comprising a total length of 200-500  $\mu\text{m}$ .

### 3.4.2 FCS measurements on XMAP215-tubulin complex formation

Fluorescence correlation spectroscopy (FCS) allows for the determination of the diffusion characteristics of fluorescent molecules and their interaction with other particles [163]. We used FCS to measure diffusion coefficients of tubulin in dilute solutions in the absence and in the presence of XMAP215, in an attempt to investigate XMAP215-tubulin complex formation in solution.

**Principles of FCS.** In FCS the kinetics of fluorescent molecules are measured by monitoring the fluctuations of their emission intensity in a confocal excitation volume [164]. The detection volume is defined by the diffraction-limited focal spot of a strongly focused laser beam in combination with a confocal detection pinhole, leading to a Gaussian intensity profile. Fluorescent molecules enter and exit the excitation volume due to Brownian motion giving rise to fluctuations in the detected emission intensity. In FCS, the detection volume is typically in the femtoliter range, i.e. approximately the volume of a bacterial cell, and concentration of fluorescent molecules is in the nanomolar range, resulting in only a few molecules being present in the detection volume. The auto-correlation function,  $G(\tau)$ , of the recorded intensity signal is related to the characteristic diffusion time,  $\tau_d$ , during which a molecule resides in the observation volume. Equation 3.3 gives the analytical form of the auto-correlation function when two populations of diffusing particles are present in solution:

$$G(\tau) = \frac{1}{N_1} \left( \frac{1}{1 + \frac{\tau}{\tau_{d1}}} \right) \sqrt{\frac{1}{1 + f^2 \frac{\tau}{\tau_{d1}}}} + \frac{1}{N_2} \left( \frac{1}{1 + \frac{\tau}{\tau_{d2}}} \right) \sqrt{\frac{1}{1 + f^2 \frac{\tau}{\tau_{d2}}}} \quad , \quad (3.3)$$

where  $N$  is the average number of fluorescent particles within the excitation volume and can be calculated, for a single diffusing species, from the initial correlation amplitude,  $G(\tau \rightarrow 0) = 1/N$  (figure 3.12).  $f$  is the ratio between the axial,  $\omega_z$ , and lateral,  $\omega_{xy}$ , dimensions of the observation volume.  $\omega_{xy}$  and  $\omega_z$  denote the radii of the Gaussian profile at  $1/e^2$  of its maximal intensity. In a calibrated observation volume with an exact Gaussian profile,  $1/e^2$  radial dimension  $\omega_{xy}$ , and known  $f$ , the diffusion coefficient,  $D$ , of a fluorescent species can be determined as  $D = \omega_{xy}^2 / 4\tau_d$ , where  $\tau_d$  is evaluated from a fit to the auto-correlated signal (figure 3.13).

## Results and discussion

Figure 3.12 shows the auto-correlation function of the fluorescence signal detected by FCS in an aqueous solution of 2.5 nM Rhodamine 6G. The diffusion coefficient of Rhodamine 6G is known,  $D = 2.8 \times 10^{-10} \text{ m}^2/\text{s}$ , at 20°C [166], and therefore we used the Rhodamine 6G samples to calibrate our system (determining  $\omega_{xy}$  and  $f$ ). The dimensions of the focal volume were determined from a one-component fit to the auto-correlation function (figure 3.13, left) and were typically found to be  $\omega_{xy} = 470 \text{ nm}$  and  $f = 10$  ( $\omega_z = 4700 \text{ nm}$ ). Figure 3.13, left, also shows the fit residual, representing the difference between the fitted and the measured autocorrelation function. The noisy

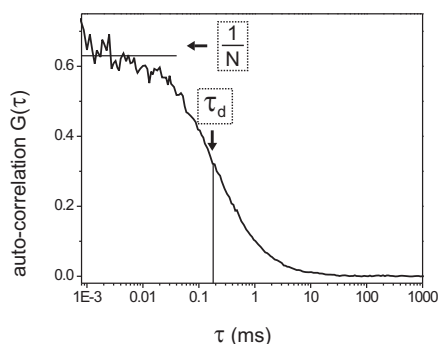


**Figure 3.12: Auto-correlation function measured in FCS.** The intensity signal was recorded in a solution of 2.5 nM Rhodamine 6G for 200s and fed into a hardware correlator that computes the auto-correlation of the signal as a function of the lag time  $\tau$ . From the auto-correlation function, the number of particles in the detection volume,  $N$ , and the characteristic diffusion time of the particles in the detection volume,  $\tau_d$ , can be determined (see text).

residual is flat indicating that our observation volume has a Gaussian shape. A wavy shape pattern present in the residual would indicate a non-Gaussian observation volume or a wrong assumption in the fitted function (for example a one-component fit of a signal from a two-component sample) [167].

In control samples we measured a diffusion coefficient for tubulin of  $(4.0 \pm 0.3) \times 10^{-11} \text{ m}^2/\text{s}$  (table 3.2), similar to previously reported values measured using FCS [168]). The theoretically predicted value for the diffusion coefficient of a single tubulin dimer,  $5.5 \times 10^{-11} \text{ m}^2/\text{s}$  (table 3.2), is somewhat higher than our measurements. One expla-

tubulin [nM]	XMAP215	ratio tub : xmap	$D$ $\times 10^{-11} \text{ (m}^2/\text{s)}$
<b>experiment</b>			
0.2	-	-	$4.0 \pm 0.3$
0.4	-	-	$3.6 \pm 0.1$
0.2	+	3 : 1	$3.4 \pm 0.2$
0.4	+	1 : 1	$3.9 \pm 0.5$
<b>theory</b>			
tubulin dimer			5.5
XMAP215 + 1 tubulin dimer			3.9
XMAP215 + 7 tubulin dimers			1.7

**Table 3.2: Diffusion coefficients of tubulin in the absence and in the presence of XMAP215.** The experimental values were evaluated from a two-component fit to the auto-correlation function (see also figure 3.13). The diffusion coefficient of the fast component (free rhodamine) was fixed to  $3.0 \times 10^{-11} \text{ m}^2/\text{s}$ . The theoretical values were calculated by using the formula for the translational diffusion coefficient of rod like molecules [165] (see also Methods).

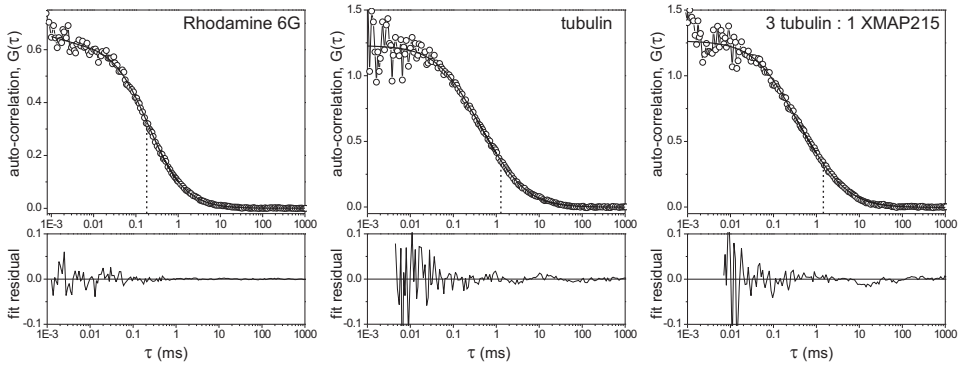


**Figure 3.13: FCS measurement of tubulin-XMAP215 complex.** The top panels show the auto-correlation function (open symbols) of the fluorescence signal recorded in a solution containing 2.5 nM Rhodamine 6G (left) and solutions containing 0.2 nM rhodamine-labelled tubulin in the absence and in the presence of XMAP215 (middle and right). The solid line is the respective two-component fit. The dotted lines indicate the characteristic diffusion time,  $\tau_d$ , as evaluated from the fit. The lower panels show the difference between the auto-correlation function and the fit.

nation could be that the tubulin samples contain not only single dimers, but rather a mixed population of small oligomers that cannot be distinguished separately. The auto-correlation function and the residual are plotted in figure 3.13, middle. A two-component model was used to fit the experimental auto-correlation function, in order to account for the presence of free rhodamine dye (remainder from the tubulin labelling process). The diffusion coefficient of rhodamine (TAMRA, tetramethyl-rhodamine) was fixed to  $3.0 \times 10^{-11} \text{ m}^2/\text{s}$ , value that was measured in a separate experiment. We noticed that the fit residual displays a wavy shape. This indicates the presence of multiple components in our sample, as we can exclude artifacts induced by a non-Gaussian shape of the observation volume (see the flat residuals in the case of a Rhodamine 6G sample, figure 3.13 left). There are limits, however, to the resolution of detecting multiple species. Theoretical and experimental studies show that the distinction between different molecular species depends on differences in their molecular brightness, size, and the concentration of each component in solution [169]. Molecules must differ in diffusion time by a factor of  $\sim 1.6$  to be distinguished easily (more than 4 dimers in the case of tubulin, as estimated from calculations). From our FCS observations, if oligomers are present in the tubulin solution, their size must be small (2-3 dimers) or, if bigger, they represent a minority.

A theoretical calculation of diffusing particles predicts that a tubulin-XMAP215 complex would have a diffusion coefficient 1.4-fold lower when 1 tubulin dimer is bound to XMAP215 and up to 3.3-fold lower when 7 tubulin dimers are bound (table 3.2). Given the FCS resolution we would not be able to clearly identify XMAP215-tubulin complexes with less than 3-4 tubulin dimers bound to XMAP215. In the presence of XMAP215 we measured auto-correlation curves and diffusion coefficient of tubulin sim-

ilar to what we measured in the absence of XMAP215 (table 3.2). Figure 3.13 shows that the fit residual has also a slightly wavy pattern, similar to the tubulin solutions. As rationalized above, this indicates the presence of multiple components. The XMAP215-tubulin sample might contain a mixed population of tubulin single dimers, small oligomers, and XMAP215-tubulin complexes. We can not resolve whether these complexes are formed, but if so their size must correlate with only 1 or 2 tubulin dimers bound to XMAP215, given the limited resolution of FCS. If bigger oligomers or XMAP215-tubulin complexes are present, they represent a minority. It is also possible that XMAP215-tubulin complexes dissociate upon dilution to the nanomolar concentrations used in FCS. Another issue could be the presence of the fluorescent dye on tubulin, which could interfere with the interaction between XMAP215 and tubulin.

Further investigations are required to distinguish whether XMAP215-complexes are formed and to determine their typical size. A better option to study XMAP215-tubulin interaction using FCS is to measure nM labelled XMAP215 in the presence of  $\mu\text{M}$  concentrations of unlabelled tubulin.

## Methods

**Sample preparation.** For the control samples, rhodamine-labelled tubulin (Cytoskeleton) was diluted to  $6\ \mu\text{M}$  in MRB80 supplemented with  $1.2\ \text{mM}$  GTP and  $2.4\ \text{mg/ml}$  BSA. The tubulin solution was centrifuged for 10 min at  $16,100\ \text{x g}$  at  $4^\circ\text{C}$  to remove protein aggregates and further diluted to a final concentration of  $0.2\ \text{nM}$  or  $0.4\ \text{nM}$  in assay buffer ( $40\ \text{mM}$  K-Pipes,  $0.5\ \text{mM}$  EGTA,  $2\ \text{mM}$   $\text{MgCl}_2$ , pH 6.8) +  $0.3\ \text{mg/ml}$  BSA. According to the manufacturer, the labeling stoichiometry of tubulin is 1-2 dyes per tubulin dimer. In solution, we measured 20-30% free rhodamine dye from the total number of fluorescent molecules.

For the samples containing tubulin and XMAP215, rhodamine-labelled tubulin was diluted to  $6\ \mu\text{M}$  and centrifuged similar to the preparation for the control samples. The clarified tubulin ( $5\ \mu\text{M}$ ) was incubated for 1-2 min at room temperature with unlabelled XMAP215 at two different ratios of XMAP215:tubulin, 1:1 and 1:3. In this incubation step a total of  $1\ \text{mM}$  GTP and  $2\ \text{mg/ml}$  BSA was present in solution. The samples were further diluted to  $0.2\ \text{nM}$  or  $0.4\ \text{nM}$  tubulin, in a similar way as the control samples.

Diluted protein solutions were transferred into the wells of a glass bottom microplate (Whatman). The microplate wells used for measuring were first passivated, to reduce protein loss on surfaces, by incubation with  $2.5\ \text{mg/ml}$  BSA and subsequently rinsed with MRB80. All FCS measurements were performed in a sample volume of  $100\ \mu\text{l}$  at room temperature,  $21 \pm 1^\circ\text{C}$ .

**FCS measurements.** Experiments were performed on a home-built FCS setup. The laser beam of a frequency doubled Nd:YAG laser at  $532\ \text{nm}$  (Crystalaser) is coupled into an inverted optical microscope (Nikon Eclipse TE2000-U) and focused into the sample by a  $63\times$   $1.4\ \text{NA}$  oil immersion objective (Nikon). The beam diameter was expanded through a two-lens telescope to slightly underfill the objective aperture. Fluor-

rescent signal from the sample and the excitation laser light are separated by a dichroic mirror (Chroma, z532rdc) in combination with a long-pass filter (Chroma, hq550lp) that blocks the remaining laser light reflected from the sample. The fluorescence light passes through a pinhole (50  $\mu\text{m}$  in diameter), which blocks the photons produced outside the focal volume, and is detected by an avalanche photodiode (APD, Eg&G). The APD signal is fed into a hardware correlator (ALV/5000E), which computes the auto-correlation function of the fluorescence intensity signal.

Both the diameter of the excitation beam and the pinhole size have been chosen to minimize possible artifacts like a non-Gaussian intensity distribution in the focus [167]. Typical laser power at the sample was between 50-100  $\mu\text{W}$ . In this regime the photo-bleaching should be negligible. The system was calibrated by collecting FCS curves of an aqueous solution of Rhodamine 6G molecules prior to each measurement. The auto-correlation of tubulin and tubulin-XMAP215 were typically recorded for 200 s and all samples were measured 3 times. The curves were further analyzed in Mathematica by fitting a two-component model (free dye and tubulin dimers) to determine the diffusion coefficients,  $D$ , of tubulin.

**Theoretical diffusion coefficients of rod-like particles.** We used a model described in [165]. For a cylinder of length  $L$  and diameter  $d$ , the translational diffusion coefficient,  $D$ , can be expressed as:

$$D = \frac{k_B T}{3\pi\eta L} \left( \ln\left(\frac{L}{d}\right) + 0.312 + 0.565\left(\frac{d}{L}\right) - 0.1\left(\frac{d}{L}\right)^2 \right), \quad (3.4)$$

where  $k_B T$  is the Boltzmann factor and  $\eta$  is the viscosity of the solvent. This model is correct for  $L/d$  approximately in the range 2 - 30. For the XMAP215-tubulin complexes we evaluated  $L$  from the total molecular volume and the average diameter,  $d$ , as estimated from published values.

### 3.5 Additional remarks and discussion

Two recently published studies [27, 150] report additional information on the molecular details of microtubule growth and the interaction between XMAP215 and tubulin. Here our data is further discussed in the light of this new information.

At high spatial resolution, we measured fast length increases during microtubule polymerization corresponding to 2-3 tubulin dimers in size. The fast length increases could be caused either by instantaneous addition of small oligomers or subsequent addition of single dimers. We cannot resolve between the two possibilities due to the limited response time of our system (i.e. presence of drag forces on the bead-axoneme construct) and due to the time resolution of our detection method, limited to video rate. On the other hand, small tubulin oligomers are most probably present in our sample as we assembled microtubules in the presence of a relatively high amount of  $\text{Mg}^{2+}$  ions, which was previously shown to induce tubulin oligomerization [168]. Considering the presence of small oligomers and previous biochemical data suggesting that

GDP-tubulin can incorporate at the growing end [50, 170], we think that oligomer addition can be a mechanism contributing to microtubule elongation, as discussed earlier in this chapter (section 3.2). In contrast, a recent study by Scheck et al. [150] proposes that microtubule assembly takes place predominantly via single dimer addition. Using an optical tweezers based technique similar to the one presented in this thesis, the authors monitored microtubule assembly dynamics at high spatial and temporal resolution. However, the results from Scheck et al., and their interpretation thereof, cannot be directly compared with our results due to differences in the experimental conditions (tubulin concentration,  $Mg^{2+}$  ion concentration, temperature) and the differences between the two methods (nucleation sites used - axoneme vs microtubule and presence of an increasing force vs constant force against the microtubule, details that might affect the response time). Further experiments would be necessary to resolve the issue.

We also measured fast length increases during microtubule growth in the presence of XMAP215, with sizes up to the length of the XMAP215 protein itself. The sequence of molecular events underlying the XMAP215-catalyzed addition of tubulin at the growing end is still under discussion. We proposed two possible scenarios as exemplified in figure 3.5 b. One possibility is that XMAP215 templates formation of large oligomers in solution, which are subsequently incorporated at the growing microtubule tip, or XMAP215 first binds at the growing end where it facilitates addition of tubulin dimers along its length. Using FSM and FCS we did not detect formation of large oligomers in solution, although it was not clear whether we were not able to measure the large oligomers due to the experimental realization, e.g. low regime of protein concentrations and the presence of fluorescent dye on tubulin. Our FCS experiments suggested that, rather, only 2-3 dimers bind to XMAP215 in solution. Recently Brouhard et. al [27] also reported new insights into XMAP215-tubulin interactions by visualizing single XMAP215-GFP proteins interacting with dynamic microtubules. The authors propose that XMAP215 binds free tubulin in a 1:1 complex forming a closed configuration. The complex 'surfs' on the growing ends by a diffusion-facilitated mechanism, where it catalyzes the addition of multiple tubulin dimers (~300 at the specific experimental conditions). The idea that XMAP215 forms a complex with only 1 tubulin dimer correlates with our FSM and FCS observations. However, this idea is in contrast with previous experiments, where incomplete rings of tubulin in a complex with XMAP215 were observed to form in solution, the complex size matching the length of the XMAP215 protein [64]. However, taking into consideration our measurements in solution and the recently published data of Brouhard et. al, the second mechanism proposed by us could underly the fast length increases observed in our high-resolution data: XMAP215 at the tip facilitates the addition of tubulin subunits along its length. The multiple interaction sites between XMAP215 and tubulin would also insure the presence of the protein at the microtubule lattice for a while upon binding, supporting our observation of stepped depolymerization that indicates 'obstacles' on the microtubule lattice.



***Acknowledgements***

The major part of the work presented in this chapter is published in [143]. I would like to thank Jacob Kerssemakers, with whom I collaborated, for developing the experimental method and the step fitting algorithm and for performing first experiments together. I also thank Tim Noetzel, Kazuhisa Kinoshita and Tony Hyman for kindly providing the XMAP215 protein for us. For the FCS set-up and help with experiments I would like to thank Thomas Kalkbrenner and Sander Tans.

[143]: Kerssemakers JWJ, Munteanu EL, Laan L, Noetzel TL, Janson ME, Dogterom M (2006) Assembly dynamics of microtubules at molecular resolution. *Nature* **442**: 709-712



---

## Reconstitution of a microtubule plus-end tracking system *in vitro*

*Growing microtubule plus ends have emerged as dynamic regulatory sites in which specialized proteins, called plus-end-tracking proteins (+TIPs), bind and regulate the proper functioning of microtubules [19,20,22,23]. However, the mechanism by which +TIPs regulate microtubule dynamics and the molecular mechanism underlying the +TIP ability to track the growing end are not well understood. An in vitro approach is necessary to understand the effect of individual +TIPs. Here we report the in vitro reconstitution of a minimal plus-end tracking system consisting of the three fission yeast proteins Mal3, Tip1 and the kinesin Tea2. Using time-lapse total internal reflection fluorescence microscopy, we show that the EB1 homologue Mal3 has an enhanced affinity for growing microtubule end structures as opposed to the microtubule lattice. This allows it to track growing microtubule ends autonomously by an end recognition mechanism. In addition, Mal3 acts as a factor that mediates loading of the processive motor Tea2 and its cargo, the CLIP170 homologue Tip1, onto the microtubule lattice. The interaction of all three proteins is required for the selective tracking of growing microtubule plus ends by both Tea2 and Tip1. Our results dissect the collective interactions of the constituents of this plus-end tracking system and show how these interactions lead to the emergence of its dynamic behavior. We expect that such in vitro reconstitutions will also be essential for the mechanistic dissection of other plus-end tracking systems.*

Microtubules are polar, dynamic tubulin polymers that have a variety of functions in eukaryotic cells [6]. The dynamics and the spatial organization of microtubules are regulated by several highly conserved microtubule-associated proteins. An important class of these proteins, called +TIPs, accumulates selectively at growing microtubule plus ends in living cells. A wealth of fluorescence microscopy studies in various organisms have identified numerous +TIPs that belong to conserved subfamilies: CLIP-170 [171], APC [172], EB1 [173], CLASPs [174], p150 [175] and spectraplakins [176]. In the fission yeast *Schizosaccharomyces pombe*, classical genetics combined with real-time fluorescence microscopy [177] demonstrated that multiple aspects of cellular organization depend on a defined distribution of microtubules [178, 179]. This distribution is mediated by, among others, three +TIPs: the EB1 homologue Mal3 [109], the

CLIP170 homologue Tip1 [107] and the kinesin Tea2 [41, 180]. A hierarchy of molecular events required for plus-end tracking has been established from observations inside living yeast cells: the motor Tea2 and its putative cargo Tip1 move along the microtubule lattice towards its growing plus ends, where they accumulate [41, 103]. Efficient recruitment to microtubules and the plus-end accumulation of Tea2 and Tip1 depend on the presence of Mal3, which itself tracks the microtubule plus ends independently of Tea2 and Tip1 [41, 103, 109]. It is not yet known whether additional factors or post-translational modifications are required, or whether Mal3, Tea2 and Tip1 constitute a minimal system that is sufficient to show plus-end tracking. In fact, a mechanistic understanding of plus-end tracking is still missing, in part because of the lack of an *in vitro* assay in which plus-end tracking can be reconstituted with a minimal set of pure components [17].

## 4.1 Results and discussion

Here we reconstitute microtubule plus-end tracking of three fission yeast purified proteins, namely Mal3, Tea2, and Tip1, *in vitro*. The experimental set-up is schematically shown in figure 4.1 a. We observed fluorescently labelled +TIPs and dynamic microtubules by two-color spinning-disc confocal<sup>1</sup> and total internal reflection fluorescence (TIRF)<sup>2</sup> microscopy. Dynamic microtubules were nucleated from short stabilized microtubule seeds attached specifically to a passivated glass surface (see section 4.3).

We first imaged dynamic microtubules in the presence of all three +TIPs: Mal3, Tea2 and green fluorescent protein (GFP)-tagged Tip1 using confocal microscopy. Remarkably, Tip1-GFP was able to accumulate and follow the growing ends of the dynamic microtubules (figure 4.1 b). As Tip1 is at the top of the hierarchy among the three proteins (being the cargo of the kinesin Tea2 and depending on the presence of Mal3 to accumulate at microtubule plus-ends *in vivo*), the three proteins were probably all present at the microtubule tip forming an end-tracking ternary complex. The movie sequence in figure 4.1 b reveals the end-tracking features of Tip1-GFP: i) In the presence of the three +TIPs, Tip1-GFP followed the growing microtubules ends and did not accumulate at the ends of shrinking microtubules or at the static ends of the seeds. ii) Both the plus and the minus ends showed Tip1-GFP accumulation. iii) The intensity of the GFP signal at the microtubule plus end was higher than at the minus end. Also, at the minus end the signal was often blinking during the microtubule elongation, whereas at the plus end the intensity was not visibly fluctuating. The differences in the signal at the two ends indicate that Tip1-GFP in the presence of the three protein complex accumulates preferentially at the microtubule plus-end. The high fluorescence intensity of the tip accumulation indicates the presence of multiple Tip1-GFP molecules following the microtubule end and, most probable, multiple Tea2 and Mal3 molecules.

---

<sup>1</sup>The confocal microscopy of dynamic microtubules and +TIPs was done at AMOLF.

<sup>2</sup>The TIRF microscopy of dynamic microtubules and +TIPs was done at EMBL.

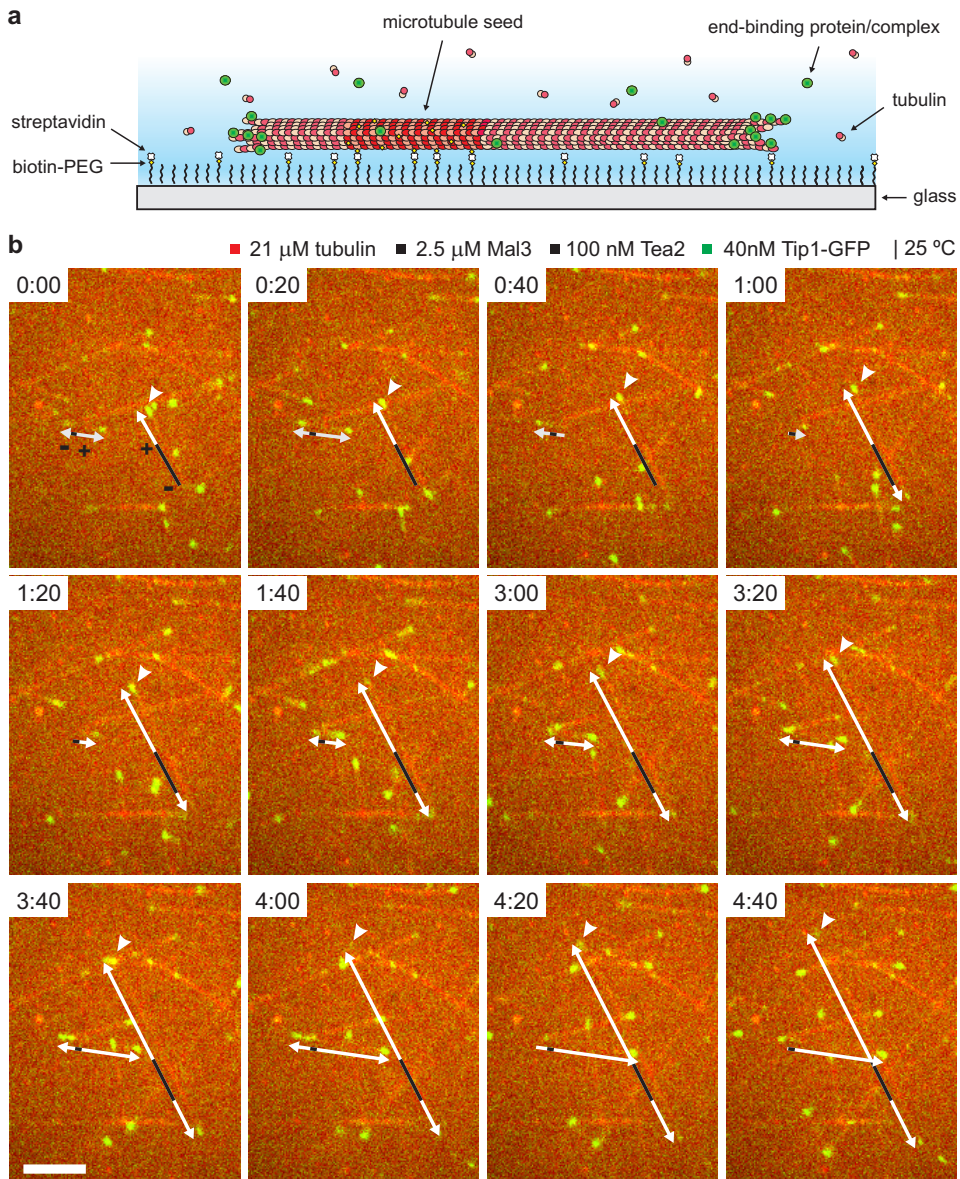


**Figure 4.1: Reconstitution of plus-end tracking *in vitro*.** (a) Diagram of the experimental setup and (b) image sequence showing dynamic microtubules (red) assembled from rhodamine-labelled tubulin in the concomitant presence of Mal3, Tea2 and Tip1-GFP (green). Microtubules were nucleated from surface bound seeds and observed by dual-color spinning-disc confocal microscopy. Schematic guiding lines (shifted with respect to the image) indicate dynamic microtubules (white lines, arrowed if the end is growing) and the corresponding seeds (black lines). Tip1-GFP accumulated and followed only growing microtubule ends, both the plus and the minus end. The intensity of the GFP signal at the plus end (white arrowhead) was higher and less variable during growth as compared with the signal at the minus end. The time elapsed from the first image is indicated in min : sec. Scale bar is 5  $\mu\text{m}$ .

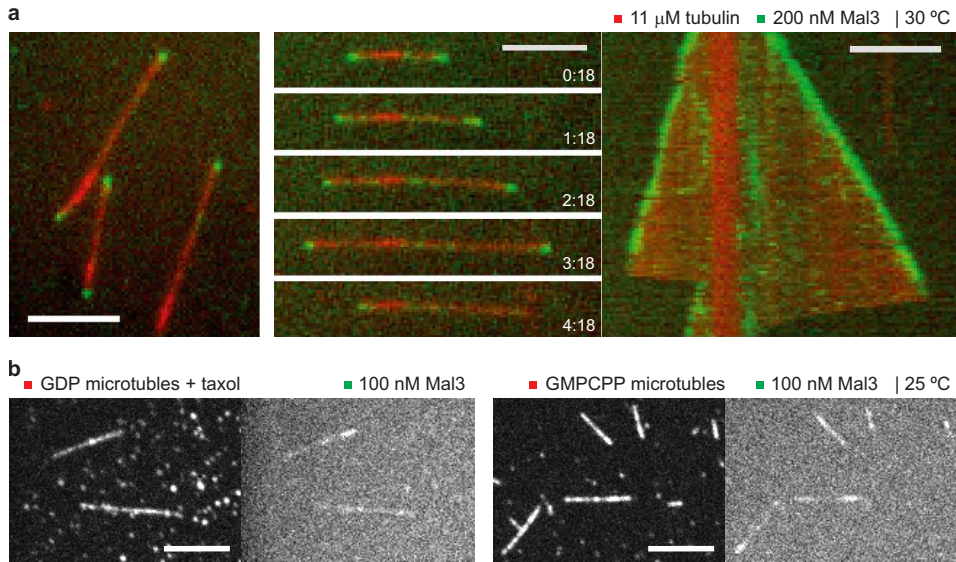


**Figure 4.2: Tracking of growing microtubule ends by Mal3 *in vitro*.** (a) Overlaid TIRF images of Mal3-Alexa 488 (green) and dynamic Alexa 568-labelled microtubules (red). The time sequence of images taken at the indicated times in min : sec (middle) and the corresponding kymograph of the same microtubule (right) shows Mal3 following both growing microtubule ends. Mal3 was used at 200 nM in all end-tracking experiments, unless otherwise stated. The kymograph displays a period of 5 min. Scale bars, 5  $\mu\text{m}$ . (b) Confocal images of static microtubules (left image in each pair) in the presence of 100 nM Mal3-Alexa488 (right image in each pair). Mal3 did not accumulate at the ends of static microtubules neither for the taxol-stabilized GDP microtubules (left pair of images) nor for the microtubules assembled with GMPCPP (equivalent with a GTP-tubulin lattice) (right pair). Scale bars, 5  $\mu\text{m}$ .

This first experiment showed that the minimal complex formed by the three proteins is sufficient to reconstitute *in vitro* the microtubule end-tracking by Tip1-GFP. This specific end-tracking behavior seemed to be insensitive to the exact protein concentrations over a wide range of concentrations (lowest combination: 100 nM Mal3, 20 nM Tea2, 8.5 nM Tip1; highest combination: 2.5  $\mu\text{M}$  Mal3, 100 nM Tea2, 45 nM Tip1). We next studied the three +TIPs individually and then in various combinations with fluorescently labelled and unlabelled +TIPs.

#### 4.1.1 Mal3 recognizes and autonomously tracks microtubule growing ends

Only one of the three proteins, the EB1 homologue Mal3, was able to bind efficiently to dynamic microtubules in the absence of the others. Alexa 488-labelled Mal3 selectively accumulated at growing microtubule ends (figure 4.2 a, left) at considerable ionic strength over a wide range of protein concentrations [124]. A Mal3 signal at microtubule tips could be detected even at Mal3 concentrations as low as 7 nM. (see also sec-

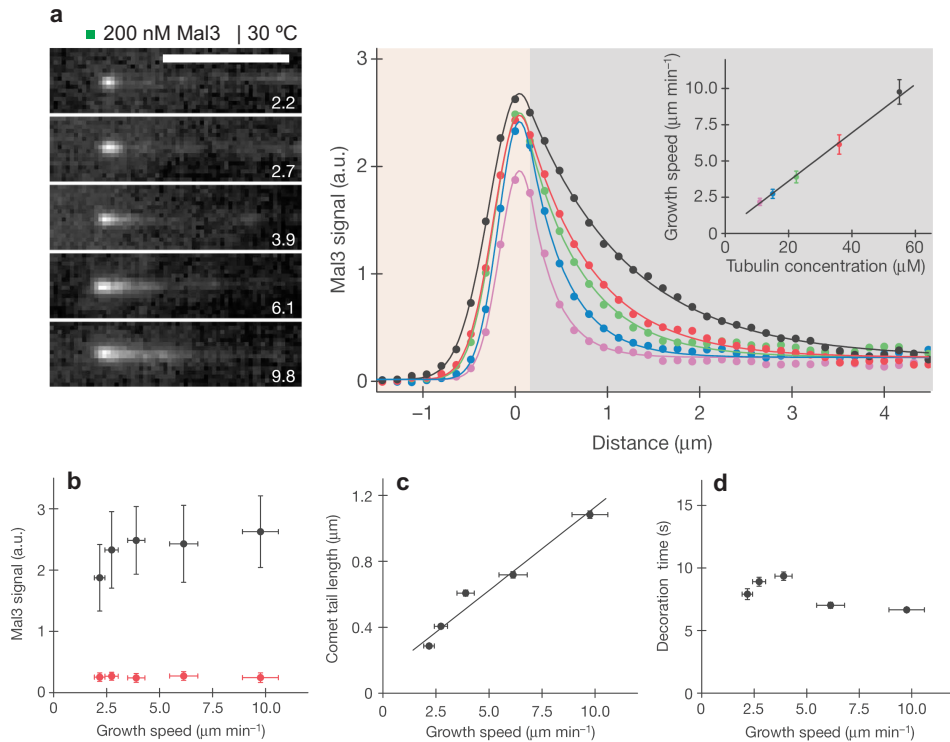


**Figure 4.3: Mechanism of plus-end tracking by Mal3.** (a) Images of individual Mal3-Alexa 488 comets at the indicated growth velocities (in  $\mu\text{m min}^{-1}$ ) (left) and averaged intensity profiles of the comets (right). The Mal3-Alexa 488 concentration was 200 nM. The data (dots) were fitted (lines) using Gaussian (area to the left from the intensity peak) and exponential (area to the right from the intensity peak) functions. The inset shows the dependence of the growth velocities on tubulin concentrations. Error bars indicate s.d. (b) The Mal3-Alexa 488 signal at the peak of the Mal3 comet (black symbols) as obtained from the averaged intensity profiles, and the signal on the microtubule lattice behind the comet (red symbols) as quantified separately from intensity line scans. Error bars indicate the s.d. of the maximum tip intensity and the s.d. of the averaged line scans for the lattice intensity. (c) Mal3 comet tail lengths as obtained from single-exponential fits to the averaged intensity profiles. Error bars indicate standard errors as obtained from the exponential fits. (d) The characteristic decoration time of the Mal3 signal in the Mal3 comet tail at different microtubule growth speeds as obtained by dividing the comet tail length by the microtubule growth speed. Errors were calculated by error propagation.

tion 5.2.2). Movie sequences and the corresponding kymographs (time-space plots), revealed that Mal3 was tracking both the fast-growing plus ends and the more slowly growing minus ends (figure 4.2 a, middle and right). However, Mal3 did not accumulate at the ends of depolymerizing microtubules (figure 4.2 a, middle and right) or static microtubules (figure 4.2 b). Selective tracking of free, polymerizing microtubule ends is therefore an inherent property of Mal3. Mal3-Alexa 488 also bound weakly along

the entire length of microtubules (figure 4.2 a), a behaviour that was enhanced at lower ionic strength (figure 4.2 b). This binding might reflect the previously shown preferential association of Mal3 with the lattice seam of taxol-stabilized microtubules [25].

Two fundamentally different molecular mechanisms can be envisaged for how Mal3 accumulates at the growing microtubule end. Mal3 could co-polymerize in a complex with tubulin to the growing microtubule end, and subsequently be released. Alternatively, instead of binding to free tubulin, Mal3 could recognize a characteristic structural feature at the microtubule end. This structural feature could either be a collective property of several tubulin subunits such as the previously observed protofilament sheet [34] or a property of individual tubulin dimers that are in a GTP-bound versus a GDP-bound state [99].

We investigated the binding of Mal3 on static microtubules that mimic either GTP-bound or GDP-bound tubulin lattice. The microtubules assembled in the presence of GTP and stabilized by taxol will have predominantly GDP-tubulin within the lattice, whereas the microtubules assembled in the presence of GMPCPP, a slowly hydrolyzable analogue of GTP, are equivalent with a microtubule composed of GTP-tubulin subunits. Mal3 had similar affinity for both type of microtubules (figure 4.2 b), indicating that Mal3 most probably does not recognize the growing microtubule end by preferential binding to GTP-tubulin, which is prevalent at the growing tips.

To distinguish between a co-polymerization mechanism and an end-recognition mechanism, we measured the spatial distribution of Mal3 along microtubule plus ends that were growing in the presence of various tubulin concentrations but a constant Mal3 concentration.

Increased microtubule growth velocities resulting from increased tubulin concentrations led to a more comet-shaped accumulation of Mal3-Alexa 488 at growing microtubule plus ends (figure 4.3 a). Averaged fluorescence intensity profiles of Mal3-Alexa 488 comets demonstrated that after an initial peak in fluorescence the signal decreased exponentially towards the basal lattice signal (figure 4.3 a). The peak fluorescence of Mal3 was largely insensitive to changes in the tubulin/Mal3 ratio (figure 4.3 b). This argues against a simple co-polymerization mechanism, because such a mechanism would lead to peak signals that varied with the tubulin/Mal3 ratio. Furthermore, gel-filtration experiments showed that Mal3 does not bind to unpolymerized tubulin [124]. This agrees with the observation that the amount of Mal3 binding along the microtubule lattice is also independent of the tubulin concentration (figure 4.3 b). Together these data support a mechanism in which Mal3 tracks microtubule ends by recognizing a structural feature.

The characteristic comet tail length obtained from exponential fits to the decays of the averaged Mal3 fluorescence intensity profiles increased linearly with the microtubule growth velocity (figure 4.3 c). This suggests that microtubule ends are decorated with Mal3 for a characteristic time of about 8 s, independently of microtubule growth velocity (figure 4.3 d). In contrast, the dwell time of individual Mal3-Alexa 488 mole-



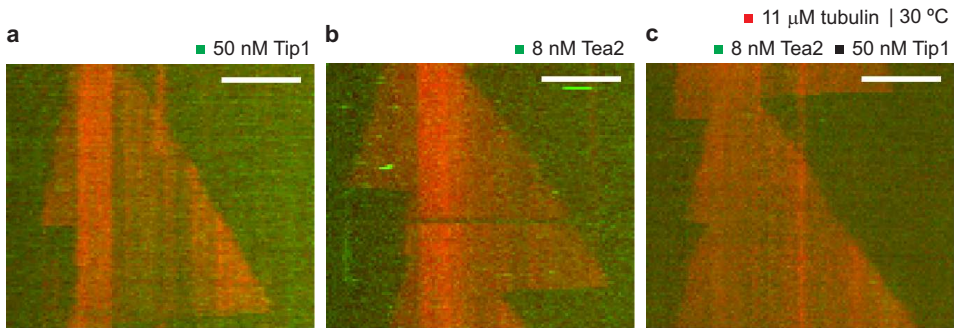


**Figure 4.4: Tea2 and Tip1 individually and in combination do not track microtubule ends at physiological conditions.** Kymographs of (a) Tip1-GFP, (b) Tea2-Alexa 488, and (c) Tea2-Alexa 488 together with Tip1 (labelled +TIPs in green) on dynamic Alexa 568-labelled microtubules (red). The sensitivity for GFP and Alexa 488 detection was strongly increased in comparison with that in figure 4.2 a. Concentrations were 50 nM for Tip1 and 8 nM for Tea2 in all end-tracking experiments unless otherwise stated. The kymographs display a period of 5 min. Scale bars, 5  $\mu\text{m}$ .

cules at growing microtubule plus ends, measured with greater temporal resolution under single-molecule imaging conditions, was only  $0.282 \pm 0.003$  s [124]. This indicates that individual Mal3 molecules turn over rapidly on a plus-end-specific structure that has a lifetime of about 8 s before it transforms into a normal microtubule lattice structure. A similarly fast turnover of Mal3 was also observed *in vivo* [103].

#### 4.1.2 Tea2 and Tip1 need each other and Mal3 for efficient plus-end tracking

In contrast to Mal3, Tip1-GFP and Alexa 488-labelled Tea2 did not bind significantly to the microtubules in conditions under which selective end tracking of Mal3 was observed (figure 4.4 a and b). Under single-molecule imaging conditions, however, rare interactions of the kinesin Tea2 (0.5 nM) with the microtubule could be observed at low ionic strengths with the use of higher frame rates [124]. The analysis of the motion of single Tea2 motors yielded a mean velocity of  $4.8 \pm 0.3$   $\mu\text{m min}^{-1}$  and an average run length of  $0.73 \pm 0.01$   $\mu\text{m}$  [124]. At the same low ionic strength, but at higher concentration, Tea2 (50 nM) bound efficiently to microtubules (figure 4.5 a and b). A Tea2 profile with continuous increase towards the plus-end and a higher accumulation at the tip was observed on static microtubules. The end accumulation could be due to the motors that land close to the microtubule tip (at a distance from the tip smaller than the average run length) leading to the motors dwelling for a while at the tip before releasing from the microtubule. Intensity profiles along microtubules revealed that more Tea2 motors were present on the taxol-stabilized GDP microtubules (figure 4.5 a) than on the GMPCPP microtubules (figure 4.5 b). It is possible that Tea2 has higher affinity

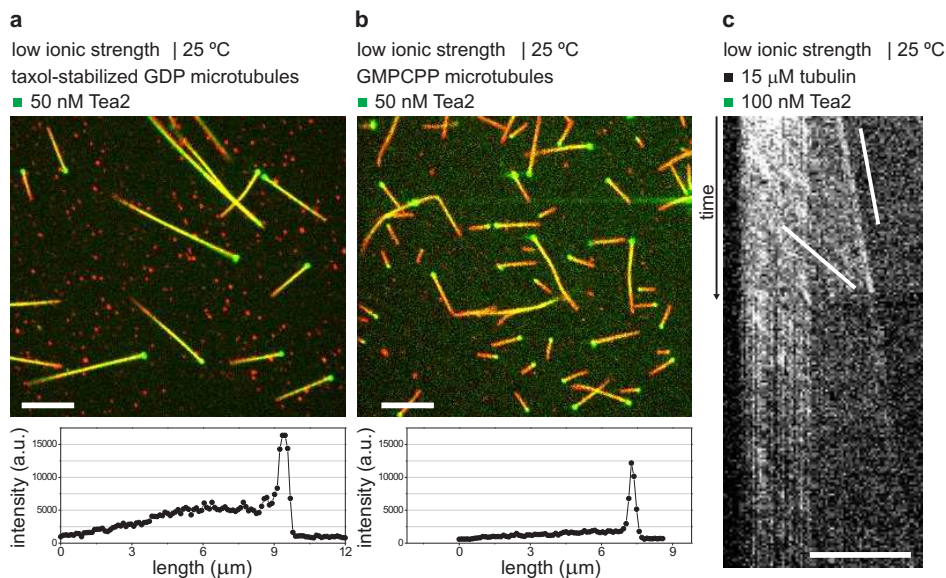


**Figure 4.5: Tea2 binds, walks on and end-tracks growing microtubules at low salt conditions.** (a) and (b) Overlaid spinning-disc confocal images of stabilized microtubules (red) and Tea2-Alexa 488 (green). At low salt conditions and in the absence of free tubulin Tea2-Alexa 488 binds efficiently and walks on static microtubules. The kinesin accumulates at the microtubule plus ends. The line intensity profiles along one microtubule shows that more Tea2 was present on (a) taxol-stabilized GDP microtubules than on (b) the GMPCPP microtubules. (c) Kymograph of Tea2-Alexa 488 tracking the plus-end of a dynamic microtubule (same low salt condition as in (a) and (b)). On the microtubule lattice Tea2-Alexa 488 motors moved towards the plus end with a speed higher than the microtubule growth speed. Two lines are drawn as guidance to the eye: one indicating microtubule growth and one indicating Tea2 speckle movement along the microtubule lattice. The kymograph displays a period of 400 sec. Scale bars, 5  $\mu\text{m}$ .

for the GDP-tubulin lattice and/or the run length of the motor is increased on the GDP-microtubules. Both the single molecule experiments and the binding on the static microtubules were performed in the absence of free tubulin. When we imaged Tea2-Alexa 488 on dynamic microtubules (where free tubulin is present), at low ionic strength conditions, surprisingly, we observed Tea2 tracking the growing plus-ends. The efficiency of binding to the microtubules was though much lower than in the absence of free tubulin. The mechanism of tracking dynamic ends could be understood in a similar way with the accumulation at the microtubule static ends, as the Tea2 kinesin walks faster than the microtubules grow. Using kymograph analysis of the Tea2 motion on dynamic microtubules we measured an average motor speed of  $3.5 \pm 0.8 \mu\text{m min}^{-1}$ , which was 6-fold higher than the microtubule growth speed  $0.6 \pm 0.1 \mu\text{m min}^{-1}$ . We cannot completely exclude the possibility of Tea2 accumulation at the end due to an unnatural aggregation induced by the low ionic strength. Though, if aggregation of the motor

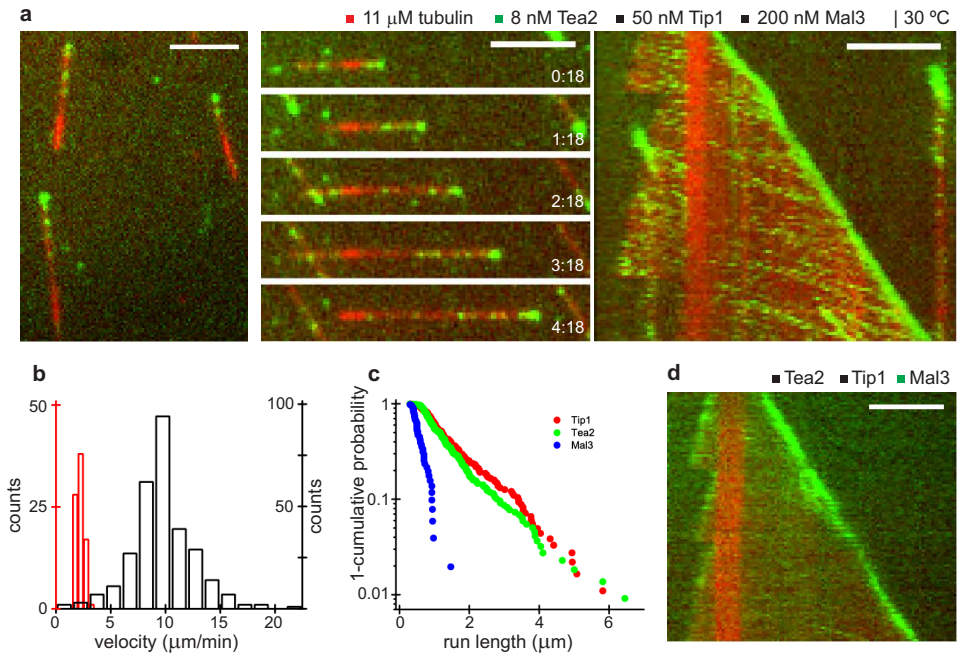


**Figure 4.6: Efficient microtubule plus-end tracking of Tea2-Tip1 in the presence of Mal3.** (a) Overlaid TIRF images showing Tea2-Alexa 488 (green) and Alexa 568-labelled microtubules (red) in the presence of the two other +TIPs (left). Middle, time sequence of images (at the times shown, in min : sec); right, the corresponding kymograph. Protein concentrations for Mal3 are as in figure 4.2 and for Tea2 and Tip1 as in figure 4.4. Kymographs display periods of 5 min. Scale bars, 5  $\mu\text{m}$ . (b) Histograms of the velocities of microtubule plus-end growth (red, left axis) and Tea2-Alexa 488 speckle movement along the microtubule lattice (black, right axis). The increased velocity of Tea2 speckles in comparison with single Tea2 molecules is mostly a consequence of an increased temperature. (c) Run-length distribution of Mal3-Alexa 488 (green), Tip1-GFP (black) and Tea2-Alexa 647 (blue) moving along the microtubule lattice, always in the presence of the other two +TIPs. Concentrations were 100 nM Mal3, 50 nM Tip1 and 8 nM Tea2. (d) Kymograph showing Mal3-Alexa 488 (green) in the presence of Tea2 and Tip1. The signal intensity can be directly compared with figure 4.2 a.

would predominate, artifacts would appear also on the lattice of static microtubules as local accumulations, which we do not observe in our sample. This experiment suggests that microtubule plus-end tracking is an intrinsic ability of Tea2, but at higher ionic strengths (physiological conditions) Tea2 is not able to efficiently follow growing plus-ends on its own. The preference of Tea2 for the GDP lattice (observed in the absence of free tubulin) could entail that the main role of Tea2 is to assure the efficient transport of other +TIPs to the microtubule tip where these hitchhikers could accumulate and exert a specific function.

Because Tea2 binds *in vivo* [109] and *in vitro* [124] to Tip1, and because the motor might be auto-inhibited without its putative cargo, we tested whether Tip1 could en-

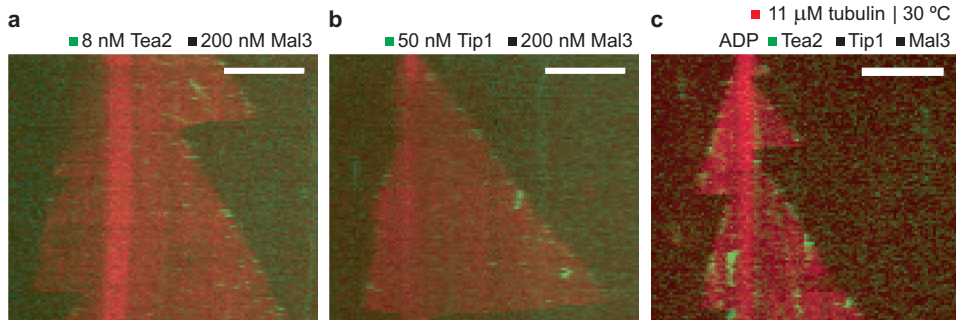


**Figure 4.7: All three +TIPs and the motor activity of Tea2 are required for microtubule plus-end tracking of the Tea2-Tip1 complex.** (a) Tea2-Alexa 488 (green) in the presence of Mal3 alone does not bind efficiently to microtubules (red). The fluorescence signal can be directly compared with figure 4.4 middle. (b) Tip1-GFP (green) in the presence of Mal3 alone does not bind efficiently to microtubules (red). The fluorescence signal can be directly compared with figure 4.4 left. (c) The motor activity of Tea2 is required for its microtubule plus-end tracking ability: Tea2-Alexa 488 (green) in the presence of Mal3, Tip1 and ADP instead of ATP. The signal intensity can be directly compared with figure 4.6 a. Standard concentrations of 200 nM Mal3, 50 nM Tip1 and 8 nM Tea2 were used. Kymographs display periods of 5 min. Scale bars, 5  $\mu\text{m}$ .

hance the binding of Tea2-Alexa 488 to dynamic microtubules. However, this was not the case (figure 4.4 c).

*In vivo*, the presence of Mal3 is needed for the plus-end tracking of Tea2 and Tip1 [41, 103, 109]. Triggered by this observation together with our first successful *in vitro* reconstitution of the end-tracking by the three protein complex we examined whether the autonomous plus-end tracking protein Mal3 is sufficient to mediate microtubule plus-end tracking of Tea2 and Tip1 alone. We investigated in further detail the localization and the end-tracking behavior of the individual +TIPs when all three proteins were present.

At high ionic strengths, in the presence of Mal3 and Tip1, Tea2-Alexa 488 strongly accumulated at growing microtubule plus ends (figure 4.6 a). No accumulation of Tea2-Alexa 488 was visible at growing minus ends (figure 4.6 a) or depolymerizing ends at this condition. Furthermore, Tea2-Alexa 488 speckles appeared along the microtubule lattice and moved towards the plus end (figure 4.6 a, right). The speed of these particles was on average  $9.8 \pm 2.9 \mu\text{m min}^{-1}$  and therefore 4.4-fold faster than the velocity of microtubule growth ( $2.2 \pm 0.3 \mu\text{m min}^{-1}$ ; figure 4.6 b). Tip1-GFP moved similarly along the microtubule lattice and also tracked growing microtubule plus ends, but not depolymerizing ends or the ends of static microtubules [124]. Some accumulation at the growing minus ends was though observed at increased concentrations of proteins (see figure 4.1). Mal3-Alexa 488, in contrast, was not observed to move along the microtubule to the same extent as Tea2 and Tip1 (figure 4.6 d). These observations very closely mimic the situation *in vivo* [41, 103, 109].

In addition, Mal3-mediated recruitment of the Tea2-Tip1 complex requires the presence of both Tea2 and Tip1. Tea2-Alexa 488 was hardly present on the microtubules in the absence of Tip1 (figure 4.7 a) and Tip1-GFP was not significantly bound to microtubules in the absence of Tea2 (figure 4.7 b), whereas binding of Mal3-Alexa 488 to microtubules was unaffected in both cases. The results with the double combinations of proteins (figure 4.4 c and figure 4.7 a and b) exactly mimic the *in vivo* single-deletion mutants of Mal3, Tea2 and Tip1 [41, 103, 109].

#### 4.1.3 Mal3 acts as a loading factor for the Tea2-Tip1 complex

Gel filtrations demonstrated that in solution Mal3, Tea2 and Tip1 exist as a stable ternary complex [124]. It is therefore most likely that the formation of this complex is required for efficient binding of Tea2-Tip1 to the microtubule. However, the three proteins do not behave in the same way once bound to the microtubule. Imaging the movements of the three proteins on the microtubule lattice with greater temporal resolution showed that Tip1-GFP and Alexa 647-labelled Tea2 co-migrate [124], indicating that Tea2 indeed transports Tip1. Consistent with this was the observation that the average run lengths for Tea2 and Tip1 were very similar, at  $0.90 \pm 0.01$  and  $1.10 \pm 0.01$   $\mu\text{m}$ , respectively (figure 4.6 c). In contrast, Mal3-Alexa 488 showed only short runs with an average run length of  $0.29 \pm 0.01$   $\mu\text{m}$  (figure 4.6 c). This demonstrates that Mal3 is initially transported by Tea2, but dissociates shortly after a productive binding event.

We confirmed that Mal3-mediated recruitment of Tea2-Tip1 to the microtubule lattice requires the interaction of Mal3 with the amino-terminal extension of the kinesin Tea2 [181]. Replacing full-length Tea2 with a construct lacking the N-terminal extension ( $\Delta\text{NTea2}$ ) abolished efficient binding of Tip1-GFP to the microtubule [124].

Replacing ATP with ADP eliminated the efficient binding of Tea2-Alexa 488 along the microtubule lattice and the tracking of microtubule plus ends, despite the presence of all three proteins (figure 4.7 c). Only a very weak fluorescence signal could be observed at growing microtubule ends, but without a preference for the plus or minus end (figure 4.7 c). This demonstrates that *in vitro* the processive motor activity of Tea2 is essential for efficient microtubule-end tracking of Tea2-Tip1 and also for their plus-end preference.

#### 4.1.4 Microtubule dynamics in the presence of Mal3, Tea2 and Tip1

In living cells, single deletions of Mal3, Tea2 or Tip1 suggested that these three +TIPs mainly decrease the frequency of microtubule catastrophes without strongly affecting the other parameters of microtubule dynamic instability [107, 109, 180]. We tested the direct effect of Mal3 alone and of Mal3 with Tea2 and Tip1 on microtubule dynamics under conditions of selective end tracking. We imaged microtubules in the presence of unlabelled +TIPs by differential interference contrast microscopy. At the conditions selected for the end-tracking experiments, neither Mal3 alone nor the combination of

Mal3	Tea2	Tip1	$v_{gro}$ ( $\mu\text{m}/\text{min}$ ) (n)	$v_{shr}$ ( $\mu\text{m}/\text{min}$ ) (n)	$T_{cat}$ (s) ( $N_{cat}$ )	$N_{res}$ in total time of shrinkage
-	-	-	$1.2 \pm 0.2$ (62)	$26 \pm 9$ (41)	$650 \pm 80$ (69)	0 in 322 s
+	-	-	$1.3 \pm 0.2$ (63)	$26 \pm 8$ (74)	$230 \pm 20$ (132)	8 in 314 s
+	+	+	$1.3 \pm 0.2$ (54)	$27 \pm 9$ (40)	$410 \pm 50$ (61)	4 in 321 s

**Table 4.1: Dynamic instability parameters of microtubules in the absence and presence of +TIPs.** Dynamic instability parameters under conditions of selective end-tracking (200 nM Mal3, 50 nM Tip1 and 8 nM Tea2). The mean growth velocity ( $v_{gro}$ ) and mean shrinkage velocity ( $v_{shr}$ ) represent the weighted averages (weights are the time spanned by each event) over a total of  $n$  events. The error on the mean is the weighted standard deviation (s.d.). The average time until a catastrophe occurred ( $T_{cat}$ ) is the total growth time (summed over individual events) divided by the number of catastrophes observed ( $N_{cat}$ ). The error on  $T_{cat}$  is the standard deviation (s.d.) calculated as  $T_{cat}/\sqrt{N_{cat}}$ . The number of rescues ( $N_{res}$ ) in total shrinkage time is given. The time until a rescue occurred and its statistical error could not be determined due to the limited number of events observed.

all three proteins had a strong effect on the growth and shrinkage velocities of microtubule plus ends (table 4.1). However, Mal3 alone increased the frequencies of catastrophes and rescues (table 4.1). In chapter 5 the effect of Mal3 was investigated in more detail revealing that Mal3 has a complex influence on microtubule dynamics, affecting all dynamic instability parameters. The addition of Tea2-Tip1 counteracted the observed effects of Mal3 (table 4.1). Preliminary experiments on the mechanism of regulation of microtubule dynamics by the combination of all three +TIPs are presented in chapter 7 (section 7.2.1). Our results discussed above show that especially the effect of Mal3 on the catastrophe frequency is different from what would be expected from the corresponding deletion *in vivo*. This is not surprising, because several other proteins not studied here are known to affect the catastrophe frequency [182, 183]. By including these other modulators of microtubule dynamics in the future, our *in vitro* system promises also to lead to the identification of the more complex minimal system that reproduces physiological microtubule dynamics.

## 4.2 Conclusions

Thus, we have identified Mal3 as an autonomous tracking protein of growing microtubule ends *in vitro*. Mal3 most probably recognizes a structural feature at microtubule ends rather than co-polymerizes as a tubulin-Mal3 complex. As *in vivo*, the behavior of Mal3 *in vitro* does not depend significantly on the presence of Tea2 or Tip1. Furthermore, we identified Mal3-Tea2-Tip1 as a minimal system producing plus-end tracking behavior of Tea2 and Tip1 *in vitro*. This suggests that *in vivo* Tea2, Tip1 and Mal3 may also work as a microtubule plus-end tracking system, independently of other +TIPs. However, *in vivo* part of the Mal3 pool might simultaneously function in 'parallel' end-

tracking systems. The role of Mal3 as a loading factor of Tea2-Tip1 involves the initial formation of a ternary complex that promotes productive encounters of Tea2-Tip1 with the microtubule lattice. Tip1 is subsequently transported by the processive motor Tea2, whereas Mal3 rapidly dissociates and is transported for only short distances.

Our in vitro system provides a powerful new tool to test the proposed mechanisms for microtubule end targeting of different +TIPs [17, 29, 110] and to analyse the interplay between plus-end tracking and the dynamic properties of microtubules that are ultimately responsible for the morphogenetic function of the microtubule cytoskeleton.

## 4.3 Methods

### 4.3.1 End-tracking assay using TIRF microscopy<sup>3</sup>

**Experimental method.** Flow chambers consisting of a biotin-PEG-functionalized coverslip (as described in [184]) and a PLL-PEG passivated glass were assembled. To block the residual nonspecific binding sites on the surface, the flow chamber was incubated with 1% Pluronic F-127 and 50  $\mu\text{g/ml}$   $\kappa$ -casein in assay buffer on ice. Brightly labelled, short GMPCPP microtubules (containing 20% Alexa 568-labelled tubulin and 7.7% biotinylated tubulin) were attached by means of neutravidin to the biotin-PEG functionalized coverslip. With the use of a custom TIRF microscopy system [124], dynamic microtubules and +TIPs either tagged with GFP or labelled with Alexa fluorophores were observed in the presence of 11  $\mu\text{M}$  dimly labelled tubulin (containing 6.7% Alexa 568-labelled tubulin) in assay buffer (80 mM K-PIPES pH 6.8, 85 mM KCl, 4 mM  $\text{MgCl}_2$ , 1 mM GTP, 1 mM EGTA, 10 mM 2-mercaptoethanol and 2 mM MgATP or 5 mM MgADP) containing 0.1% methylcellulose (4,000 cP; Sigma) and an oxygen scavenger system (20 mM glucose, 200  $\mu\text{g/ml}$  glucose-oxidase, 400  $\mu\text{g/ml}$  catalase). In some experiments with Mal3, the tubulin concentration was varied in order to vary the microtubule growth rate (figure 4.3). Unless stated otherwise, the final concentrations of the labelled and unlabelled +TIP proteins were kept constant at 200 nM Mal3, 50 nM Tip1 and 8 nM Tea2. These protein concentrations were chosen after systematic variation of concentrations to allow the easy visualization of both end tracking and transport along microtubules. The temperature was  $30 \pm 1^\circ\text{C}$ . The experimental conditions for other measurements mentioned here (determination of individual run length and speed of +TIPs on the microtubules, the speed of single Tea2 molecules on static microtubules, and the dwell time of single Mal3 molecules at the microtubule plus-end) are given in [124]. The +TIP proteins were expressed, purified and labelled as described in [124].

**Data analysis.** The growth trajectories of microtubules and walking tracks of Tea2-Tip1 speckles were analyzed with kymographs in ImageJ (plug-in developed by Arne

<sup>3</sup>The TIRF experimental set-up is located at EMBL.

Seitz). Single-molecule motility was analyzed with kymographs and by automated particle tracking implemented in a custom software environment [124].

Average run lengths of Tea2, Tip1 and Mal3 speckles and their standard error (figure 4.6 c) were obtained from exponential fits to '1-cumulative probability' distributions of the individual travel distances as determined by kymograph analysis from two independent experiments for each protein. The total number of events analyzed was  $n = 198$  for Mal3-Alexa 488,  $n = 520$  for Tea2-Alexa 647, and  $n = 182$  for Tip1-GFP.

To analyze the shape of Mal3 comets (figure 4.3), line profiles of the fluorescence intensity of Mal3-Alexa 488 at growing microtubule plus ends were aligned and averaged. An exponential fit to the tail of the profile was then used to quantify the decay of the signal. Detailed analysis methods are described in [124].

### 4.3.2 End-tracking assay using confocal microscopy<sup>4</sup>

**Experimental method.** Flow chambers were assembled between a pre-cleaned glass coverslip and a microscopy slide. The chamber was incubated with 0.2 mg/ml PLL-PEG-biotin (Susos AG, Switzerland) in assay buffer or 2.5 mg/ml biotin-BSA in acetate buffer (21 mM acetic acid, 79 mM  $C_2H_3O_2Na$ , pH 5.2) and after rinsing, with 1 mg/ml streptavidin in assay buffer. Short GMPCPP microtubules (containing 17% biotin-tubulin and 7% rhodamine-tubulin) were specifically attached to the functionalized surface by biotin-streptavidin links. The flow chamber was passivated by incubation with 1 mg/ml  $\kappa$ -casein. Dynamic microtubules were assembled in the presence of 21  $\mu M$  tubulin (containing 5% rhodamine-labelled tubulin) and +TIPs in assay buffer (80 mM K-PIPES pH 6.8, 55 mM KCl, 4 mM  $MgCl_2$ , 1 mM EGTA) supplemented with 1 mM GTP, 0.2 mg/ml  $\kappa$ -casein, 0.2 mg/ml  $\alpha$ -casein, and an oxygen scavenger system (50 mM glucose, 400  $\mu g/ml$  glucose-oxidase, 200  $\mu g/ml$  catalase, 4 mM DTT). When Tea2 was present in solution, additional 1 mM ATP was added. The final concentrations of +TIPs for the experiment presented in figure 4.1 were 2.5  $\mu M$  Mal3, 100 nM Tea2 and 40 nM Tip1-GFP. In the experiment with only Tea2 on dynamic microtubules (figure 4.5 c), the ionic strength of the assay buffer was lowered (12 mM K-PIPES pH 6.8, 4 mM  $MgCl_2$ , 1 mM EGTA), the tubulin concentration was 15  $\mu M$  and the solution contained 100 nM Tea2. Labelled and unlabelled tubulin was purchased from Cytoskeleton. The sample was sealed with candle wax. During experiments the sample was kept at constant temperature of  $25 \pm 1^\circ C$ .

**Confocal microscopy.** Fluorescently labelled +TIPs and dynamic microtubules were imaged with a confocal spinning disc microscope, comprising a confocal scanner unit (CSU22, Yokogawa Electric Corp) attached to an inverted microscope (DMIRB, Leica) equipped with a 100x/1.3 NA oil immersion lens (PL FLUOTAR, Leica) and a built-in 1.5x magnification lens. The sample was illuminated using a 488 nm laser (Sapphire 488-30 CHRH, Coherent Inc.) or a 561 nm laser (85-YCA-015, Melles Griot). Images

---

<sup>4</sup>The spinning-disc confocal set-up is located at AMOLF.



were captured by a cooled EM-CCD camera (C9100, Hamamatsu Photonics) controlled by software from VisiTech International. Images were acquired with a typical 500 ms exposure time. Laser intensity was varied depending on the labelled protein concentration. The temperature was controlled by maintaining the room at  $25 \pm 1^\circ\text{C}$ .

**Data analysis.** The growth trajectories of microtubules and walking tracks of Tea2 speckles were analyzed from kymographs in ImageJ (plug-in developed by Arne Seitz). Weighted averages and weighted standard deviation (see section 4.3.4) were calculated for the microtubule growth speed ( $n=13$ ) and the speed of Tea2 speckles ( $n=65$ ) on microtubules from one experiment with Tea2 alone on dynamic microtubules.

### 4.3.3 +TIPs on static microtubules analyzed by confocal microscopy

The samples were prepared in a similar way as for the end-tracking assay. The stabilized microtubules were specifically bound to the biotin-PEG functionalized glass surface by biotin-streptavidin links. The GMPCPP microtubules were prepared by incubation of  $30 \mu\text{M}$  tubulin (containing 17% biotin-tubulin and 2% rhodamine-tubulin) with 1 mM GMPCPP (Jena Bioscience, Germany) at  $36^\circ\text{C}$  for 50 minutes. The GTP microtubules were prepared from  $50 \mu\text{M}$  tubulin (containing 17% biotin-tubulin and 2% rhodamine-tubulin) and 1 mM GTP by incubation at  $36^\circ\text{C}$  for 50 minutes and additional 10 minutes after 10-fold dilution with  $10 \mu\text{M}$  taxol (Cytoskeleton) warm solution. Mal3 at a concentration of 100 nM was introduced in assay buffer as described for the end-tracking assay. Tea2 was used at a concentration of 50 nM in low ionic strength assay buffer (12 mM K-PIPES pH 6.8, 4 mM  $\text{MgCl}_2$ , 1 mM EGTA) supplemented with 1 mM ATP, 0.3 mg/ml  $\kappa$ -casein, 0.3 mg/ml  $\alpha$ -casein, and an oxygen scavenger system. The solutions did not contained free tubulin or GTP. In the experiments with taxol stabilized microtubules  $10 \mu\text{M}$  taxol was maintained in the protein mix. Temperature was  $25 \pm 1^\circ\text{C}$ . Samples were imaged with the same confocal spinning disc microscope as above. Line intensity profiles along microtubules were measured in ImageJ.

### 4.3.4 DIC assay to measure microtubule dynamics

**Experimental method.** Samples were prepared in a similar way as for the TIRF end-tracking assay. The functionalized surface was created with 0.2 mg/ml PLL-PEG-biotin and 1 mg/ml streptavidin and passivation was done with 0.5 mg/ml  $\kappa$ -casein. The nucleating seeds contained 15% biotin-labelled tubulin only. Protein concentrations were as for the TIRF end-tracking assay. Samples were maintained at  $30 \pm 1^\circ\text{C}$ .

**DIC microscopy.** Dynamic microtubules nucleated from surface bound seeds were imaged by video-enhanced differential interference contrast (VE-DIC) microscopy using an inverted microscope (DMIRB, Leica) equipped with a 100x/1.3 NA oil immersion objective (HCX PL FLUOTAR, Leica). The temperature in the sample was adjusted and maintained constant by Peltier elements (Melcor) mounted on a sleeve around the objective and controlled by in-house built electronics. Images were acquired with a CCD

camera (CF8/1, Kappa), further processed for background subtraction and contrast enhancement with an image processor (C5510 Argus 20, Hamamatsu Photonics) and digitized on-line at a rate of 1 frame per 2 seconds with an in-house developed software (written and run in IDL). Simultaneously with the on-line digitization, the processed images were recorded on a DVD at video rate with a commercial burner (DVD R-80, Philips).

**Data analysis.** For the analysis of microtubule dynamics, for every condition DIC data was collected from three independent experiments and for every experiment a minimum of 10 microtubules were analyzed with kymographs. The average growth and shrinkage speeds (table 4.1) were calculated as weighted averages over all events as  $v = (\sum_1^n v_i t_i) / (\sum_1^n t_i)$ . Individual speeds ( $v_i$ ) were estimated from manual fits to the growth or shrinkage parts of the kymograph. The weights are represented by the times ( $t_i$ ) spanned by the individual events ( $i$ ). The error was calculated as weighted standard deviation, derived from  $sd^2 = \frac{n}{n-1} (\sum_1^n (v_i - v)^2 t_i) / (\sum_1^n t_i)$ . The catastrophe time ( $T_{cat}$ ) was calculated as the total growth time divided by the number of catastrophes observed ( $N_{cat}$ ) and the statistical error on  $T_{cat}$  as  $T_{cat} / \sqrt{N_{cat}}$ . The number of rescues observed ( $N_{res}$ ) in total shrinkage time are mentioned (table 4.1).

### Acknowledgments

The major part of the experimental work presented in this chapter is published in [124] and was the result of a collaborative effort between AMOLF: Liedewij Laan, myself and Marileen Dogterom and EMBL: Peter Bieling, Henry T. Schek, Linda Sandblad, Thomas Surrey and Damian Brunner.

[124]: Bieling P, Laan L, Schek HT III, Munteanu EL, Sandblad L, Dogterom M, Brunner D, Surrey T (2007) Reconstitution of a microtubule plus-end tracking system *in vitro*. *Nature* **450**: 1100-1105

---

## Regulation of microtubule dynamics by the autonomous microtubule-end tracker Mal3

*+TIPs are intriguing proteins that have the special ability to localize at the microtubule growing ends. This advantageous position enables +TIPs to directly regulate the microtubule dynamics. EB1 protein family members were shown to affect microtubule dynamics and organization in vivo, but it is still unclear if the EB proteins exert an effect on microtubule dynamics on their own. In this chapter we investigated the effect of such a +TIP from the EB1 protein family, namely the fission yeast homologue, Mal3. Our results show that, in vitro, Mal3 is an autonomous end tracker of growing microtubule ends. Here we investigate the effect of Mal3 on the microtubule plus-end growth dynamics using light microscopy, fluorescence microscopy and our high-resolution technique based on optical tweezers. Using time-lapse DIC and fluorescence imaging of individual microtubules we find that Mal3 binds differentially to the lattice and at the tip of a growing microtubule and the presence of Mal3 affects all the parameters of microtubule dynamic instability. Mal3 binds efficiently at the microtubule tip where it enhances tubulin dimer net addition and the chance for a microtubule to switch from a growing to a shrinking phase. Microtubules in the presence of Mal3 grew up to 3-fold faster and had up to 4-fold enhanced catastrophe rate. Using our high-resolution technique we could identify incomplete microtubules, most probably resembling the end-structures at the growing tip, that were formed in the presence of Mal3. In the fluorescent measurements we identified longer Mal3-decorated end-structures with increasing Mal3 concentrations. At the microtubule lattice Mal3 binds less potently than at the tip. With Mal3 present at the lattice, the microtubules disassembled slower and rescues were highly promoted. Our results suggest that Mal3 has a complex influence on microtubule dynamics, both stabilizing and destabilizing and that Mal3 induced effects are correlated with a differential binding of Mal3 at the tip and on the lattice of a growing microtubule.*

## 5.1 Introduction

Mal3 is the fission yeast homolog of end-binding 1 (EB1) protein. EB1 family members are highly conserved regulators of microtubule dynamics belonging to the core part of the interaction network formed by the microtubule plus-end binding proteins [14]. Human EB1 added to *Xenopus* egg extracts promotes microtubule growth by increasing the rescue rate and decreasing the catastrophe rate [110, 185]. The fission yeast homologue Mal3 was also shown to promote initiation of microtubule growth and to inhibit catastrophes. Cells that are lacking Mal3 have shortened microtubules with premature catastrophes [108, 109].

In order to dissect the influence of the end-binding proteins on the microtubule dynamics we need an *in vitro* assay, in which the *in vivo* localization of the proteins on dynamic microtubules is preserved and individual microtubules can be monitored in the presence of one protein or a system of end-binding proteins. The growth promoting effect of EB1 and Mal3 on microtubules was previously suggested from bulk turbidity assays [25, 112] that reflect the influence of the proteins on the total polymer formed [170] and do not give information about the influence on the dynamics of individual microtubules. Experiments were also performed on individual microtubules in egg extracts [110] and in cells [109, 113, 114]. In these experiments, the environment in which the microtubules assemble contains a cocktail of proteins and therefore the sole influence of EB1 or Mal3 on microtubule dynamics cannot be inferred.

As described in chapter 4, Mal3 is a microtubule-end tracker *in vitro* with similar end-tracking behavior as *in vivo*. Mal3 is able to accumulate both at the plus and minus ends of growing microtubules and not on the ends of shrinking or stable microtubules. Strikingly, this behavior does not depend on the presence of other end-tracking proteins. Here we investigate the influence of Mal3 on the dynamics of individual microtubules and the molecular mechanism of interaction with the microtubule end. Dynamic microtubules were nucleated from centrosomes in order to selectively probe the plus end dynamics of microtubules.

## 5.2 Results

### 5.2.1 Mal3 enhances the dynamic instability of microtubules *in vitro*.

In the presence of Mal3 we observed a change in all dynamic instability parameters: growth speed, shrinkage speed, catastrophe rate and rescue rate.

For Mal3 concentrations ranging from 20 nM to 200 nM, the growth speed was enhanced in a concentration dependent manner: the more Mal3 present, the faster the microtubules grew (figure 5.1 b). Mal3 sped up the microtubule growth to a maximum of 3-fold achieved at a ratio of Mal3 : tubulin of approximately 1 : 70. For Mal3 concentrations higher than 200 nM, the average growth speed remained constant at the 3-fold enhanced level (figure 5.1 b). The effect of Mal3 on shrinkage speed was less strong.

The presence of the end binding protein slowed down depolymerizing microtubules. For concentrations less than 200 nM Mal3, the effect on the shrinkage speed was concentration dependent (figure 5.1 c). We measured a constant 1.5-fold reduction in the shrinkage speed in the presence of more than 200 nM Mal3.

Microtubules grow and shrink with intrinsically variable speeds [186]. This variability is reflected by the standard deviation, sd, over the speeds of individual growth and shrinkage events. We typically measured sd values of 20% to 30% of the average microtubule growth and shrinkage speeds. We did not observe an influence of Mal3 on the sd, indicating that Mal3 had no effect on the intrinsic variability of microtubule growth and shrinkage.

The most striking effect we measured in the presence of Mal3 was the increased catastrophe rate (figure 5.1 d), as opposed to the *in vivo* case where the absence of Mal3 results in more dynamic microtubules [108, 109]. We observed that the catastrophe rate *in vitro* was increasing with the concentration of Mal3, to a maximum of  $0.20 \pm 0.02 \text{ min}^{-1}$ , which is 4-fold higher than the catastrophe rate we measured in control samples (no Mal3:  $0.050 \pm 0.006 \text{ min}^{-1}$ ). This maximum was reached around 100 nM Mal3 corresponding to a Mal3 : tubulin ratio of 1 : 150. For Mal3 concentrations higher than 100 nM, the catastrophe rate was slowly decreasing to  $0.14 \pm 0.02 \text{ min}^{-1}$ , which was still 3-fold higher than the control level.

Mal3 had a strong concentration dependent effect on the rescue frequency as well (figure 5.1 e). We measured a more than 10-fold increase in the rescue rate in the range from 100 nM to 2.5  $\mu\text{M}$  Mal3. The increase was approximately linear with the Mal3 concentration and the rescue rate did not saturate in the range of concentrations we investigated. For Mal3 concentrations below 200 nM we were not able to calculate a reliable rescue frequency due to the low number of events observed and only an upper bound could be estimated (data analysis described in section 5.5.1).

The addition of new tubulin subunits, reflected in the growth speed, as well as the initiation of a shrinkage phase, reflected in the catastrophe rate, happens at the microtubule tip. We saw a similar influence of Mal3 on the two processes: at low Mal3 concentrations, the Mal3-induced enhancement was proportional with the amount of Mal3 present in solution and above a certain concentration, the effect saturated. The rapid disassembly of tubulin, evaluated as shrinkage speed, and the chance of switching from a shrinkage to a growing phase, the rescue rate, depend mostly on the microtubule lattice properties. We observed a different behavior for the rescue rate as compared with the catastrophe rate: we measured a continuously increasing rescue rate proportional to the Mal3 concentration and no saturation of this effect. Shrinkage speed had yet similar behavior as the growth speed and catastrophe rate. These differences between the effects of Mal3 on the dynamic instability parameters might reflect a differential interaction of Mal3 with the tip and with the microtubule lattice. Therefore we next investigated the localization of Mal3 on the dynamic microtubules at similar conditions used to determine the dynamic instability parameters.

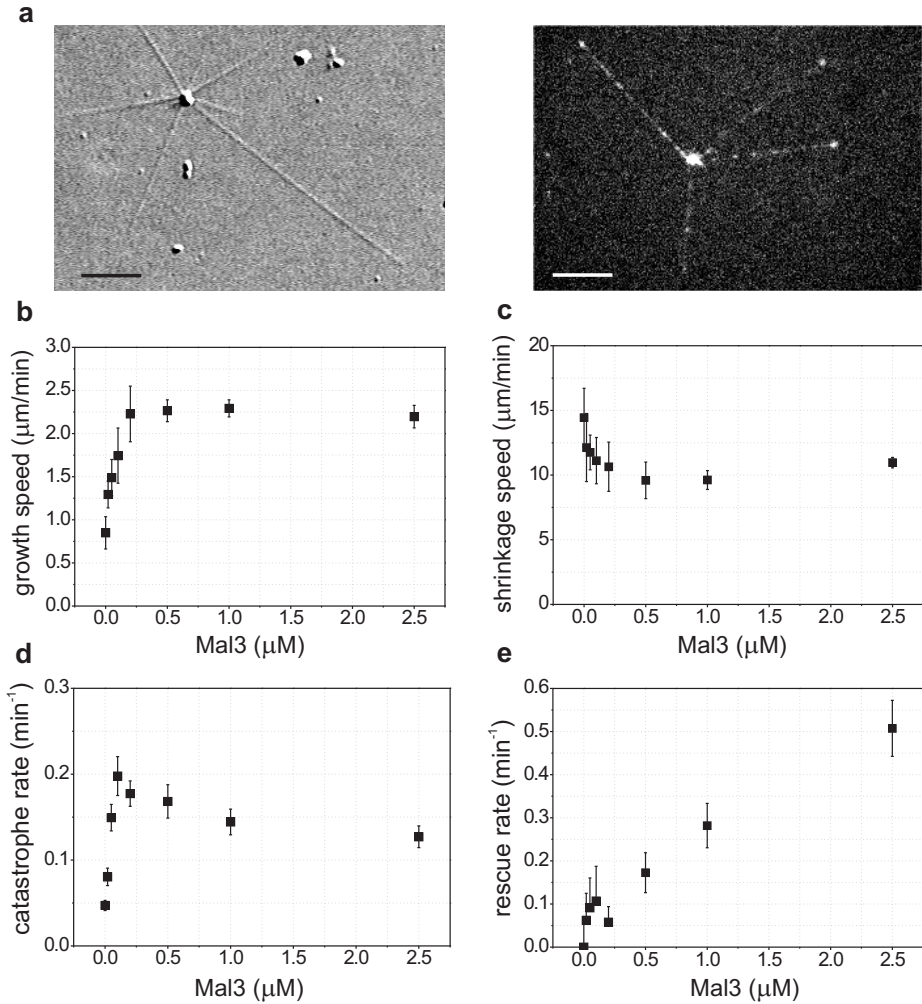


**Figure 5.1: Dynamic instability parameters.** (a) A video-enhanced DIC micrograph of centrosome nucleated microtubules (left) and a confocal image showing the Mal3-Alexa 488 (100 nM) tracking the microtubule growing ends (right). Scale bars are 5  $\mu\text{m}$ . (b) Growth speeds, (c) shrinkage speeds, (d) catastrophe rates and (e) rescue rates of microtubules in the presence of different concentrations of Mal3. Microtubules were assembled from 15  $\mu\text{M}$  tubulin and with 50 mM KCl present in solution, at 25  $^{\circ}\text{C}$ . For each data point we cumulated data from 3 - 6 independent experiments. Data are presented as (mean  $\pm$  sd) (data analysis described in section 5.5.1).

### 5.2.2 Mal3 interacts differentially with the tip and with the lattice of growing microtubules.

We showed in chapter 4 that Mal3 tracks the ends of growing microtubules by an end recognition mechanism, i.e. having an enhanced binding at the growing end structure as compared with the lattice [124]. In order to investigate if there is a correlation between the observed changes in the microtubule dynamics and the differential binding of Mal3 on the microtubules, we used confocal microscopy to image Alexa 488 labelled Mal3 on dynamic microtubules.

For each Mal3 concentration we analyzed profiles from 3 - 4 independent experiments and in each experiment 10 - 70 microtubules were analyzed. We first evaluated the average Mal3-Alexa 488 background intensity in each experiment in order to test the quality of our method employed for the image processing and the profile analysis (section 5.5.2). We expect a linear dependency between the Mal3 concentration and the average Mal3-Alexa 488 background intensity measured in each experiment. Figure 5.2 b shows indeed a linear dependency of the average background intensity,  $I_{\text{background}}$ , on the Mal3 concentration. The spread in the background intensity between the samples prepared at the same Mal3 concentration was significant, especially at low Mal3 concentrations (inset in figure 5.2 b). This spread is due to the errors in the protein concentrations resulting from the sample preparation. In order to exclude the experimental errors, we chose to present quantities evaluated from the profile analysis as a function of the background intensity.

The microtubule profiles of Mal3-Alexa 488 showed a clear difference between the signal at the tip and on the microtubule lattice (figure 5.2 a) for the whole range of Mal3 concentrations investigated. From the microtubule profiles we evaluated three quantities: the relative amount, as compared with a control sample, of Mal3 bound on the microtubule lattice,  $I_{\text{lattice}}$ , the amount interacting with the microtubule growing end,  $I_{\text{tip}}$ , and the typical length of the tip signal,  $\sigma_{\text{tip}}$  (see section 5.5.2).

The average signal on the lattice was increasing proportionally with the amount of Mal3 present in solution (a linear fit seems to be a good approximation to the data, figure 5.2 d), indicating a simple first-order interaction of the protein with the microtubule lattice. Mal3 was shown to bind preferentially at the seam [25], but we do not exclude binding elsewhere on the lattice. The lattice binding sites for Mal3 did not saturate in the range of Mal3 concentrations investigated here. This linear-increase behavior is very similar with the one observed for the rescue rate in the presence of Mal3 (figure 5.1 e). The similarity of the two results indicates that the Mal3 bound on the microtubule lattice affects rescue rates. One of the possible underlying mechanisms, recently revealed by cryo electron-microscopy [25], is the increased stability of the microtubule lattice, primarily due to the microtubule seam stabilization by Mal3.

At the microtubule tip, remarkably, the average signal showed elevated intensity even at very low Mal3 concentrations demonstrating a potent binding of Mal3 at the growing end. This elevated efficiency of binding could be due to a low dissociation con-

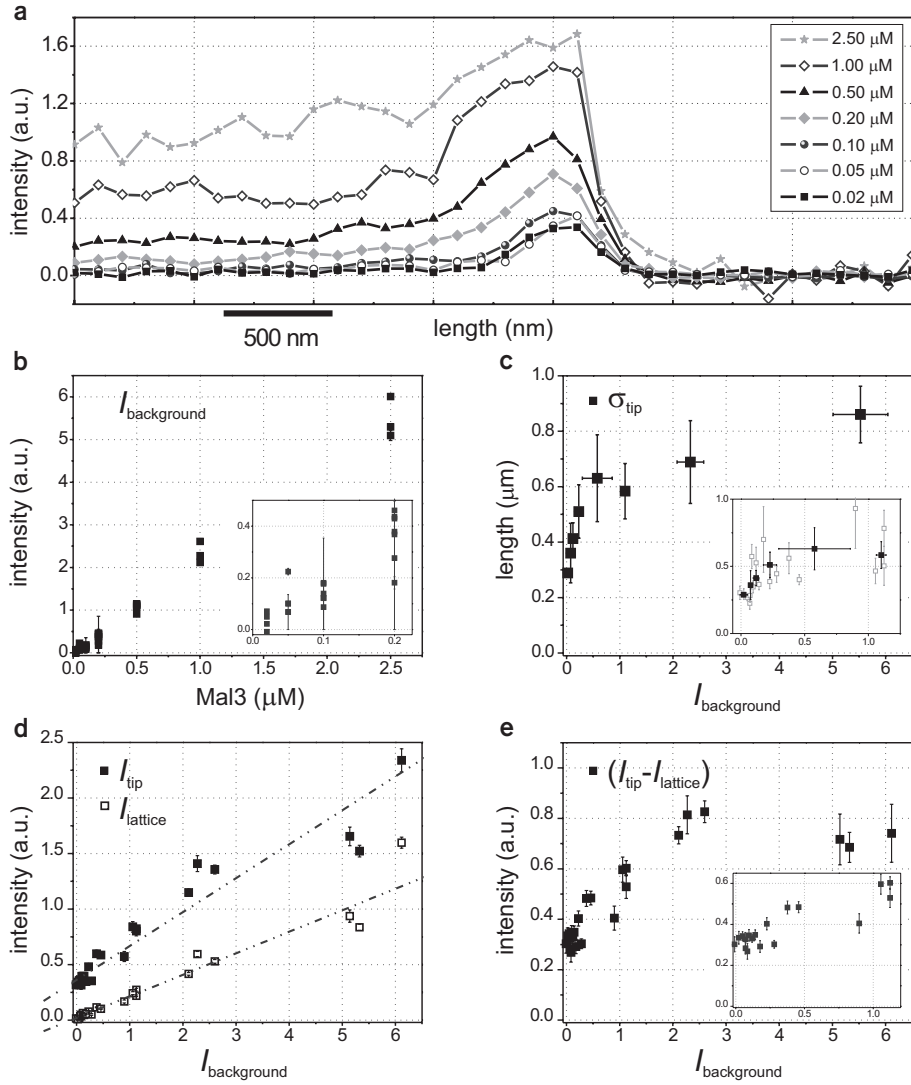


**Figure 5.2: Mal3-Alexa 488 binds differentially on growing microtubules.** (a) Mal3 intensity profiles along microtubules measured at the indicated concentrations of Mal3. Each profile is the average of about 10 - 70 microtubules from one experiment. (b) The normalized background intensity,  $I_{\text{background}}$ , as a function of the Mal3 concentration follows a linear relationship, as expected. (c) The spatial extent of the Mal3 signal at the microtubule tip,  $\sigma_{\text{tip}}$  as a function of the background intensity. The data (open symbols in the inset) were binned over 3 data points. The x-errors represent s.d. and the y-errors are s.e.m. (d) Normalized intensity of Mal3 present at the tip,  $I_{\text{tip}}$ , (solid symbols) and on the microtubule lattice,  $I_{\text{lattice}}$ , (open symbols) as a function of the background intensity. Dotted lines are linear fits to the data. The intensity  $I_{\text{tip}}$  was evaluated over the tip region,  $\sigma_{\text{tip}}$ . The difference,  $(I_{\text{tip}} - I_{\text{lattice}})$ , is shown in (e). The normalized intensities presented in (d) and (e) represent values per image pixel ( $110 \times 110 \text{ nm}^2$ ) and are proportional with the amount of Mal3 (see section 5.5.2). Data was collected from 24 independent experiments. Insets: zoom in the initial part of the data. Error bars represent s.e.m. For the difference signal, the errors were calculated by error propagation.



stant ( $K_D = k_{\text{off}}/k_{\text{on}}$ ) of Mal3 at the tip compared with the lattice and/or due to a higher number of available binding sites. The sharp transition of the tip signal from zero (no Mal3 present in solution) to the condition with Mal3 present, followed by an almost linear increase in the tip signal (figure 5.2 d), indicate different interaction kinetics of the protein at the growing end as compared to the interaction with the microtubule lattice. When we plot the difference signal between the tip and the lattice (figure 5.2 e) we noticed a similar saturation behavior of the signal as for the microtubule growth speed and the catastrophe rate (figure 5.1 b and d). This observation implies that, at the tip, there are lattice-like binding sites that do not saturate in the regime of concentrations investigated and tip-specific binding sites that saturate, similarly with the growth speed and catastrophe rate. This correlation suggests that Mal3 present at the tip induces structural and/or biochemical changes at the tip that affect both the tubulin incorporation rate and the chance of switching to a shrinking phase.

We also measured an increase in the spatial extent of the tip signal with the Mal3 concentration (figure 5.2 c). The region with higher Mal3 concentration at the microtubule tip was increased more than 4-fold in the presence of Mal3 to a length of approximately 800 nm. At low concentrations of Mal3 we measured a spatial extent of the Mal3 signal of 250 nm, but the measurement is probably limited by the optical resolution. As shown in chapter 4 and [124], Mal3 most probably recognized an end-structure at the growing microtubule tip. Our result suggests that in the presence of Mal3 microtubules have longer end-structures. To further investigate the influence of Mal3 on these tip-specific structures we followed microtubule assembly and disassembly with our optical tweezers based technique that provides near molecular resolution.

### 5.2.3 Mal3 promotes formation of microtubule end-structures.

When Mal3 was present in high concentration (1  $\mu\text{M}$  and higher), we sometimes observed curved, elongated structures at the end of growing microtubules (figure 5.3). These structures could be malformed tubes or some specific end structure different than a closed tube. The fact that the curved structure can be straightened while the microtubule is growing suggests that there is no defect in the tube growth, but rather an extended end-structure before closing into a tube. These observations together with the fluorescent measurements on Mal3 spatial extent at the tip suggest that Mal3 promotes formation of elongated microtubule end-structures. In order to gain more information about the changes induced by Mal3 at the microtubule tip we measured microtubule growth at high-resolution using optical tweezers (method described in chapter 2). Our preliminary experiments and observations are presented below.

Figure 5.4 a shows microtubule growth traces in the absence (upper panel) and in the presence of 200 nM Mal3 (lower panel) measured with optical tweezers. In these experiments, microtubules grew under force (indicated on the right axis), which is known to affect their dynamics [70, 76, 77]. In both experiments shown in figure 5.4 a the average and the maximum force experienced by the growing microtubules were similar.

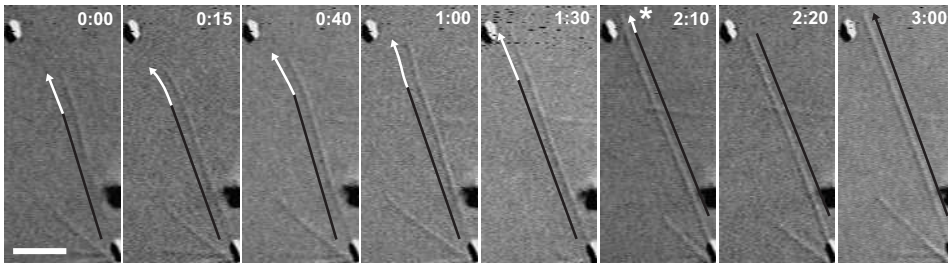


**Figure 5.3: Microtubule end-structure in the presence of Mal3.** Time sequence of DIC images of a growing microtubule in the presence of 1  $\mu\text{M}$  Mal3. Schematic guiding lines (shifted with respect to the image) of the dynamic microtubule are drawn. An arrowed line indicates growth. A curved structure, 2 - 3  $\mu\text{m}$  in length, (white part of the line) is elongating at the microtubule tip and straightens while the microtubule is growing (the black part of the line represents the straight microtubule). The end-structure had a catastrophe (asterisk in frame 2:10) and depolymerized until the straight part of the microtubule. The time elapsed from the first image is indicated in min : sec. Scale bar is 3  $\mu\text{m}$ .

Zooming in on the high-resolution traces, we noticed variabilities in speeds during one continuous event both for the growth and for the shrinkage phases (figure 5.4 b). For the depolymerization events we could clearly identify two types of processes: slow and fast depolymerization (empty and solid arrow heads, respectively, in figure 5.4 b). The microtubule depolymerization events often started with a slow phase followed by a fast shrinkage. Sometimes multiple slow and fast length reductions were identified during a depolymerization event. We also observed shrinkage events that could be entirely described by slow depolymerization, mostly in the Mal3 samples (figure 5.4 b).

In order to quantify the effect of Mal3 on microtubule assembly and disassembly, we evaluated growth and shrinkage speeds of short data stretches where the growth and, respectively, the shrinkage speed was approximately constant (data analysis described in section 5.5.3). For the two conditions investigated (absence and presence of Mal3), we analyzed the growth and the shrinkage events of microtubules from two independent experiments (part of the two data sets are shown in figure 5.4 a). The distributions of speeds are shown in figure 5.5. In the optical tweezers experiments, the microtubule average length was much shorter (100-400 nm) as compared to the average length in the absence of force, in the DIC experiments (couple of micrometer). Therefore, our data from the high-resolution experiments refer to growth and shrinkage speeds on a smaller length and time scale. In the time scale there is typically a factor 10 difference between the two methods.

For the growth events we evaluated growth speeds only on stretches that displayed predominantly microtubule length increase and we excluded the more extensive pauses and length reductions during growth. Therefore the mean values are overestimated and the comparison between the effect of Mal3 on the growth speed measured with the two methods, optical tweezers and DIC, is only qualitative. In the absence of Mal3

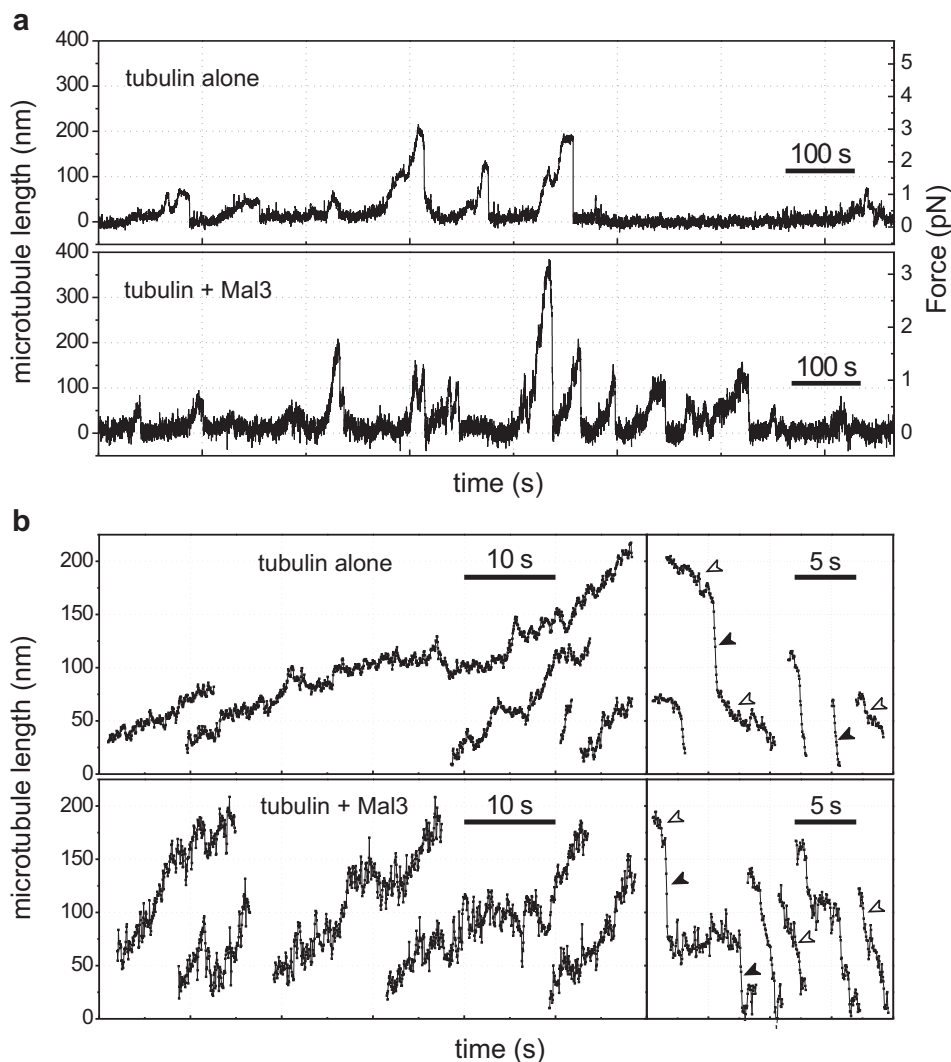


**Figure 5.4: Microtubule assembly measured with optical tweezers.** (a) Growth and shrinking events of individual microtubules in the absence (top panel) and in the presence of 200 nM Mal3 (lower panel). The microtubules grow and shrink in the presence of an opposing force (indicated on the right axis). (b) Selected growth and shrinkage events shown at higher magnification. Empty arrowheads indicate slow depolymerization phases and solid arrowheads indicate fast length decreases.

we measured reduced growth speeds with a weighted average of  $0.48 \pm 0.08 \mu\text{m min}^{-1}$  (mean  $\pm$  s.e.m.;  $n = 18$ ) as compared with the average growth speed measured on freely growing microtubules in the DIC experiment,  $0.88 \pm 0.03 \mu\text{m min}^{-1}$  ( $n = 99$ ) (figure 5.5 a, top panel). This effect was expected due to the fact that microtubules in the optical

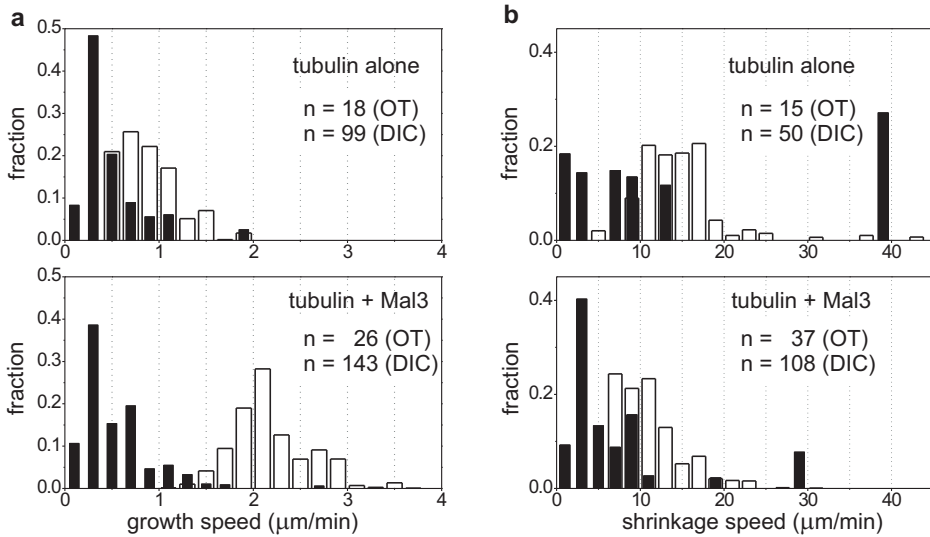


**Figure 5.5: Quantifying growth and shrinkage speeds.** Weighted distributions of (a) growth speeds and (b) shrinkage speeds for microtubules grown in the absence (top panels) and in the presence of 200 nM Mal3 (lower panels). The empty-bar distributions were evaluated from the DIC experiments with microtubules growing freely from centrosomes. The black solid-bar distributions were evaluated from the high-resolution measurement with optical tweezers (OT). The contribution of each speed in the distributions was weighted with the time extent of the corresponding event for the DIC data, growth and shrinkage events, and for the OT data, only growth events. Each shrinking event measured with the OT was weighted with the length reduction during the event. The total number of data stretches ( $n$ ) used to compute the distributions are indicated.

tweezers experiment were growing against a force, which reduces the growth speed [70,76,77]. In the presence of Mal3 the average growth speed was reduced more strongly from  $2.18 \pm 0.03 \mu\text{m min}^{-1}$  without force ( $n = 143$ ) to  $0.53 \pm 0.07 \mu\text{m min}^{-1}$  under force ( $n = 26$ ) (figure 5.5 a, lower panel). This effect could be interpreted in two ways: i) force has a different effect on microtubule growth when Mal3 is present at the end, consistent with an altered end-structure in the presence of Mal3 or ii) the presence of an opposing force impedes Mal3 to exert its effect at the microtubule tip. More experiments are necessary to elucidate the underlying mechanism.

Shrinkage speed distributions evaluated from the high-resolution traces displayed an interesting behavior as compared to the DIC data analyzed at low-resolution. We measured a relatively high number of data stretches that displayed a much lower shrinkage speed than the average speed measured in the DIC experiment, both for the tubulin alone and in the presence of 200 nM Mal3. These slow events appear in the weighted distribution as peaks in the speed range below  $5 \mu\text{m min}^{-1}$  (figure 5.5 b). The slow events were typically present at the onset of the depolymerization phases, spanning few tens of nanometers and a couple of seconds. In DIC we would not be able to mea-

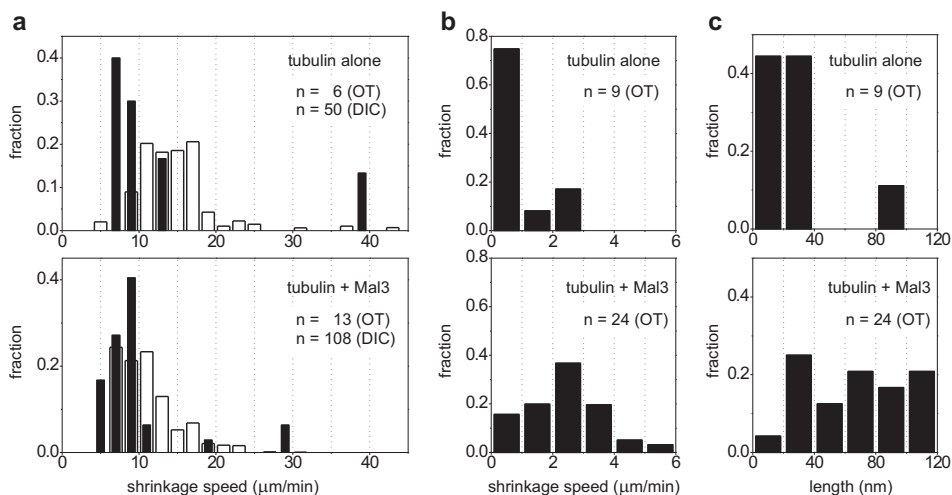


**Figure 5.6: Quantifying the slow and the fast shrinkage events.** Weighted distributions of (a) fast and (b) slow shrinkage speeds for microtubules grown in the absence (top panels) and in the presence of 200 nM Mal3 (lower panels). The empty-bar distributions were evaluated from the DIC experiments with microtubules growing freely from centrosomes. The black solid-bar distributions were evaluated from the high-resolution measurement with optical tweezers (OT). The contribution of each speed in the distributions was weighted with the time extent of the corresponding event. (c) Length distributions of the slow disassembly stretches in the presence and absence of Mal3. The slow events are the same as used in (b).

sure such events, given the typical resolution of microscopy. Therefore, the most probable explanation for the lack of peaks below  $5 \mu\text{m min}^{-1}$  in the DIC data is the limited resolution of the DIC method.

Due to the fact that almost all shrinkage events started with a slow length-decrease followed by fast depolymerization, we think that the slow length-decrease represents the event that triggers microtubule fast depolymerization. As further discussed in chapter 6 this event could be the disassembly of the end-structure or loss of lateral contacts between the protofilaments at the microtubule tip. Following this idea, the shrinkage events that are completely described by slow length-decrease could represent disassembly of incomplete microtubules that only have an end-structure, which did not yet close into a tube to form a regular microtubule lattice.

To further investigate the possible influence of Mal3 on these slow depolymerization phases we evaluated weighted speed distributions separately for the fast and the slow events (figure 5.6). Slow speeds were selected as speeds in the range below the minimum shrinkage speed measured in the DIC experiment ( $< 5.5 \mu\text{m min}^{-1}$ ). The fast speeds represent the speeds higher than this threshold ( $> 5.5 \mu\text{m min}^{-1}$ ). For the fast length reductions we measured similar average speeds at high- and low-resolution (figure 5.6 a). Mal3 slowed down depolymerizing microtubules in both experiments: from

$13 \pm 5 \mu\text{m min}^{-1}$  ( $n = 6$ ) for tubulin alone to  $10 \pm 2 \mu\text{m min}^{-1}$  ( $n = 13$ ) in the presence of Mal3 measured with optical tweezers, similar to the decrease from  $14 \pm 1 \mu\text{m min}^{-1}$  ( $n = 50$ ) to  $11 \pm 0.4 \mu\text{m min}^{-1}$  ( $n = 108$ ) in the DIC experiment (weighted average speeds are presented as mean  $\pm$  s.e.m.). This similarity suggests that the fast length decreases measured with optical tweezers are underlined by regular microtubule depolymerization.

In contrast, the slow shrinkage events most probably reflect depolymerization of a different microtubule structure, e.g. an open tube or a sheet-like structures, or a conformational change at the tip (see also chapter 6). The speed and length distributions for the slow length-decreases are shown in figure 5.6 b and c. From the total microtubule length in the shrinkage phases approximately 60% was lost through slow disassembly in the presence of Mal3, while for tubulin alone only 33% of the total length was covered by the slow stretches. In the presence of Mal3 slow shrinkage occurred at an average speed of  $2.4 \pm 0.3 \mu\text{m min}^{-1}$  ( $n = 24$ ) and the slow events had an average length of  $67 \pm 6$  nm. In the absence of the protein the slow phases of depolymerization had an average speed of  $1.0 \pm 0.3 \mu\text{m min}^{-1}$  ( $n = 9$ ) and an average length of  $28 \pm 7$  nm. Average speeds and lengths are presented as mean  $\pm$  s.e.m. The differences in speed and average length might reflect different events at the microtubule end: one prior to fast shrinkage, both in the absence and in the presence of Mal3, and one representing depolymerization of incomplete microtubules, observed mostly in the Mal3 sample. Only in the presence of Mal3 we frequently observe complete slow depolymerization events, pointing to fact that Mal3 promotes formation of end-structures. Further experiments are necessary to elucidate the nature of slow depolymerization and the influence of Mal3 on the end-structure (see also discussion in chapter 6).

### 5.3 Discussion

We found that Mal3 influences microtubule dynamics in various ways. Mal3 bound potently to the tip of growing microtubules. The protein presence at the tip enhanced the addition of tubulin dimers and increased the chance of catastrophes. On the other hand Mal3 had a stabilizing effect on the pre-existing protofilaments that form the lattice as we measured reduced shrinkage speeds and increased microtubule rescue rates.

The enhancement of tubulin net incorporation at the microtubule end in the presence of Mal3 could be explained by two scenarios: i) Mal3 binds to tubulin in solution and the formed complexes have higher affinity for the microtubule tip or ii) Mal3 binds at the microtubule growing end and induces changes that in turn facilitates the addition of new tubulin subunits. As described in chapter 4, the average time Mal3 decorated the microtubule-ends was much higher than the dwell time of individual Mal3 molecules (the time one molecule stayed bound) at the microtubule tip. This indicates that Mal3 recognizes the growing end-structure where it turns over rapidly. Also, gel filtration experiments revealed a weak interaction between tubulin and Mal3 in solution [124].

Taken together, these observations support the second scenario, in which Mal3 binds at the tip and changes the microtubule end-structure, most probably both biochemically and structurally. The tubulin dimers will have higher affinity for this Mal3-decorated end-structure. However, some contribution of the first scenario cannot be excluded, but due to the weak interaction between tubulin and Mal3 in solution, only a small amount of tubulin will be incorporated through enhanced co-polymerization of Mal3-tubulin complexes. The fact that we saw a saturation in the Mal3-induced enhancement of the growth speed indicates that the binding sites for Mal3 at the microtubule tip are limited. This idea is also supported by the observed saturation of the fluorescent Mal3 signal at the microtubule end (the tip signal above the lattice one) in the high range of concentration investigated. We observed a concentration lag between the saturation regime for the amount of Mal3 interacting at the microtubule tip and the saturation regime of the microtubule growth speed. This could mean that the microtubule end-structure recognized by Mal3 includes a higher number of Mal3 binding-sites than the ones where Mal3 affects tubulin incorporation.

In the presence of Mal3, we measured longer end-structures at the microtubule tip by monitoring the spatial extent of the region decorated with fluorescent protein at the microtubule tip. Longer end-structures in the presence of Mal3 could be explained by the increased microtubule growth speed, as previous electron microscopy experiments showed that faster growing microtubules display longer sheet-like structures at the growing end [34]. Indeed, the length enhancement of the Mal3 decorated end-structure correlated with the growth speed enhancement in the presence of Mal3. This effect was measured also when tubulin concentration was varied resulting in faster growing microtubules decorated by longer Mal3 comets (chapter 4).

According to previous data measured on dynamic microtubules [56,57], an increase in the growth speed correlates with a lower catastrophe rate. We measured an opposite effect in the presence of Mal3. The increased catastrophe rate induced by Mal3 correlated with the increase of the growth speed, showing that the protein bound at the microtubule end is not only enhancing the net rate of tubulin subunit incorporation, but also the chance of having a catastrophe. Our high-resolution data on disassembling microtubules revealed that Mal3 promotes formation of end-structures that depolymerize before closing into a regular microtubule. This effect could contribute to the increased switching from a growing to a shrinking phase. Previous work done *in vivo* suggested that removal of Mal3 from microtubule tips may be a prerequisite for a catastrophe to occur [109]. Our data suggest that Mal3 is most probably "removed" together with the tubulin by disassembly of the end-structure.

After a maximal Mal3-induced enhancement of the catastrophe rate we observed a slow decrease in the rate with Mal3 concentration. The catastrophe rate remained though elevated as compared with the tubulin control. These observations indicate that Mal3 present at the tip had both destabilizing and stabilizing effects. *In vivo*, the ratio Mal3:tubulin is in the order of 1:200 as roughly estimated from a bulk experiment

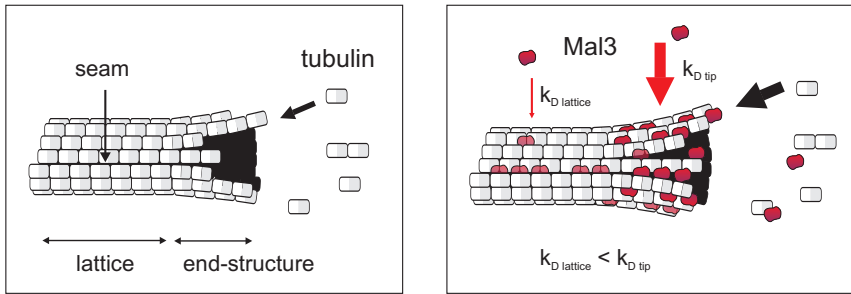


**Figure 5.7:** Schematic drawing of a growing microtubule end in the absence (left) and in the presence of Mal3 (right). Mal3 interacts differentially at the microtubule end and on the lattice.

[25]. This ratio, in our experiments, correlates with a region of Mal3 concentration after the maximum enhancement of the catastrophe rate induced by Mal3.

The dual effect of Mal3 observed on the catastrophe rate is underlined by the interaction of Mal3 and tubulin at the microtubule tip. As the end-structure present at the tip is continuously growing and changing into a tube, the interaction of Mal3 at the tip could be most probably described by a combination of end-specific interactions and lattice-like interactions. The destabilizing effect of Mal3, probably due to the end-specific interactions, seemed to be predominant. The end-structure that resemble the lattice could be responsible for the second stabilizing effect, though less potent.

We did not detect an accumulation of Mal3 at the tip of shrinking microtubules. Therefore the observed increase in the rescue rate and the decrease in the shrinkage speed might be correlated with a change in the lattice properties. The rescue rate increase was proportional with the amount of Mal3 on the lattice and in solution, whereas the shrinkage speeds after an initial decrease remained constant when we increased Mal3 concentration. This could suggest that Mal3 has a dual effect also at the lattice. Previous work showed that Mal3 binds preferentially to the seam of microtubules and increases the lattice stability [25]. This increased stability could be dependent on the amount of Mal3 bound to the seam. Shrinkage speed might be mainly influenced by the seam stability. Assuming this correlation between the amount of Mal3 present at the seam and the shrinkage speed (the more Mal3 at the seam, the more stable lattice and slower shrinking microtubules), we expect a saturation in the down-regulation by Mal3 of the shrinkage speed when the seam binding sites are saturated with Mal3. Our data supports this idea. However, the amount of Mal3 bound on the lattice did not saturate in the range of concentrations investigated. This could be an indication that Mal3 binds on the whole lattice, not only at the seam. The rescue rate enhancement correlates with the amount of Mal3 interacting with the lattice, suggesting that the protein on the lattice has an influence on the recovery of microtubules during shrinking events. Although we did not detect fluorescent signal of Mal3-Alexa 488 at the tip of shrinking microtubules, we cannot exclude an end-effect of Mal3 that enhances rescue rates. Fur-



ther experiments are needed to elucidate the extent of Mal3-binding sites at the lattice and whether Mal3 has an interaction with the shrinking microtubule ends.

In conclusion, Mal3 affects differentially the tip and the microtubule lattice (figure 5.7). At the microtubule end, Mal3 binds efficiently, where it enhances the tubulin incorporation and promotes catastrophes. At the lattice, Mal3 binds and stabilizes lattice-specific structures that are also present, to some extent, within the microtubule end-structure. As a result Mal3 slows down shrinking microtubules and has a second, though less potent, stabilizing effect at the microtubule end-structure. At the lattice Mal3 binds with low affinity and promotes microtubule rescues.

## 5.4 Additional remarks

Two recently published studies report the influence of EB1, the human end-binding protein, on microtubule dynamics *in vitro* [111,187]. Manna et. al [111] reports that EB1 had minimal effect on the microtubule growth speed and the rescue rate. The main effect was observed on the shrinkage speed and the catastrophe rate, the presence of EB1 decreasing disassembly speed and suppressing catastrophes. The only common observation between this study and our measurements with Mal3, is the observed decrease in the shrinkage speed. In the second report [187], Vitre et.al reveals yet an influence of EB1 on all dynamic instability parameters. The authors found that EB1 stimulates spontaneous nucleation and growth of microtubules, and promotes both catastrophes and rescues. The extent of the EB1 influence on microtubule dynamics is almost identical with our Mal3 measurements. Using cryo-electron-microscopy, the authors could observe longer tubulin sheets at the microtubule ends in the presence of EB1. Our similar observation corroborates with this result.

The differences between the two studies remain to be clarified. The experimental method used in [187] resembles closely our DIC method. Given the similarity between our observations, presented in this chapter, and the results from [187], one can conclude that the two homologs, EB1 and Mal3, rely on the same molecular mechanism to interact with microtubules and to influence microtubule dynamics.

Vitre et. al [187] propose a mechanism for catastrophes and growth enhancement based on EB1-stimulated growth and closure of the tubulin sheets: EB1 favors lateral association of free tubulin at microtubule-sheet edges. Based on our observations on the dynamic microtubule ends at high-resolution, we propose a mechanism in which Mal3 promotes formation of end-structures that frequently depolymerize, before having the chance to close into a tube. This mechanism might contribute to the observed enhancement of the catastrophe rate. Further experimental work is needed to clarify the molecular mechanism underlying the influence of Mal3 at microtubule ends.

## 5.5 Experimental procedures and data analysis

### 5.5.1 Measuring the parameters of microtubule dynamic instability by DIC microscopy.

**Sample preparation.** Experiments were performed in a flow chamber constructed between a microscope slide and a glass coverslip. Both glass surfaces were cleaned by immersion in chromosulfuric acid for few hours and subsequently rinsed with mili-Q water. The glass surfaces were separated by two parallel lines of silicone grease (high-vacuum silicone grease, Sigma) that were applied with a syringe on the microscope slide approximately 5 mm apart. The chamber was then filled with 6  $\mu$ l of assay buffer (80 mM K-PIPES, 1 mM EGTA, 4 mM  $MgCl_2$ , pH 6.8) and the volume was adjusted by pressing the coverslip down until the liquid completely filled the chamber. Subsequent solutions were flowed in by pipetting on one side of the chamber and blotting with tissue or filter paper at the other side.

We used centrosomes (a kind gift from Bornens lab, Curie Institute; isolated from cultured human lymphoblastic cells [188]) as microtubule nucleation sites. First, the centrosomes were non-specifically adhered on the glass coverslip. The glass surface was then passivated in two steps by incubation with 0.2 mg/ml PLL-PEG (poly-L-lysine (20 kDa) grafted to polyethylenglycol (2 kDa) with 3.5 lysine units per PEG chain) (Susos AG, Switzerland) in assay buffer, and further with 1 mg/ml  $\kappa$ -casein in assay buffer. After each step, except the last incubation with  $\kappa$ -casein, the flow chamber was washed with 30-100  $\mu$ l assay buffer. Passivation is necessary in order to minimize protein loss on the glass surfaces. Microtubule growth was initiated by flowing in a solution containing 15  $\mu$ M tubulin (bovine, Cytoskeleton, USA), 1 mM GTP and Mal3 (with a concentration ranging from 20 nM to 2.5  $\mu$ M) in assay buffer supplemented with 50 mM KCl, 0.1% methyl cellulose (4000cP, Sigma), 0.6 mg/ml  $\kappa$ -casein and an oxygen scavenger system (50 mM glucose, 400  $\mu$ g/ml glucose-oxidase, 200  $\mu$ g/ml catalase, 4 mM DTT). Methyl cellulose acts as a crowding agent preventing the microtubules to fluctuate away from the surface. Mal3 was a kind gift from Linda Sandblad (Brunner lab, EMBL) [25]. Before injection in the flow chamber, the tubulin solution was spun for 6 minutes in an airfuge (Beckman Coulter, A-100/30 rotor) at maximum speed (167000 x g) in order to remove protein aggregates from solution. The spinning was done with a cooled rotor in order to keep the tubulin solution below 10°C. After the tubulin solution was injected, the flow chamber was sealed with candle wax and transferred onto the microscope stage. Sample preparation was done at room temperature, 21°C. During the experiment, the temperature in the flow chamber was maintained at 25 $\pm$ 1°C.

**DIC microscopy.** Dynamic microtubules nucleated from the centrosomes were imaged by video-enhanced differential interference contrast (VE-DIC) microscopy (figure 5.1 a, left), using an inverted microscope (DMIRB, Leica) equipped with a 100x/1.3 NA oil immersion objective (HCX PL FLUOTAR, Leica). The temperature in the sam-

ple was adjusted and maintained constant by Peltier elements (Melcor) mounted on a sleeve around the objective and controlled by in-house built electronics. Images were acquired with a CCD camera (CF8/1, Kappa), further processed for background subtraction and contrast enhancement with an image processor (C5510 Argus 20, Hamamatsu Photonics) and digitized on-line at a rate of 1 frame per second (fps) with an in-house developed software (written and run in IDL). Simultaneously with the on-line digitization, the processed images were recorded on a DVD at video rate, 25 fps, with a commercial burner (DVD R-80, Philips).

After mounting on the microscope stage, the sample was first equilibrated to the set temperature, 25°C, for about 10 minutes. Each sample was then imaged for 30-45 minutes.

**Data analysis.** Microtubule length vs time traces were measured using ImageJ software. Microtubule length changes below five pixels could not be observed, resulting in a spatial resolution of our assay of  $\sim 0.5 \mu\text{m}$ . Growing and shrinking speeds were determined from linear fits on individual events. One event is defined as a continuous growth or shrinking phase of a dynamic microtubule. For each sample an average growth and shrinkage speed was determined as the average over all events weighted with the time of the individual events (equation 5.1). The weighted standard deviation was determined as well (equation 5.2).

$$v_s = \frac{\sum v_i t_i}{\sum t_i} \quad (5.1)$$

$$\text{sd}_s = \sqrt{\frac{n}{n-1} \frac{\sum (v_i - v_s)^2 t_i}{\sum t_i}} \quad (5.2)$$

where  $i$  denotes an individual event,  $v_i$  is the speed (growth or shrinkage) of the event  $i$ ,  $t_i$  is the time spanned by the event  $i$ , and  $n$  is the total number of events measured in the sample.

For each Mal3 concentration, 30 - 75 microtubules were analyzed from 3 - 6 independent experiments. A weighted average speed (growth and shrinkage),  $v_s$ , was determined in each of these experiments. The speeds  $v_s$  (3 - 6 per Mal3 concentration) were further used to calculate an average speed,  $\bar{v}$ , per Mal3 concentration. Figure 5.1 b, c shows ( $\bar{v} \pm \text{sd}$ ). The standard deviation,  $\text{sd}$ , reflects the precision between different experiments at the same Mal3 concentration. We do not show the standard deviation,  $\text{sd}_s$ , on the average speed,  $v_s$ , within one experiment, which mostly reflects the intrinsic variability of the microtubule growth and shrinkage processes (see also text in section 5.2, page 85).

The catastrophe and rescue rates were determined by dividing the total number of catastrophes or rescues observed,  $N$ , by the total time the microtubules spent in the growing phase or, respectively, in the shrinking phase. For each Mal3 concentration

data was cumulated from the independent experiments. As both catastrophes and rescues are random events, the statistical error with which  $N$  was measured could be approximated by  $\sqrt{N}$  (68.3% confidence level, corresponding to the standard deviation). This approximation only holds for large  $N$  ( $> 8$ ). For Mal3 concentrations below 500 nM, we observed very few rescues ( $\leq 8$ ). In this case only an upper bound (90% confidence level) could be estimated in determining  $N$  [53]. Another experimental consideration in measuring  $N$  is the limited spatial ( $\sim 0.5 \mu\text{m}$ ) and temporal (1 s) resolution of our assay. Missing the short and/or the fast events results in the underestimation of the catastrophe and the rescue rate, as well as apparent slower growth and shrinkage speeds. This effect could be important at high Mal3 concentrations ( $> 1 \mu\text{M}$ ).

**Control experiments.** In our assay we used centrosomes as the microtubule nucleation sites. To check that our measurements on the dynamic instability parameters were not influenced by the possible residual proteins from the centrosome preparation, we prepared control samples in which microtubules were nucleated from seeds (short, stable GMPCPP microtubules) bound specifically on the surface of the flow chamber. The seeds were prepared by incubation of 30  $\mu\text{M}$  tubulin mix containing 17% biotin-labelled tubulin with 1 mM GMPCPP (Jena Bioscience, Germany) at 36°C for 40 minutes. We used the same tubulin batch to prepare seeds and in the polymerization mix. The seeds were bound to a biotin-functionalized surface via biotin-*streptavidin* links. The surface was prepared by subsequent incubations with 0.2 mg/ml PLL-PEG-biotin (poly-L-lysine (20 KDa) grafted to polyethylenglycol (2 KDa) with 3.5 lysine units per PEG chain and with 48% biotin attached to PEG (3.4 KDa) (Susos AG, Switzerland) and with 1 mg/ml *streptavidin* in assay buffer.

We compared the dynamic instability parameters of microtubule plus-ends grown from centrosomes and from the seeds for five different experimental conditions: tubulin alone and in the presence of 50 - 500 nM Mal3. We measured similar microtubule dynamics in the samples with centrosomes and with seeds.

### 5.5.2 Evaluating the amount of Mal3 bound on microtubules by confocal microscopy

**Sample preparation.** The samples were prepared in a similar way as for the DIC experiments, with the exception that Mal3-Alexa 488 was used in the protein mix. The Mal3 protein was purified and labelled as described previously [19, 124] (see also chapter 4). The labelling ratio was 0.9 of Alexa 488 dye per Mal3 protein molecule. Experiments were performed at 15  $\mu\text{M}$  tubulin.

**Confocal microscopy.** The fluorescently labelled Mal3 on dynamic microtubules was imaged with a confocal spinning disc microscope, comprising a confocal scanner unit (CSU22, Yokogawa Electric Corp) attached to an inverted microscope (DMIRB, Leica) equipped with a 100x/1.3 NA oil immersion lens (PL FLUOTAR, Leica) and a built-in

1.5x magnification lens. The sample was illuminated using a 488 nm laser (Sapphire 488-30 CHRH, Coherent Inc.). Images were captured by a cooled EM-CCD camera (C9100, Hamamatsu Photonics) controlled by software from VisiTech International. Images were acquired with exposures between 500 ms and 1 s. The laser intensity was varied depending on the Mal3 concentration in order to achieve a good signal to noise ratio. The temperature was controlled by maintaining the room at  $25 \pm 1^\circ\text{C}$ .

**Image processing and profile analysis.** We analyzed intensity profiles along growing microtubules. As we used different illumination conditions (laser intensity, exposure time and camera gain) for different samples, the raw images were first processed in order to be able to compare the microtubule profiles measured in different samples. Through the image processing we also corrected for the spatial illumination profile of our set-up, that had a 2D-Gaussian shape.

The intensity measured in each pixel of the raw image,  $\text{IM}_{\text{raw}}$ , was the summed contribution of several signals:

$$\text{IM}_{\text{raw}}(x, y) = N(x, y) \cdot E(x, y) \cdot f(I_{\text{laser}}, g, t_{\text{exp}}) + \text{IM}_0(x, y) \quad (5.3)$$

$$\text{IM}_0(x, y) = c_0 \cdot E(x, y) \cdot f(I_{\text{laser}}, g, t_{\text{exp}}) + f_0(g, t_{\text{exp}}) \quad (5.4)$$

where  $(x, y)$  is the pixel position,  $N$  is the number of Mal3-Alexa 488 molecules contributing to the signal of the pixel  $(x, y)$ ,  $E$  is the 2D-Gaussian profile of the illumination,  $f$  is a term that includes the non-linear dependency of the signal on the laser intensity,  $I_{\text{laser}}$ , and on the camera gain,  $g$ , and the linear dependency on the exposure time,  $t_{\text{exp}}$ .  $\text{IM}_0$  is the image acquired when there are no fluorescent molecules in the sample and it comprises two main contributions. One that depends on the laser intensity and was mainly due to laser leakage through the filters, and partly due to the autofluorescence of the glass and of the protein solution. This contribution can be written as the equivalent signal from a number  $c_0$  of fluorescent molecules ( $c_0$  should not depend on pixel position unless there are inhomogeneities on the filters or on the camera chip). The other contribution in  $\text{IM}_0$  was the dark camera noise  $f_0$  (camera signal when the sample was not illuminated). We processed the raw image  $\text{IM}_{\text{raw}}$  as indicated in equation 5.5 and obtained a normalized intensity,  $I_n$ , that does not depend anymore on the illumination conditions.

$$\text{IM}_p(x, y) = \frac{\text{IM}_{\text{raw}}(x, y) - \text{IM}_0(x, y)}{\text{IM}_{\text{ctrl}}(x, y) - \text{IM}_0(x, y)} \equiv I_n(x, y) \propto \frac{N(x, y)}{N_{\text{ctrl}}(x, y)} \quad (5.5)$$

where  $\text{IM}_{\text{ctrl}}$  is an image acquired in a control sample containing a solution of 300 nM Mal3-Alexa 488 together with all the other components of the polymerization mix and no centrosomes on the surface, thus no growing microtubules.  $N_{\text{ctrl}}$  represents the number of fluorescent Mal3 molecules contributing to the signal in the control sample. These molecules were mainly diffusing and only a very small fraction were non-specifically adhered on the surface. In the raw image, along a microtubule, the main

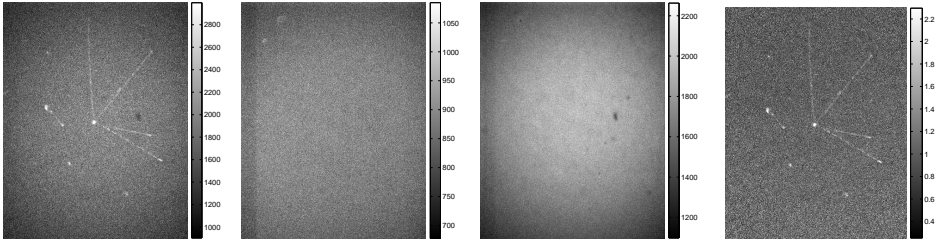


**Figure 5.8: Image processing.** From left to right:  $IM_{\text{raw}}$ ,  $IM_0$ ,  $IM_{\text{ctrl}}$ , and  $IM_p$ . The raw image was acquired in a sample with 300 nM Mal3-Alexa 488 and dynamic microtubules.

fraction of  $N$  was represented by the Mal3-Alexa 488 molecules interacting with the lattice or with the tip of the microtubule. Due to the different localizations within the point spread function of the microscope of the molecules (diffusing in solution or on surface) included in  $N$  and  $N_{\text{ctrl}}$ , the normalized intensity  $I_n$ , which we evaluated in the processed image  $IM_p$ , it is not equal, but proportional to the ratio  $N/N_{\text{ctrl}}$ . As  $N_{\text{ctrl}}$  was constant, any change in  $I_n$  along a microtubule or between samples directly reflects and it is proportional to real changes in  $N$ . The images  $IM_0$ ,  $IM_{\text{ctrl}}$ , and  $IM_{\text{raw}}$  were taken at identical illumination conditions and at similar depth in the sample, i.e. close to the surface where the dynamic microtubules were localized. For  $IM_0$  and  $IM_{\text{ctrl}}$  ten images were average to decrease imaging noise. An example of a processed image is shown in figure 5.8.

For almost half of the illumination conditions the signal measured in the control sample was low resulting in a very noisy difference image,  $IM_{\text{ctrl}} - IM_0$ , with the average intensity approximatively zero. In these cases we computed  $I_n(x, y)$  using a control image acquired at different illumination conditions,  $IM'_{\text{ctrl}}$ , that had a better signal to noise ratio (equations 5.6 and 5.7).

$$IM'_p(x, y) = \frac{IM_{\text{raw}}(x, y) - IM_0(x, y)}{IM'_{\text{ctrl}}(x, y) - IM'_0(x, y)} \equiv I'_n(x, y) \quad (5.6)$$

$$I_n(x, y) = I'_n(x, y) \cdot \frac{b}{b'} \quad (5.7)$$

where  $b$  is the background intensity evaluated in  $IM_p$  (equation 5.5) by averaging the pixel intensities in a couple of rectangles that included only surface without microtubules.  $b'$  was evaluated in a similar way in the processed image  $IM'_p$ , which was calculated using the control image acquired at the different illumination condition. We did not detect any bias in  $I_n$  between the two ways of evaluating it.

In the processed images, intensity line profiles were measured on individual microtubules (figure 5.9). One microtubule profile was the average of three adjacent line

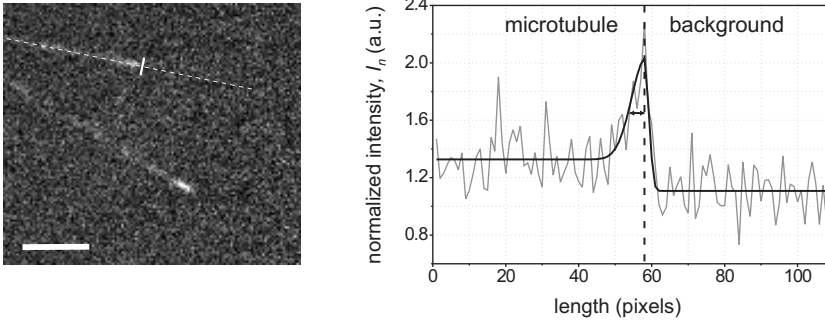


**Figure 5.9: Microtubule line profile.** Left: Fluorescent image of Mal3-Alexa 488 (500 nM) on dynamic microtubules. The line used to measure the profile (dotted line) was manually drawn and the initial guess of the microtubule tip (thick line) was evaluated from a step fit. Scale bar is 3  $\mu\text{m}$ . Right: The profile measured in the left image is shown and superimposed is the result of a fit combining two half-Gaussians. The fit yielded the microtubule tip position ( $x_{\text{tip}} = 58$ ) indicated by the dotted line and the standard deviation of the microtubule half-Gaussian ( $\sigma_{\text{tip}} = 4 \pm 1$  pixels) indicated by the double arrowed line.

scans to account for the point spread function (PSF) of the microscope. The intensities along a line scan were binned to pixel-size bins (the length of one pixel corresponded to 110 nm). A profile typically included 1 - 5  $\mu\text{m}$  stretch of the microtubule continuing with a 1 - 5  $\mu\text{m}$  stretch on the surface, along the microtubule line. An initial guess of the tip location was evaluated from a step fit on the profile. This value was used as initial parameter for a fit with the functional form given by two half-Gaussians, one for the microtubule stretch and one for the background stretch (equations 5.8 and 5.9).

$$G_{\text{mt}} = I_{\text{background}} + I_{\text{lattice}} + I_0 e^{-\frac{(x-x_{\text{tip}})^2}{2\sigma_{\text{tip}}^2}} \quad (5.8)$$

$$G_{\text{bkg}} = I_{\text{background}} + I_0 e^{-\frac{(x-x_{\text{tip}})^2}{2\sigma_{\text{psf}}^2}} \quad (5.9)$$

The fit had three parameters: the microtubule tip location,  $x_{\text{tip}}$ , the standard deviation of the microtubule half-Gaussian,  $\sigma_{\text{tip}}$ , and the shared maximum value of the Gaussians,  $I_0$ . The standard deviation,  $\sigma_{\text{psf}}$ , of the half-Gaussian for the background part,  $G_{\text{bkg}}$ , was fixed to one pixel, corresponding to the PSF of our confocal microscope. The signal along the microtubule end region is also convolved with the PSF. Therefore, the standard deviation determined at the microtubule tip,  $\sigma_{\text{tip}}$ , includes also the  $\sigma_{\text{psf}}$ .

From the fit parameters we used the microtubule tip location,  $x_{\text{tip}}$ , to align the microtubule profiles in one sample and we next averaged the aligned profiles (figure 5.2 a). In each sample 10 - 70 microtubules were analyzed. The standard deviation of the mi-

microtubule half-Gaussian,  $\sigma_{\text{tip}}$ , was evaluated from the fit on each individual profile. This value indicates the average spatial extent of the Mal3 interacting with the microtubule tip.

The average background,  $I_{\text{background}}$ , was evaluated as the average pixel intensity in a rectangle on a surface area close to the microtubule, or as the average pixel intensity of the surface stretch of the profile starting three pixels away from the microtubule tip. The amount per pixel of Mal3 interacting with the lattice, given as the normalized intensity  $I_{\text{lattice}}$ , was evaluated in each sample from the average profile as the average pixel intensity more than  $2\sigma_{\text{tip}}$  away from the microtubule tip minus  $I_{\text{background}}$ . The amount per pixel of Mal3 bound at the tip,  $I_{\text{tip}}$ , was evaluated as the average intensity of the pixels within the spatial extent  $\sigma_{\text{tip}}$  from the microtubule tip, minus  $I_{\text{background}}$ . The mean values and the corresponding s.e.m. for  $I_{\text{background}}$ ,  $I_{\text{lattice}}$ ,  $I_{\text{tip}}$ , and  $\sigma_{\text{tip}}$  (figure 5.2 b-e) were calculated averaging all the values estimated from fits on individual profiles in one sample.

**Control experiments.** We checked whether the Alexa 488 labelled Mal3, used for the confocal imaging, had the same behavior on microtubule dynamics as the unlabelled Mal3, used in the DIC experiment. We measured the dynamic instability parameters of microtubules grown in the presence of 100 nM and 200 nM Mal3-Alexa 488 and we found similar values with the ones evaluated for unlabelled Mal3. This agreement indicated that the presence of the Alexa label on Mal3 did not affect the protein interaction with the microtubules.

We also checked whether the binding of Mal3-Alexa 488 on microtubules was possibly influenced by residual proteins from the centrosome preparation. For this purpose we measured profiles on microtubules growing from the plus-ends of seeds (short stable GMPCPP microtubules). We did not find a difference in the amount of Mal3 present at the growing tip or on the microtubule lattice between the samples prepared with different nucleation sites.

### 5.5.3 Microtubule end dynamics measured with optical tweezers

Microtubules were nucleated from an axoneme. Growth and shrinkage of dynamic microtubules were monitored with high resolution using an optical tweezers based technique (method described in chapter 2).

**Sample preparation.** Microtubules grew against rigid barriers that were made from SU-8 photoresist (MicroChem) using standard lithography techniques [144, 150]. The coverslip carrying the SU-8 barriers were assembled into a home-made flow chamber. The chamber allowed injection of small samples (couple of microliters) by pipetting at an entrance opening and continuous slow flow by adjusting the height of the drain. The drain and the chamber were connected by teflon tubing and a computer-linked flow sensor (Seyonic, Switzerland) was inserted between the drain and the chamber in or-



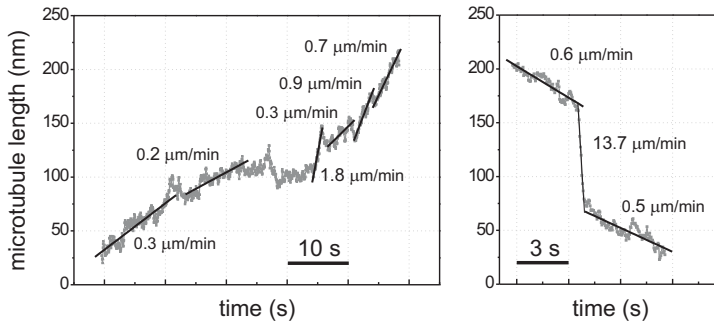


**Figure 5.10: Evaluating growth and shrinkage speeds.** Microtubule growth event (left) and the shrinkage event of the same microtubule (right). Solid black lines are linear fits on data stretched that have approximately constant speed. The speed values resulted from the fits are indicated.

der to monitor the magnitude of the flow. Prior to the sample injection, the chamber was passivated with 50 mg/ml BSA. Streptavidin coated polystyrene beads (2  $\mu\text{m}$  in diameter) were flowed in the chamber together with axoneme pieces (a kind gift from M. Footer). Using the optical trap a construct was assembled by non-specific attachment of a bead to one end of an axoneme. The construct was then positioned and held in front of a barrier by a ‘key-hole’ optical trap. Microtubule growth was initiated by flowing in the polymerization mix prepared in a similar way as for the DIC experiments.

**Data acquisition and analysis.** Microtubule growth against the rigid barrier resulted in bead displacement, which was measured off-line at a sampling rate of 25 Hz with the use of a standard auto-correlation method (in-house developed image processing software written and run in IDL). From the bead displacement we can evaluate the force against the growing microtubule (bead displacement multiplied with the trap stiffness) and the microtubule length after correction for the construct compliance. The construct compliance was determined before each experiment. With this method the microtubule length changes in time were processed with few nanometer resolution. Single events of growth and shrinkage were broken into a series of shorter events, stretches that could be approximated as having constant speed (figure 5.10). The growth and shrinkage speeds were evaluated from linear fits on these short data intervals and the corresponding weighted distributions were constructed. Each speed contribution was weighted with the time extent of the corresponding event (for the growth events) and with the total length change during the corresponding event (for the shrinkage events).

## Acknowledgements

I would like to thank Linda Sandblad for the kind gift of Mal3 protein and useful discussions, Peter Bieling and Liedewij Laan for help with purification and labelling of

Mal3, Liedewij Laan for help with initial experiments, and Christian Tischer for useful discussions.

*to be submitted:* Munteanu EL, Laan L, Brunner D, Surrey T, Dogterom M. Regulation of microtubule dynamics, *in vitro*, by the autonomous microtubule-end tracker Mal3.

---

## Microtubule catastrophes at molecular resolution

*Catastrophes, transitions from growth to shrinkage, are highly regulated in living cells. Information about the molecular events underlying catastrophes are limited to static cryo-EM images of growing and shrinking microtubules and modeling based on mechanochemical properties of tubulin. Here we used our high-resolution technique to zoom in on catastrophes of dynamic microtubule ends. We observed that fast disassembly events are typically preceded by a slow decrease in microtubule length of several tens of nanometers. We investigated whether this slow decrease is changed when microtubule associated proteins that affect the catastrophe rate, XMAP215 or Mal3, are added.*

In cells, microtubule dynamics are highly regulated in order to achieve specific functions at the right time and place. For example high turnover of microtubules at the onset of mitosis allows rapid reorganization of the microtubule array to form the mitotic spindle. How regulatory proteins interfere with the molecular events leading to a catastrophe, is still an open question. This is partly due to the lack of understanding of the molecular mechanism associated with catastrophes. It is well established that the dynamic instability of microtubules is driven by GTP hydrolysis. It was proposed that a stabilizing 'GTP-cap' is required for stable microtubule growth. When this cap is lost the microtubule will transition to rapid depolymerization. Based on cryo-EM micrographs it is believed that the stabilizing cap is represented by a sheet-like structure at the ends of growing microtubules. As shrinking microtubules are characterized by highly curved protofilaments, it is obvious that catastrophes must involve a structural change [39]. It was proposed that closure of the sheet results in a blunt end, corresponding to an intermediate between polymerization and depolymerization [61, 189]. Another idea emerging from cryo-EM studies was that during microtubule elongation, once in a while less stable lattice configurations form at the growing end that could be the origin of catastrophes [190].

In an attempt to shed more light on the molecular events underlying catastrophes, we used our high spatial-resolution technique to follow microtubule growth and shrinkage, and focused on the events right before a fast disassembly event.

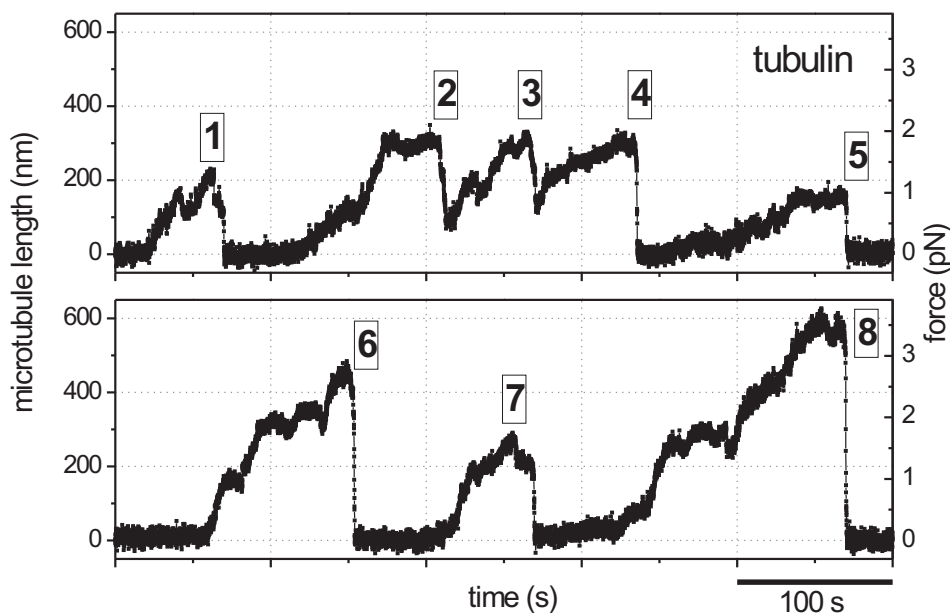


**Figure 6.1: Dynamic instability of microtubules measured with optical tweezers.** Microtubule length changes (left axis) and the force experienced by the dynamic microtubules (right axis) are plotted. Numbers indicate events with clearly recognizable catastrophes. Microtubules were grown from 5-20  $\mu\text{M}$  tubulin in the absence of MAPs at 25°C. The events presented in the two panels were measured using the same bead-axoneme construct.

## 6.1 Results

Figure 6.1 shows several growth and shrinking events of individual microtubules, measured with our optical tweezers based technique (chapter 2). Microtubules were grown from axonemes against a rigid barrier. In the trap, microtubules experience a force while growing, indicated on the right axis. A single microtubule growing and shrinking is exemplified by event 5 in figure 6.1. Events 2, 3, and 4 can be explained by the subsequent growth of multiple microtubules, as we do not expect to observe rescues in our experimental conditions. When the first microtubule was shrinking, the bead-axoneme construct moved towards the barrier until another growing microtubule came in contact with the barrier. From that moment on the bead moved again away from the barrier following the growth of the second microtubule. The axonemes used as nucleation centers are nucleating, on average, 1-2 microtubules under our experimental conditions. Even when multiple microtubules were growing from the axoneme, we attributed the shrinking events to single microtubules, as in this situations probably only one microtubule stayed in contact with the barrier.

### 6.1.1 Is there a molecular signature of catastrophes?

In order to identify a molecular signature of catastrophes, we focused on the events at the onset of fast disassembly events. Figure 6.2 shows individual shrinking events (a and b) for regular tubulin disassembly. For all the events we noticed a common feature: a slow microtubule length decrease prior to a fast disassembly event. Most of the slow length decreases display an approximately constant speed and can take up to several seconds before the microtubule undergoes fast disassembly. There is however a high variability between individual events in the spatial extent of this initial slow length decrease, which ranges from 0 nm to 150 nm (figure 6.2 b). There is also some variability in the total time spanned by the length decrease and in the speeds of the length decrease at short time scale: sometimes the length decrease includes several periods characterized by different depolymerization speeds.

In order to identify microtubule average behavior prior to a fast disassembly event, we aligned the individual segments at the onset of fast shrinkage. The average event is shown in figure 6.2 d. We could identify a reduction in length, which was characterized by a slow speed of  $3.1 \pm 0.2 \mu\text{m min}^{-1}$  (mean  $\pm$  s.e.m.) as evaluated by a linear fit over 0.65 s before the onset of the fast disassembly and a length extent of  $\sim 30$  nm. We were wondering if this length decrease was not due to the presence of force against which microtubules were growing. Microtubules experienced, on average, a stall force of  $1.4 \pm 0.2$  pN (mean  $\pm$  s.e.m.) (figure 6.2 c). It is possible that under force the bead-axoneme construct constantly rearranges its contact position at the wall, which might appear as a length decrease. To test this option we aligned at a random position pieces of data where the microtubules were stalled and calculated an average event. The average event measured from 14 data stretches showed a flat plateau (figure 6.2 f). Therefore we attribute the decrease in length to molecular events leading to fast shrinkage.

### 6.1.2 Microtubule catastrophes in the presence of XMAP215 and Mal3

As both XMAP215 (chapter 3) and Mal3 (chapter 5) had clear effects on the catastrophe rate of microtubules, we also investigated whether the two MAPs have a distinguishable effect on the microtubule length evolution just before a fast disassembly event.

Analysis of XMAP215 shrinking events (figure 6.3) revealed a similar length decrease prior to fast disassembly. Figure 6.3 d shows the average event in comparison with the one measured in the absence of XMAP215. The two events are almost identical. However, the individual events in the presence of XMAP215 often display a length decrease prior to fast disassembly that includes several periods of short length decreases, which are characterized by various speeds, together with periods of no length changes. This variability in shape is more often observed with XMAP215 than in the absence of XMAP215, when most of the events prior to fast disassembly are characterized by almost monotonous length decrease. The individual events in the presence of XMAP215 are plotted in figure 6.3 a. We also noticed pauses during the fast periods of shrinkage.

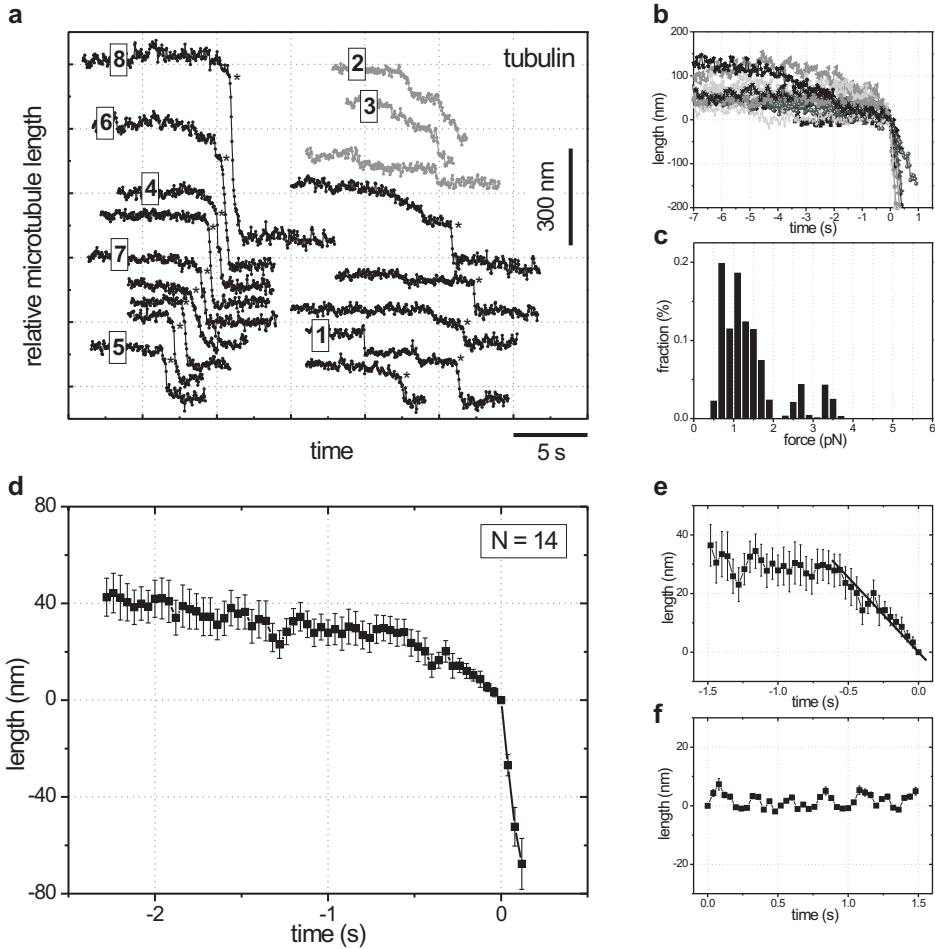


**Figure 6.2: Microtubule dynamics before fast depolymerization.** (a) Individual shrinking events of microtubules assembled in the presence 20  $\mu\text{M}$  tubulin. Numbered traces correspond to the shrinking phases of the events with the same numbers in figure 6.1. The black traces display clear events of fast shrinkage and were aligned at the onset of the fast disassembly phase (indicated by asterisks) with respect to both time and length. The aligned segments are shown in (b), in which the zero's of the coordinate system correspond to the alignment point. In the gray events from (a) we did not identify a fast disassembly event. (c) Histogram of stall forces including only the plateaus before a complete microtubule depolymerization event. Average stall force experienced by microtubules was  $1.4 \pm 0.2$  pN (mean  $\pm$  s.e.m.). (d) Average behavior of microtubules prior to a fast disassembly phase. The event was determined by averaging the aligned segments from (b) ( $n=14$ ). Error bars represent s.e.m. (e) Microtubule length changes during 1.5 seconds just before the fast disassembly phase are compared with (f) length changes during 1.5 seconds during the microtubule stall phase. Error bars are s.e.m. The slow reduction in microtubule length before fast disassembly had a speed of  $3.1 \pm 0.2$   $\mu\text{m min}^{-1}$  and it was determined from a linear fit (solid line in (e)) over 0.56 s until the onset of fast microtubule disassembly. The error on the speed represents standard error as determined from the linear fit.

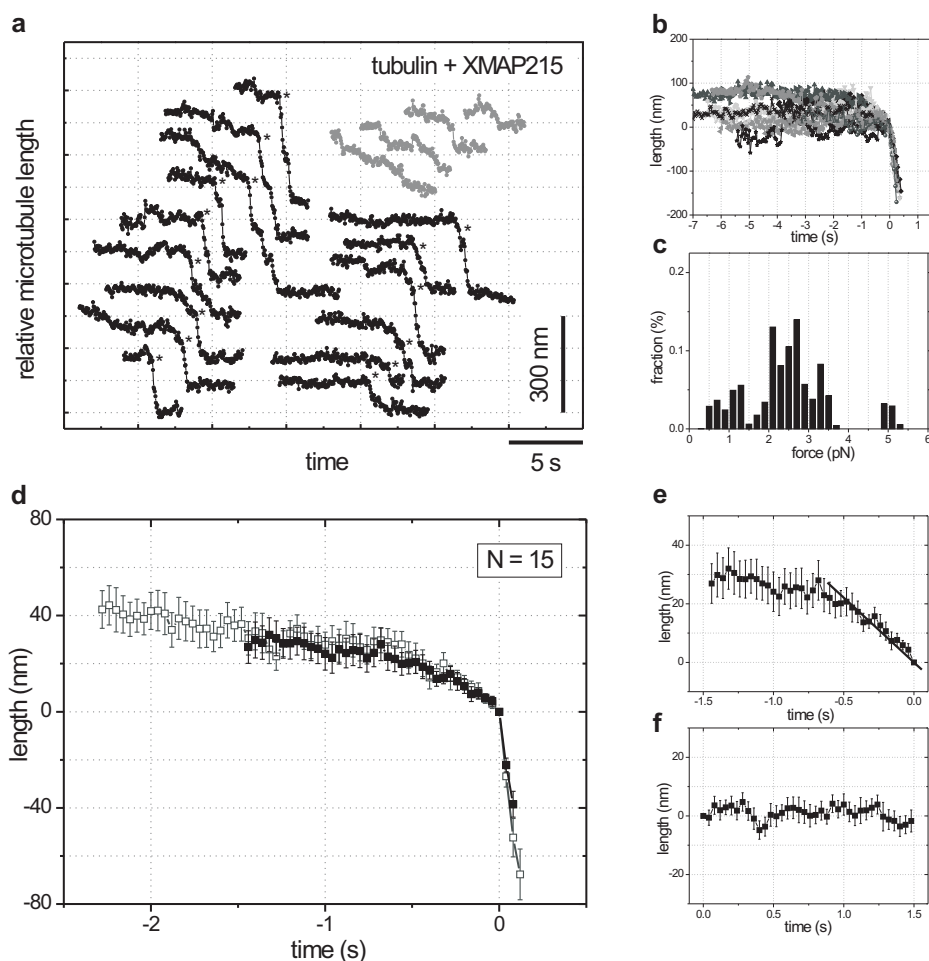


**Figure 6.3: Microtubule shrinkage in the presence of XMAP215.** (a) Individual shrinking events of microtubules assembled in the presence of 20  $\mu\text{M}$  tubulin and 150 nM XMAP215. Black traces display clear events of fast shrinkage and were aligned at the onset of shrinkage (indicated by asterisks). The aligned segments are shown in (b). (c) Histogram of stall forces. The average force experienced by microtubules before a catastrophe was  $2.4 \pm 0.3$  pN (mean  $\pm$  s.e.m.). (d) Average event prior to microtubule fast shrinkage in the presence of XMAP215 (solid symbols), determined from the aligned segments ( $n = 15$ ) shown in (b). The average event evaluated in the absence of XMAP215 (open symbols) (figure 6.2 d) is plotted for comparison. Error bars represent s.e.m. (e) Microtubule length changes during 1.5 seconds just before the fast disassembly phase are compared with (f) length changes during the microtubule stall phase. Error bars are s.e.m. The slow microtubule length reduction was characterized by a speed of  $2.7 \pm 0.2$   $\mu\text{m min}^{-1}$  as determined from a linear fit (solid line in (e)) over 0.56 s until the onset of fast microtubule disassembly. The error on the speed was evaluated from the linear fit.

These pauses resemble the slow length decrease prior to fast disassembly.

In the presence of Mal3 we identified two types of shrinkage events: fast and slow (figure 6.4 a, see also chapter 3). When we averaged the fast events we observed a similar length decrease prior to fast disassembly as in the absence of Mal3 (figure 6.4 d). We also averaged the slow shrinking parts of all events in the following way. The alignment point for the fast ones was the onset of fast disassembly, whereas for the slow ones the alignment point was the end of the slow shrinkage event. The average slow event when all events were included, shown in figure 6.4 d, displays a small up-shift compared with the tubulin or the average fast event. This means that, on average, the length loss through slow depolymerization was more extended in the presence of Mal3 as compared with the absence of the protein. The main contribution comes, however, from the shrinkage events entirely characterized by slow length decrease. The average shrinkage speed of these events is  $4.5 \pm 0.2 \mu\text{m min}^{-1}$  (figure 6.4 e), which is higher compared with the one measured for the length decrease prior to fast disassembly in the absence of Mal3.

## 6.2 Discussion on the mechanism of catastrophes

We can imagine two scenarios for the slow length decrease leading to microtubule fast shrinkage: i) disassembly of a stabilizing sheet-like structure at the microtubule end or ii) stochastic opening of the closed lattice configuration (cylinder) that exists at the end of a stalled microtubule. It is also possible that both scenarios occur sequentially before a fast disassembly event. In the first scenario, the end-structures should survive for up to a minute under force, as we measured stalled microtubules in this time regime prior to the event triggering fast disassembly. In the second scenario, the opening of the cylinder would possibly involve a length extent of several hundred nanometers in order to explain the apparent reduction of 30 nm, given the mechanics of microtubule ends (see section 3.3.1).

XMAP215 does not seem to have an obvious effect on this loss of tubulin dimers or tube opening prior to a fast shrinkage. The pauses during fast period of shrinkage in the presence of XMAP215 might be an indication that XMAP215 is present at the lattice where it has a stabilizing effect: the microtubule can undergo normal fast disassembly, preceded by the slow length decrease, until it encounters an XMAP215 molecule. XMAP215 temporarily prevents the fast disassembly and only when XMAP215 dissociates from the lattice, the microtubule can resume shrinkage.

In the presence of Mal3 we might observe different microtubule structures. The fast events could be interpreted as shrinkage of normal microtubules, that undergo a slow length decrease prior to fast disassembly. This mechanism that triggers microtubule depolymerization seem to be unaffected by the presence of Mal3. The events described entirely by slow shrinkage might represent depolymerization of incomplete microtubules, e.g. sheet-like structures. Mal3 seems to promote formation of such



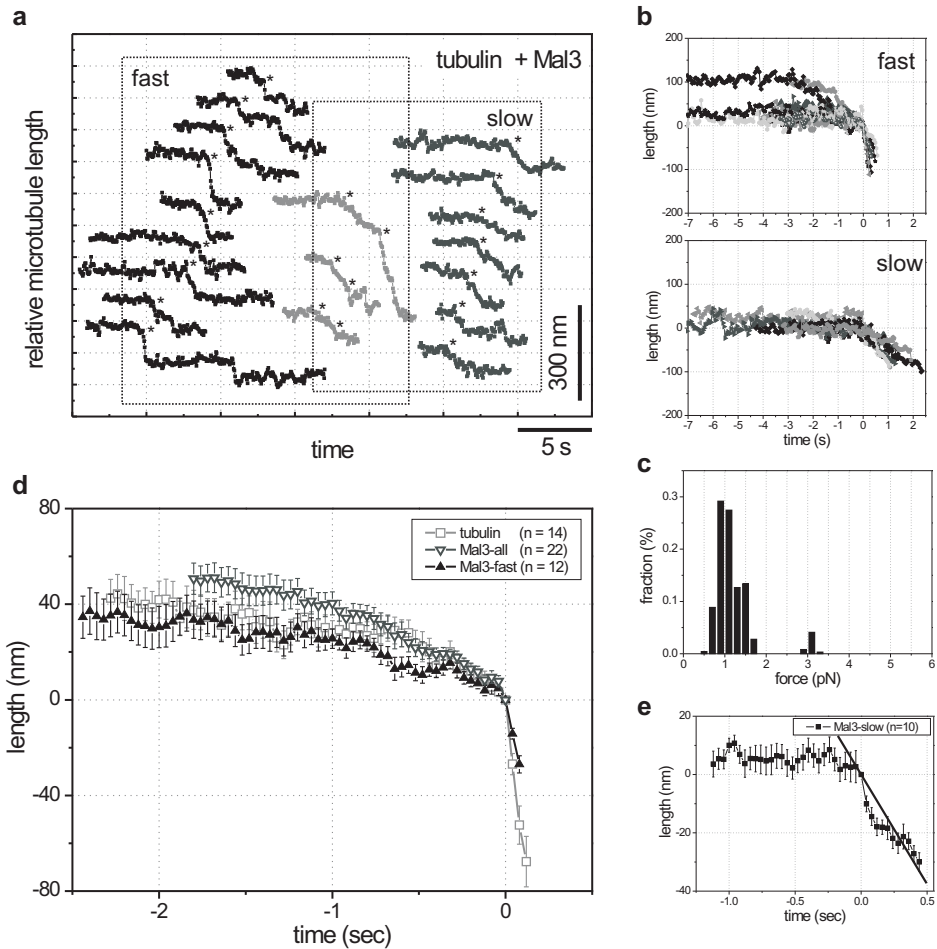


**Figure 6.4: Microtubule shrinkage in the presence of Mal3.** (a) Individual shrinking events of microtubules assembled in the presence of 20  $\mu\text{M}$  tubulin and 200 nM Mal3. Black traces comprise events of fast shrinkage and were aligned at the onset of shrinkage (indicated by asterisks). The aligned segments are shown in (b), top panel. Slow depolymerization events (gray) were aligned approximately at the beginning of the shrinking phase (asterisks). The aligned slow segments are shown in (b), lower panel. We also identified a couple of events comprising both slow and fast events, shown in light gray in (a). Asterisks indicate the onset of a slow or a fast disassembly phase. (c) Histogram of stall forces. The average force experienced by microtubules before a catastrophe was  $1.2 \pm 0.1$  pN (mean  $\pm$  s.e.m.). (d) Averaged events prior to microtubule fast shrinkage in the absence of Mal3 (open squares) (figure 6.2 d) and in the presence of Mal3 are plotted for comparison. Error bars represent s.e.m. The average events in the presence of Mal3 were determined from the aligned fast events (solid triangles) and from all events aligned in such a way that the slow depolymerization part overlapped (alignment point for the fast ones was the beginning of fast shrinkage, whereas the alignment point for the slow events was the end point of the slow shrinkage event) (open triangles). (e) Averaged event calculated from the aligned slow events in (b), lower panel. The alignment point was the beginning of the slow depolymerization. Error bars represent s.e.m. The slow depolymerization was characterized by a speed of  $4.5 \pm 0.2$   $\mu\text{m min}^{-1}$  as determined from a linear fit.

structure at the growing microtubule, as we rarely measure shrinkage events fully described by slow depolymerization in the absence of Mal3.

Our observations suggest that catastrophes involve loss of tubulin dimers or a conformational change at the microtubule end. As Mal3 recognizes the growing ends we could probably gain new information on the end-structure under force or prior to a fast disassembly event by monitoring the presence of Mal3 at the end, at the mentioned conditions. Prior *in vivo* experiments suggested that, when microtubules reach the cell cortex, Mal3 signal is lost from the microtubule end some time before shrinkage [109]. We also performed preliminary experiments *in vitro* where microtubules were grown against rigid barriers. The localization of fluorescent Mal3 at the tip was monitored. We observed similar behavior as *in vivo* (data not shown in this thesis). One possible explanation is that first, the end-structure depolymerizes or closes into a tube, hence the disappearing of the Mal3 from the tip, and subsequently, a second event triggers microtubule depolymerization. This event could be the loss of lateral contacts between protofilaments at the tip and might be the slow length decrease observed in our high-resolution measurements. Further experiments on the localization of fluorescent Mal3 at the tip before shrinkage and experiments with other +TIPs that affect the catastrophe rate would be necessary to better understand the molecular events underlying the transition from growth to shrinkage.

### ***Acknowledgements***

I thank Tim Noetzel, Kazuhisa Kinoshita and Tony Hyman for kindly providing the XMAP215 protein for us and Linda Sandblad for the kind gift of Mal3 protein.

---

## Discussion and future directions

*This thesis gives a high-resolution perspective on the process of microtubule assembly, in vitro, in the presence of regulators. The near molecular resolution was provided by our optical tweezers based techniques. The effect of two representative microtubule associated proteins, XMAP215 and Mal3, on microtubule dynamics and assembly was investigated.*

### 7.1 Discussion

Our goal was to investigate on a molecular scale what is the influence of regulators on microtubule dynamics and possibly identify the underlying mechanisms of regulation. Our optical tweezers based technique made this study possible because it allows us to follow microtubule assembly and disassembly with near molecular resolution while still preserving the dynamics of the process.

We found that XMAP215, a protein known to dramatically enhance microtubule growth, altered the molecular details accompanying microtubule assembly. Fast length increases, equivalent to 7-8 tubulin dimers, were measured in the presence of XMAP215. This suggests a mechanism of regulation based on local enhancement of tubulin addition, possibly along a single protofilament. The extent of the fast jumps during growth correlated with the length of XMAP215 protein itself, indicating possible mechanism of action at the growing tip: i) XMAP215 might promote elongation of a tubulin protofilament along its length or ii) XMAP215 could facilitate formation of long tubulin oligomers in solution. Another potential mechanism, recently proposed in ref. [27], is based on XMAP215 tracking growing ends: diffusion-facilitated end-tracking of XMAP215 ensures the presence of XMAP215 for a while at the growing tip, where it catalyzes addition of several tens of tubulin subunits.

We also investigated microtubule regulation by another class of proteins, the +TIPs. +TIPs are specialized in tracking the ends of dynamic microtubules and most of them are known to have a profound effect on microtubule dynamics. We focused our study on a complex of three +TIPs from fission yeast: the EB1 homologue Mal3, the kinesin Tea2 and the cargo Tip1. Preserving functionality of the end-tracking proteins is a crucial requirement when trying to understand how they regulate microtubule dynamics. Therefore, we first reconstituted the end-tracking behavior of the fission yeast complex *in vitro*. Strikingly, we found that Mal3 is an autonomous end-tracker. Mal3 seems to

recognize a specific structure at the ends of growing microtubules and does not need other proteins or post-translational modifications (e.g. phosphorylation) to achieve its function. In contrast, both Tea2 and Tip1 need Mal3 and each other to efficiently track growing microtubule plus-ends. This minimal system of three proteins is an example of the complex interactions in the +TIP network.

We next wondered whether a +TIP such as Mal3, due to its autonomous accumulation at the growing end, can individually regulate microtubule dynamics and if so, what is the molecular mechanism underlying Mal3 regulation. We could show that Mal3 affects all dynamic instability parameters. We measured enhanced microtubule growth, slower depolymerization and increased number of rescues and catastrophes in the presence of Mal3. This complex behavior correlates with Mal3 localization on microtubules and suggests that Mal3 acts differentially at the tip and on the microtubule lattice. One probable scenario is that Mal3 binding on the microtubules is dependent on the tubulin arrangement within the microtubule: at the lattice, most of the MAP binding sites are obscured by lateral contacts between protofilaments; at the seam, these binding sites are better accessible; and at the tip, the exposed protofilaments offer most optimal binding of Mal3. This model is consistent with Mal3 being primarily localized at the tip and moderately on the lattice. Based on its influence on microtubule dynamics we could also identify a possible molecular mechanism of regulation by Mal3. At the growing tip, the presence of Mal3 enhances the incorporation of tubulin subunits and alters the microtubule end in such a way that microtubules switch more often to a depolymerization phase, as compared to the absence of the protein. Using our high-resolution technique we also observed that Mal3 promotes formation of elongated end-structures, most probably representing incomplete microtubules. When present on the lattice, Mal3 hampers disassembly and promotes microtubule rescues. It is interesting to investigate whether this mechanism of regulation is conserved throughout the other homologs or other +TIPs that are able to autonomously end-track growing microtubule ends.

One intriguing aspect of microtubule dynamic instability is the switching event from growing to shrinkage, the catastrophe. Microtubule catastrophes are typically regulated by a large number of proteins. The principles of catastrophe regulation are currently not fully understood and whether there is a basic feature that associated proteins exploit to alter microtubule switching frequency remains to be clarified. At high-resolution, we observed a microtubule length decrease of several tens of nanometers prior to fast microtubule disassembly. This suggests the loss of a stabilizing structure. Two possible scenarios can be envisioned: either i) a stabilizing sheet-like structure at the microtubule end disassembles or ii) a cylinder configuration describing the end of a stalled microtubule opens by loss of lateral contacts between two or more protofilaments. It is possible that the events leading to a catastrophe comprise a sequence of both scenarios. MAPs could regulate both aspects involved in catastrophes. Mal3, for example, could be a MAP that affects first events in catastrophes by altering the

microtubule end-structure. Higher catastrophe rates were observed in the presence of XMAP215 as well, but we did not see an effect on the slow length decrease prior to shrinkage.

In conclusion we have investigated aspects of microtubule assembly and dynamics in the absence and in the presence of two microtubule associated protein systems. Our high-resolution technique combined with an *in vitro* approach allowed us to dissect the regulation by individual MAPs and identify possible mechanisms of regulation.

## 7.2 Future directions

Future directions of investigation naturally emerged from the experiments presented in this thesis. Here, I present three lines of investigations and our preliminary observations.

### 7.2.1 Regulation of microtubule dynamics by the plus-end tracking complex Mal3-Tea2-Tip1

Previous *in vivo* experiments in GFP-Mal3 fission yeast cells estimated that there is no correlation between the amount of Mal3 present at the microtubule tip and the microtubule growth speed [109]. In contrast, our *in vitro* experiments (chapter 5) show that Mal3 increases growth speed, which correlates with the amount of Mal3 present at the tip. This discrepancy might indicate that, *in vivo*, other +TIPs exert additional effects on microtubule growth.

From the *in vitro* reconstitution we identified that both Tea2 and Tip1 need each other and Mal3 to end-track. The presence of Mal3, which is autonomously tracking microtubule growing ends, influenced all dynamic instability aspects. We wondered what is the combined effect of the three +TIPs and whether the ternary complex can mimic *in vivo* microtubule dynamics.

We have investigated microtubule dynamic instability in the presence of various combinations of the three +TIPs, using both DIC microscopy and the high-resolution technique. Tea2-Tip1 complex seemed to reduce the effect of Mal3 at the microtubule tip. Table 7.1 summarizes the DIC measurements. The first part of the data are from experiments performed at an ionic strength similar to the experiments with Mal3 only (chapter 5). When the Tea2-Tip1 complex was added, we measured more stable microtubules (2.5-fold reduction in  $f_{\text{cat}}$ ) compared with the presence of Mal3 alone. The catastrophe frequency remained approximately 2-fold higher than the control (only tubulin present). The growth velocity was somewhat lower than in the presence of Mal3 only, but higher than in the control sample. Tea2-Tip1 background buffers did not seem to have any effect on microtubule dynamics. Therefore, the observed stabilizing effect on Mal3-regulation was due to the presence of the two proteins, Tea2-Tip1. We wondered whether the Tea2-Tip1 complex needed Mal3 to interfere with microtubule dynamics. In a set of experiments performed at higher ionic strength, we measured

salt (KCl)	Mal3 [nM]	Tea2 [nM]	Tip1 [nM]	buf	$v_{\text{gro}}$ ( $\mu\text{m}/\text{min}$ ) (n)	$f_{\text{cat}}$ ( $N_{\text{cat}}$ ) ( $\text{min}^{-1}$ )
55 mM	0	0	0	-	$1.2 \pm 0.1$ (14)	$0.08 (< 0.13)$ (8)
	0	0	0	+	$1.2 \pm 0.1$ (4)	$0.07 (< 0.15)$ (3)
	200	0	0	-	$1.8 \pm 0.1$ (17)	$0.30 \pm 0.06$ (23)
	200	50	50	+	$1.6 \pm 0.1$ (32)	$0.12 \pm 0.02$ (35)
70 mM	0	0	0	+	$1.4 \pm 0.2$ (2)	$0.17 (< 0.44)$ (2)
	0	500	200	+	$1.1 \pm 0.1$ (7)	$0.22 (< 0.38)$ (6)
	500	500	200	+	$1.3 \pm 0.1$ (6)	$0.14 (< 0.31)$ (3)
55 mM	0	0	0	+	$0.9 \pm 0.1$ (27)	$0.05 \pm 0.01$ (17)
	0	50	0	+	$0.8 \pm 0.1$ (33)	$0.04 \pm 0.01$ (18)
	200	0	0	+	$1.8 \pm 0.1$ (45)	$0.21 \pm 0.02$ (82)
	200	50	0	+	$2.2 \pm 0.1$ (33)	$0.17 \pm 0.02$ (49)

**Table 7.1: Dynamic instability parameters of microtubules in the absence and presence of +TIPs.** Microtubules were grown in the presence of  $15 \mu\text{M}$  (top and bottom part) and  $20 \mu\text{M}$  (middle part) tubulin at two different ionic strength conditions. Dynamic microtubules were imaged with DIC microscopy. Growth speeds were evaluated from linear fits on individual events. The average  $v_{\text{gro}}$  (mean  $\pm$  sem) was determined over the total number of events (n). The catastrophe frequency ( $f_{\text{cat}}$ ) was determined as the total number of catastrophes observed ( $N_{\text{cat}} \pm \sqrt{N_{\text{cat}}}$ ) divided by the total growth time. When  $N_{\text{cat}} \leq 8$  an upper bound was estimated [53].

growth speeds and catastrophe frequencies in a control sample, a sample with Tea2-Tip1 complex present and a sample where microtubules were grown in the presence of all three +TIPs. The measured values were similar in all three conditions showing that the presence of Mal3 is required for Tea2-Tip1 to exert their stabilizing effect. Tea2 alone did not seem to have an effect on the microtubule dynamics (lower part of the data in table 7.1). However, in the presence of Mal3, Tea2 had a weak stabilizing effect.

At high resolution, we also observed changes in the microtubule dynamic behavior in the presence of Tea2-Tip1, as compared with Mal3 sample (figure 7.1). Tea2 in the presence of Mal3 already suppressed the fast dynamics induced by Mal3. It is possible that the presence of Tea2 stabilizes the microtubule end-structure and fully closed microtubules can develop more often than in the presence of Mal3. Additional presence of Tip1 did not seem to further affect the plus-end dynamics. It is not clear why the two experiments, DIC and the optical tweezers measurements, do not correlate on the effect of Tea2 on microtubules. More experiments are required to elucidate the combined effect of +TIPs.

In conclusion, the effect of Mal3 on microtubule dynamics (increase in growth speed and catastrophe frequency) seemed to be reduced by Tip1. The extent of Tip1 stabilization does not seem to match the *in vivo* situation. Cells deleted for Tip1, Tea2 or Mal3 display very short and unstable microtubules. Tip1 is, most probably, no longer present at the microtubule growing ends in all three cases and the result indicates a potent stabilization by Tip1, which we do not measure to such extent *in vitro*. This suggest that *in*

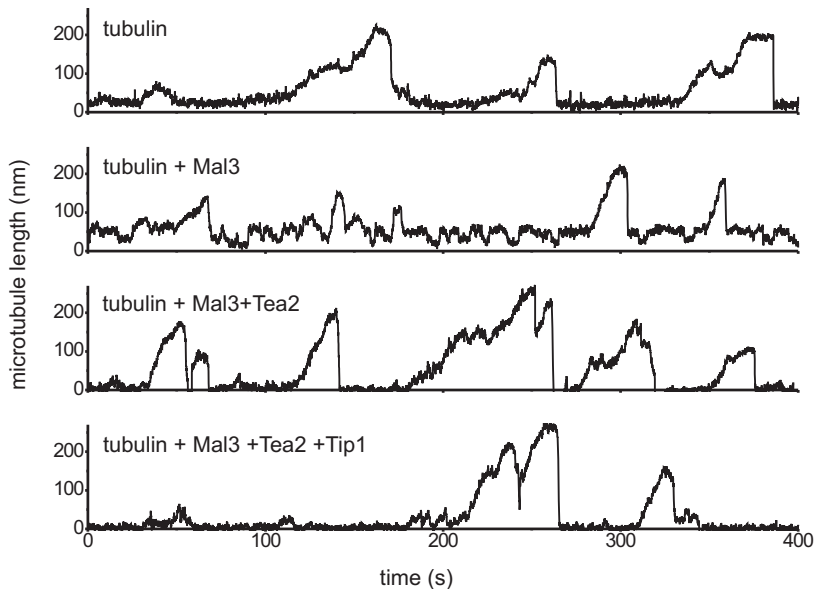


**Figure 7.1: Dynamic microtubules in the presence of Mal3, Tea2 and Tip1 measured with optical tweezers.** Microtubules were grown from 15  $\mu\text{M}$  tubulin at 25°C in the presence of various combinations of the fission yeast +TIPs, as indicated. Mal3 concentration was 500 nM in the experiment with Mal3 and Mal3-Tea2 present. In the experiment with all three proteins present, Mal3 was used at 100 nM. Tea2 concentration was 100 nM and Tip1 concentration was 40 nM.

*in vivo* there are yet other modulators and the ternary complex Mal3-Tea2-Tip1 does not fully describe microtubule regulation *in vivo*.

## 7.2.2 End-tracking of dynamic microtubules by EB proteins

**EB3 is an autonomous microtubule end-tracker.** We tested GFP-EB3 in our *in vitro* set-up (as described in chapter 4 and 5). GFP-tagged EB3 was a kind gift from S. Gouveia and A. Akhmanova. Remarkably the human EB3, similarly to the yeast homologue Mal3, showed autonomous microtubule end-tracking (figure 7.2 a). EB3 tracked both plus and minus growing ends, though with a preference for the plus-end. EB3 end-accumulation was not detected on shrinking microtubules. EB3 showed enhanced affinity for the microtubule growing end as compared with the lattice for a wide range of concentration. The interaction with microtubule lattice seemed to be inhibited, as we only observed a faint signal from the lattice for the range of concentration investigated. This observation suggests that there might be differences between the two homologs, EB3 and Mal3, in the details of the interaction with microtubules.

**EB3 C-tail is inhibiting lattice binding.** EB3 with C-tail deletion (EB3  $\Delta\text{C}$ -GFP) showed an enhanced affinity for the microtubule lattice (figure 7.2 b). When GFP was

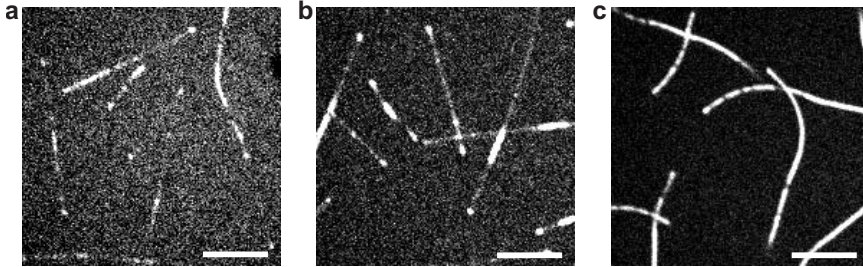


**Figure 7.2: EB3 end-tracks growing microtubules *in vitro*.** (a) Confocal micrograph of GFP-tagged EB3 (GFP at the protein N terminus) on dynamic microtubules. EB3 accumulation can be identified at the ends of growing microtubules. GFP-EB3 also bound to the short stable microtubules used as nucleation sites. (b) EB3  $\Delta$ C-GFP (EB3 lacking the C-terminus tail) signal on microtubules at 10-fold less concentration than in (a). (c) At high concentration (similar concentration with (a)), EB3  $\Delta$ C-GFP did bind with high affinity along the entire length of microtubules and altered their shape. Scale bars are 5  $\mu$ m.

attached to the C-terminus of the protein we also observed enhanced affinity of the EB3-GFP protein for the microtubule lattice as compared with the protein having the GFP fusion at the N-terminus. Though, the lattice binding was less extensive than for the C-tail deleted mutant. Microtubules grown in the presence of high amounts of EB3  $\Delta$ C-GFP displayed even higher signal on the lattice and microtubules mostly grew with a curved shape (figure 7.2 c). EB3 presence on the lattice might interfere with the seam closure and/or end-structure elongation. To understand this intriguing observation, more in depth investigations are necessary.

### 7.2.3 Influence of +TIPs on force generating microtubules

Force influences microtubule polymerization dynamics [70, 77]. Microtubules polymerizing against an opposing force grow slower and have more catastrophes. This regulation most probably occurs as well in living cells where microtubules often encounter boundaries. What is the effect of MAPs on the force generation by growing or shrinking microtubules is still unknown.

Our optical tweezers based technique allows us to evaluate the forces generated by growing microtubules. We analyzed microtubule growth events by binning the length vs time traces in short pieces (1-5 seconds) and evaluating, for each bin, an average force and growth speed. Figure 7.3 shows the individual growth speeds as a function of force in three conditions: (a) growth of microtubules from tubulin in the absence of any MAPs, (b) growth in the presence of Mal3 and (c) growth in the presence of XMAP215. We noticed that microtubules grown under force spent a large part of the time in a paused state or in a slow polymerization phase. We also noticed a decrease in the maximum speeds with increasing opposing force. If we compare the maximum growth speeds at different forces in the presence of the end-binding protein Mal3 with tubulin data, microtubules seem to slow down faster with force, while the presence of XMAP215



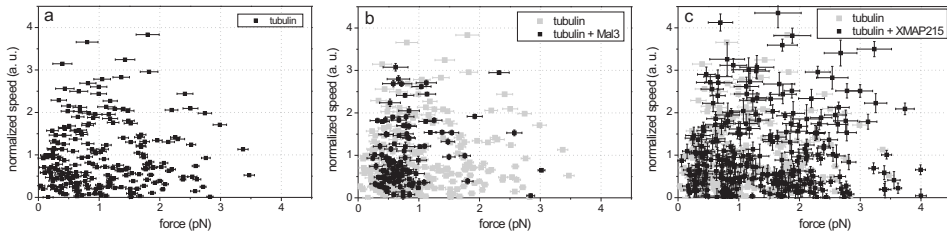


**Figure 7.3:** Microtubule growth speed as a function of the force against which the microtubules were growing. Data represent average speed and the corresponding average force of short data stretches: 5 s for the tubulin, 2 s for the Mal3 samples and 1 s for the data in the presence of XMAP215. The error bars represent s.d. The individual growth speeds are normalized with the average speed of growth in the force interval 0.5 to 1.0 pN.

reduced the force-induced slowing down of microtubules. A force-feedback set-up would be more appropriate when investigating difference in force-induced effect on microtubule assembly. This method would allow measurements of growth speeds at constant force for a large period of time providing sufficient data for an accurate estimation of both force and growth speed.

Another experimental complication is the presence of multiple microtubules. In these experiments we observe the growth of one to a couple of microtubules. When multiple microtubules are present they most probably share the force introducing artifacts in the force estimation. A better control of the nucleation from axonemes would improve the resolution of this method. This would allow us to construct force-velocity curves and analyze microtubule dynamics close to the stall force.

### ***Acknowledgements***

I would like to thank Liedewij Laan for help with experiments on Mal3-Tea2-Tip1. I would like to thank Susana Gouveia, Anna Akhmanova, Srinivas Honnappa and Michel Steinmetz for help with the experiments on EB3 proteins and for sharing the proteins with us.



---

# Bibliography

- [1] Wells WA (2005) The discovery of tubulin. *J Cell Biol* **169**:552.
- [2] Borisy GG, Taylor EW (1967) The mechanism of action of colchicine: Binding of colchicine-3H to cellular protein. *J Cell Biol* **34**:525–533.
- [3] Borisy GG, Taylor EW (1967) The mechanism of action of colchicine: Colchicine binding to sea urchin eggs and the mitotic apparatus. *J Cell Biol* **34**:535–548.
- [4] Erickson HP (1995) FtsZ, a prokaryotic homolog of tubulin? *Cell* **80**:367–370.
- [5] Schlieper D, Oliva MA, Andreu JM, Lowe J (2005) Structure of bacterial tubulin BtubA/B: Evidence for horizontal gene transfer. *Proc Natl Acad Sci* **102**:9170–9175.
- [6] Desai A, Mitchison TJ (1997) Microtubule polymerization dynamics. *Annu Rev Cell Dev Biol* **13**:83–117.
- [7] Kirschner M, Mitchison T (1986) Beyond self-assembly: from microtubules to morphogenesis. *Cell* **45**:329–342.
- [8] Mitchison T, Kirschner M (1984) Dynamic instability of microtubule growth. *Nature* **312**:237–242.
- [9] Heald R, Nogales E (2002) Microtubule dynamics. *J Cell Sci* **115**:3–4.
- [10] Cassimeris L (1999) Accessory protein regulation of microtubule dynamics throughout the cell cycle. *Curr Opin Cell Biol* **11**:134–141.
- [11] Howard J, Hyman AA (2007) Microtubule polymerases and depolymerases. *Curr Opin Cell Biol* **19**:31–35.
- [12] Akhmanova A, Steinmetz MO (2008) Tracking the ends: a dynamic protein network controls the fate of microtubule tips. *Nat Rev Mol Cell Biol* **9**:309–322.
- [13] Morrison EE (2007) Action and interactions at microtubule ends. *Cell Mol Life Sci* **64**:307–317.

- [14] Lansbergen G, Akhmanova A (2006) Microtubule plus end: a hub of cellular activities. *Traffic* **7**:499–507.
- [15] Wu X, Xiang X, Hammer JA III (2006) Motor proteins at the microtubule plus-end. *Trends Cell Biol* **16**:135–143.
- [16] Vaughan KT (2004) Surfing, regulating and capturing: are all microtubule-tip-tracking proteins created equal? *Trends Cell Biol* **14**:491–496.
- [17] Carvalho P, Tirnauer JS, Pellman D (2003) Surfing on microtubule ends. *Trends Cell Biol* **13**:229–237.
- [18] Galjart N, Perez F (2003) A plus-end raft to control microtubule dynamics and function. *Curr Opin Cell Biol* **15**:48–53.
- [19] Mimori-Kiyosue Y, Tsukita S (2003) 'Search-and-capture' of microtubules through plus-end-binding proteins (+TIPs). *J Biochem* **134**:321–326.
- [20] Schuyler SC, Pellman D (2001) Microtubule 'plus-end-tracking proteins': the end is just the beginning. *Cell* **105**:421–424.
- [21] Slep KC, Vale RD (2007) Structural basis of microtubule plus end tracking by XMAP215, CLIP-170, and EB1. *Mol Cell* **27**:976–991.
- [22] Akhmanova A, Hoogenraad CC (2005) Microtubule plus-end-tracking proteins: mechanisms and functions. *Curr Opin Cell Biol* **17**:47–54.
- [23] Wittmann T, Desai A (2005) Microtubule cytoskeleton: a new twist at the end. *Curr Biol* **15**:R126–R129.
- [24] Galjart N (2005) CLIPs and CLASPs and cellular dynamics. *Nat Rev Mol Cell Biol* **6**:487–498.
- [25] Sandblad L, Busch KE, Tittmann P, Gross H, Brunner D, Hoenger A (2006) The *Schizosaccharomyces pombe* EB1 homolog Mal3p binds and stabilizes the microtubule lattice seam. *Cell* **127**:1415–1424.
- [26] Helenius J, Brouhard G, Kalaidzidis Y, Diez S, Howard J (2006) The depolymerizing kinesin MCAK uses lattice diffusion to rapidly target microtubule ends. *Nature* **441**:115–119.
- [27] Brouhard GJ, Stear JH, Noetzel TL, Al-Bassam J, Kinoshita K, Harrison SC, Howard J, Hyman AA (2008) XMAP215 is a processive microtubule polymerase. *Cell* **132**:79–88.
- [28] Al-Bassam J, van Breugel M, Harrison SC, Hyman A (2006) Stu2p binds tubulin and undergoes an open-to-closed conformational change. *J Cell Biol* **172**:1009–1022.

- 
- [29] Folker ES, Baker BM, Goodson HV (2005) Interactions between CLIP-170, tubulin, and microtubules: implications for the mechanism of CLIP-170 plus-end tracking behavior. *Mol Biol Cell* **16**:5373–5384.
- [30] Dragestein KA, van Cappellen WA, van Haren J, Tsibidis GD, Akhmanova A, Knoch TA, Grosveld F, Galjart N (2008) Dynamic behavior of GFP-CLIP-170 reveals fast protein turnover on microtubule plus ends. *J Cell Biol* **180**:729–737.
- [31] Nogales E, Whittaker M, Milligan RA, Downing KH (1999) High-resolution model of the microtubule. *Cell* **96**:79–88.
- [32] Chrétien D, Wade RH (1991) New data on the microtubule surface lattice. *Biol Cell* **71**:161–174.
- [33] Chrétien D, Metoz F, Verde F, Karsenti E, Wade RH (1992) Lattice defects in microtubules: protofilament numbers vary within individual microtubules. *J Cell Biol* **117**:1031–1040.
- [34] Chrétien D, Fuller S, Karsenti E (1995) Structure of growing microtubule ends: two-dimensional sheets close into tubes at variable rates. *J Cell Biol* **129**:1311–1328.
- [35] Hammond JW, Cai D, Verhey KJ (2008) Tubulin modifications and their cellular functions. *Curr Opin Cell Biol* **20**:71–76.
- [36] Peris L, Thery M, Faure J, Saoudi Y, Lafanechere L, Chilton JK, Gordon-Weeks P, Galjart N, Bornens M, Wordeman L, et al. (2006) Tubulin tyrosination is a major factor affecting the recruitment of CAP-Gly proteins at microtubule plus ends. *J Cell Biol* **174**:839–849.
- [37] Reed NA, Cai D, Blasius TL, Jih GT, Meyhofer E, Gaertig J, Verhey KJ (2006) Microtubule acetylation promotes kinesin-1 binding and transport. *Curr Biol* **16**:2166–2172.
- [38] Ikegami K, Heier RL, Taruishi M, Takagi H, Mukai M, Shimma S, Taira S, Hatanaka K, Morone N, Yao I, et al. (2007) Loss of  $\alpha$ -tubulin polyglutamylation in ROSA22 mice is associated with abnormal targeting of KIF1A and modulated synaptic function. *Proc Natl Acad Sci* **104**:3213–3218.
- [39] Mandelkow E, Mandelkow E, Milligan R (1991) Microtubule dynamics and microtubule caps: a time-resolved cryo-electron microscopy study. *J Cell Biol* **114**:977–991.
- [40] Nogales E, Wang HW (2006) Structural intermediates in microtubule assembly and disassembly: how and why. *Curr Opin Cell Biol* **18**:179–184.

- [41] Browning H, Hackney DD, Nurse P (2003) Targeted movement of cell end factors in fission yeast. *Nat Cell Biol* **5**:812–818.
- [42] Gittes F, Mickey B, Nettleton J, Howard J (1993) Flexural rigidity of microtubules and actin filaments measured from thermal fluctuations in shape. *J Cell Biol* **120**:923–934.
- [43] Pampaloni F, Lattanzi G, Jonas A, Surrey T, Frey E, Florin EL (2006) Thermal fluctuations of grafted microtubules provide evidence of a length-dependent persistence length. *Proc Natl Acad Sci* **103**:10248–10253.
- [44] Janson ME, Dogterom M (2004) A bending mode analysis for growing microtubules: evidence for a velocity-dependent rigidity. *Biophys J* **87**:2723–2736.
- [45] Taute KM, Pampaloni F, Frey E, Florin EL (2008) Microtubule dynamics depart from the wormlike chain model. *Phys Rev Lett* **100**:028102.1–4.
- [46] Felgner H, Frank R, Schliwa M (1996) Flexural rigidity of microtubules measured with the use of optical tweezers. *J Cell Sci* **109**:509–516.
- [47] Felgner H, Frank R, Biernat J, Mandelkow EM, Mandelkow E, Ludin B, Matus A, Schliwa M (1997) Domains of neuronal microtubule-associated proteins and flexural rigidity of microtubules. *J Cell Biol* **138**:1067–1075.
- [48] Mickey B, Howard J (1995) Rigidity of microtubules is increased by stabilizing agents. *J Cell Biol* **130**:909–917.
- [49] Fygenon DK, Flyvbjerg H, Sneppen K, Libchaber A, Leibler S (1995) Spontaneous nucleation of microtubules. *Phys Rev E* **51**:5058–5063.
- [50] Wang HW, Long S, Rose FK, Nogales E (2005) Assembly of GMPCPP-bound tubulin into helical ribbons and tubes and effect of colchicine. *Cell Cycle* **4**:1157–1160.
- [51] Wang HW, Nogales E (2005) Nucleotide-dependent bending flexibility of tubulin regulates microtubule assembly. *Nature* **435**:911–915.
- [52] Wiese C, Zheng Y (2006) Microtubule nucleation:  $\gamma$ -tubulin and beyond. *J Cell Sci* **119**:4143–4153.
- [53] Particle Data Group (1990) Review of particle properties. *Phys Lett B* **239**:III.28–38.
- [54] Komarova YA, Vorobjev IA, Borisy GG (2002) Life cycle of MTs: persistent growth in the cell interior, asymmetric transition frequencies and effects of the cell boundary. *J Cell Sci* **115**:3527–3539.
- [55] Piehl M, Cassimeris L (2003) Organization and dynamics of growing microtubule plus ends during early mitosis. *Mol Biol Cell* **14**:916–925.

- 
- [56] Walker R, O'Brien E, Pryer N, Soboeiro M, Voter W, Erickson H, Salmon E (1988) Dynamic instability of individual microtubules analyzed by video light microscopy: rate constants and transition frequencies. *J Cell Biol* **107**:1437–1448.
- [57] Fyngenson DK, Braun E, Libchaber A (1994) Phase diagram of microtubules. *Phys Rev E* **50**:1579–1588.
- [58] Carlier MF, Hill TL, Chen YD (1984) Interference of GTP hydrolysis in the mechanism of microtubule assembly: an experimental study. *Proc Natl Acad Sci* **81**:771–775.
- [59] Hyman AA, Salser S, Drechsel DN, Unwin N, Mitchison TJ (1992) Role of GTP hydrolysis in microtubule dynamics: information from a slowly hydrolyzable analogue, GMPCPP. *Mol Biol Cell* **3**:1155–1167.
- [60] Caplow M, Ruhlen RL, Shanks J (1994) The free energy for hydrolysis of a microtubule-bound nucleotide triphosphate is near zero: all of the free energy for hydrolysis is stored in the microtubule lattice. *J Cell Biol* **127**:779–788.
- [61] Jánosi IM, Chrétien D, Flyvbjerg H (2002) Structural microtubule cap: stability, catastrophe, rescue, and third state. *Biophys J* **83**:1317–1330.
- [62] Molodtsov MI, Ermakova EA, Shnol EE, Grishchuk EL, McIntosh JR, Ataullakhanov FI (2005) A molecular-mechanical model of the microtubule. *Biophys J* **88**:3167–3179.
- [63] VanBuren V, Cassimeris L, Odde DJ (2005) Mechanochemical model of microtubule structure and self-assembly kinetics. *Biophys J* **89**:2911–2926.
- [64] Cassimeris L, Gard DL, Tran PT, Erickson HP (2001) XMAP215 is a long thin molecule that does not increase microtubule stiffness. *J Cell Sci* **114**:3025–3033.
- [65] Spittle C, Charrasse S, Larroque C, Cassimeris L (2000) The interaction of TOGp with microtubules and tubulin. *J Biol Chem* **275**:20748–20753.
- [66] Arnal I, Heichette C, Diamantopoulos GS, Chrétien D (2004) CLIP-170/tubulin-curved oligomers coassemble at microtubule ends and promote rescues. *Curr Biol* **14**:2086–2095.
- [67] Diamantopoulos GS, Perez F, Goodson HV, Batelier G, Melki R, Kreis TE, Rickard JE (1999) Dynamic localization of CLIP-170 to microtubule plus ends is coupled to microtubule assembly. *J Cell Biol* **144**:99–112.
- [68] Shirasu-Hiza M, Coughlin P, Mitchison T (2003) Identification of XMAP215 as a microtubule-destabilizing factor in *Xenopus* egg extract by biochemical purification. *J Cell Biol* **161**:349–358.

- [69] van Breugel M, Drechsel D, Hyman A (2003) Stu2p, the budding yeast member of the conserved Dis1/XMAP215 family of microtubule-associated proteins is a plus end-binding microtubule destabilizer. *J Cell Biol* **161**:359–369.
- [70] Dogterom M, Yurke B (1997) Measurement of the force-velocity relation for growing microtubules. *Science* **278**:856–860.
- [71] Grishchuk EL, Molodtsov MI, Ataulakhanov FI, McIntosh JR (2005) Force production by disassembling microtubules. *Nature* **438**:384–388.
- [72] Inoué S, Salmon ED (1995) Force generation by microtubule assembly/disassembly in mitosis and related movements. *Mol Biol Cell* **6**:1619–1640.
- [73] Dogterom M, Kerssemakers G, Jacob W J and Romet-Lemonne, Janson ME (2005) Force generation by dynamic microtubules. *Curr Opin Cell Biol* **17**:67–74.
- [74] Maiato H, DeLuca J, Salmon ED, Earnshaw WC (2004) The dynamic kinetochore-microtubule interface. *J Cell Sci* **117**:5461–5477.
- [75] Tran P, Marsh L, Doye V, Inoue S, Chang F (2001) A mechanism for nuclear positioning in fission yeast based on microtubule pushing. *J Cell Biol* **153**:397–412.
- [76] Janson ME, Dogterom M (2004) Scaling of microtubule force-velocity curves obtained at different tubulin concentrations. *Phys Rev Lett* **92**:248101.
- [77] Janson ME, de Dood ME, Dogterom M (2003) Dynamic instability of microtubules is regulated by force. *J Cell Biol* **161**:1029–1034.
- [78] Mogilner A, Oster G (1999) The polymerization ratchet model explains the force-velocity relation for growing microtubules. *Eur Biophys J* **28**:235–242.
- [79] van Doorn GS, Tanase C, Mulder BM, Dogterom M (2000) On the stall force for growing microtubules. *Eur Biophys J* **29**:2–6.
- [80] Stukalin EB, Kolomeisky AB (2004) Simple growth models of rigid multifilament biopolymers. *J Chem Phys* **121**:1097–1104.
- [81] Peskin CS, Odell GM, Oster GF (1993) Cellular motions and thermal fluctuations: the Brownian ratchet. *Biophys J* **65**:316–324.
- [82] Brangwynne CP, MacKintosh FC, Kumar S, Geisse NA, Talbot J, Mahadevan L, Parker KK, Ingber DE, Weitz DA (2006) Microtubules can bear enhanced compressive loads in living cells because of lateral reinforcement. *J Cell Biol* **173**:733–741.
- [83] Brangwynne CP, MacKintosh FC, Weitz DA (2007) Force fluctuations and polymerization dynamics of intracellular microtubules. *Proc Natl Acad Sci* **104**:16128–16133.



- 
- [84] Curmi PA, Andersen SSL, Lachkar S, Gavet O, Karsenti E, Knossow M, Sobel A (1997) The stathmin/tubulin interaction *in vitro*. *J Biol Chem* **272**:25029–25036.
- [85] Jourdain L, Curmi P, Sobel A, Pantaloni D, Carlier MF (1997) Stathmin: a tubulin-sequestering protein which forms a ternary T2S complex with two tubulin molecules. *Biochemistry* **36**:10817–10821.
- [86] McNally FJ, Vale RD (1993) Identification of katanin, an ATPase that severs and disassembles stable microtubules. *Cell* **75**:419–429.
- [87] Vale RD (2003) The molecular motor toolbox for intracellular transport. *Cell* **112**:467–480.
- [88] Caviston JP, Holzbaaur EL (2006) Microtubule motors at the intersection of trafficking and transport. *Trends Cell Biol* **16**:530–537.
- [89] Karsenti E, Vernos I (2001) The mitotic spindle: a self-made machine. *Science* **294**:543–547.
- [90] Dujardin DL, Vallee RB (2002) Dynein at the cortex. *Curr Opin Cell Biol* **14**:44–49.
- [91] Banks JD, Heald R (2001) Chromosome movement: dynein-out at the kinetochore. *Curr Biol* **11**:R128–R131.
- [92] Bringmann H, Skiniotis G, Spilker A, Kandels-Lewis S, Vernos I, Surrey T (2004) A kinesin-like motor inhibits microtubule dynamic instability. *Science* **303**:1519–1522.
- [93] Wordeman L (2005) Microtubule-depolymerizing kinesins. *Curr Opin Cell Biol* **17**:82–88.
- [94] Moores CA, Milligan RA (2006) Lucky 13 - microtubule depolymerisation by kinesin-13 motors. *J Cell Sci* **119**:3905–3913.
- [95] Walczak CE (2006) Kinesin-8s: motoring and depolymerizing. *Nat Cell Biol* **8**:903–905.
- [96] Martin SG, McDonald WH, Yates JR III, Chang F (2005) Tea4p links microtubule plus ends with the formin for3p in the establishment of cell polarity. *Dev Cell* **8**:479–491.
- [97] Grigoriev I, Montenegro Gouveia S, van der Vaart B, Demmers J, Smyth JT, Honnappa S, Splinter D, Steinmetz MO, Putney JW Jr, Hoogenraad CC, et al. (2008) STIM1 is a MT-plus-end-tracking protein involved in remodeling of the ER. *Curr Biol* **18**:177–182.
- [98] Adames NR, Cooper JA (2000) Microtubule interactions with the cell cortex causing nuclear movements in *Saccharomyces cerevisiae*. *J Cell Biol* **149**:863–874.

- [99] Drechsel DN, Kirschner MW (1994) The minimum GTP cap required to stabilize microtubules. *Curr Biol* **4**:1053–1061.
- [100] Vandecandelaere A, Brune M, Webb MR, Martin SR, Bayley PM (1999) Phosphate release during microtubule assembly: what stabilizes growing microtubules? *Biochemistry* **38**:8179–8188.
- [101] Voter WA, O'Brien ET, Erickson HP (1991) Dilution-induced disassembly of microtubules: relation to dynamic instability and the GTP cap. *Cell Motil Cytoskeleton* **18**:55–62.
- [102] Carvalho P, Gupta ML Jr, Hoyt MA, Pellman D (2004) Cell cycle control of kinesin-mediated transport of Bik1 (CLIP-170) regulates microtubule stability and dynein activation. *Dev Cell* **6**:815–829.
- [103] Busch KE, Hayles J, Nurse P, Brunner D (2004) Tea2p kinesin is involved in spatial microtubule organization by transporting Tip1p on microtubules. *Dev Cell* **6**:831–843.
- [104] Honnappa S, Okhrimenko O, Jaussi R, Jawhari H, Jelesarov I, Winkler FK, Steinmetz MO (2006) Key interaction modes of dynamic +TIP networks. *Mol Cell* **23**:663–671.
- [105] Weisbrich A, Honnappa S, Jaussi R, Okhrimenko O, Frey D, Jelesarov I, Akhmanova A, Steinmetz MO (2007) Structure-function relationship of CAP-Gly domains. *Nat Struct Mol Biol* **14**:959–967.
- [106] Komarova YA, Akhmanova AS, Kojima Si, Galjart N, Borisy GG (2002) Cytoplasmic linker proteins promote microtubule rescue in vivo. *J Cell Biol* **159**:589–599.
- [107] Brunner D, Nurse P (2000) CLIP170-like tip1p spatially organizes microtubular dynamics in fission yeast. *Cell* **102**:695–704.
- [108] Beinhauer JD, Hagan IM, Hegemann JH, Fleig U (1997) Mal3, the fission yeast homologue of the human APC-interacting protein EB1 is required for microtubule integrity and the maintenance of cell form. *J Cell Biol* **139**:717–728.
- [109] Busch KE, Brunner D (2004) The microtubule plus end-tracking proteins Mal3p and Tip1p cooperate for cell-end targeting of interphase microtubules. *Curr Biol* **14**:548–559.
- [110] Tirnauer JS, Grego S, Salmon E, Mitchison TJ (2002) EB1-microtubule interactions in *Xenopus* egg extracts: role of EB1 in microtubule stabilization and mechanisms of targeting to microtubules. *Mol Biol Cell* **13**:3614–3626.

- 
- [111] Manna T, Honnappa S, Steinmetz M, Wilson L (2008) Suppression of microtubule dynamic instability by the +TIP protein EB1 and its modulation by the CAP-Gly domain of p150<sup>Glued</sup>. *Biochemistry* **47**:779–786.
- [112] Ligon LA, Shelly SS, Tokito M, Holzbaur EL (2003) The microtubule plus-end proteins EB1 and dynactin have differential effects on microtubule polymerization. *Mol Biol Cell* **14**:1405–1417.
- [113] Tirnauer JS, O’Toole E, Berrueta L, Bierer BE, Pellman D (1999) Yeast Bim1p promotes the G1-specific dynamics of microtubules. *J Cell Biol* **145**:993–1007.
- [114] Rogers SL, Rogers GC, Sharp DJ, Vale RD (2002) Drosophila EB1 is important for proper assembly, dynamics, and positioning of the mitotic spindle. *J Cell Biol* **158**:873–884.
- [115] Varga V, Helenius J, Tanaka K, Hyman AA, Tanaka TU, Howard J (2006) Yeast kinesin-8 depolymerizes microtubules in a length-dependent manner. *Nat Cell Biol* **8**:957–962.
- [116] Gupta ML Jr, Carvalho P, Roof DM, Pellman D (2006) Plus end-specific depolymerase activity of Kip3, a kinesin-8 protein, explains its role in positioning the yeast mitotic spindle. *Nat Cell Biol* **8**:913–923.
- [117] Moore AT, Rankin KE, von Dassow G, Peris L, Wagenbach M, Ovechkina Y, Andrieux A, Job D, Wordeman L (2005) MCAK associates with the tips of polymerizing microtubules. *J Cell Biol* **169**:391–397.
- [118] Mennella V, Rogers GC, Rogers SL, Buster DW, Vale RD, Sharp DJ (2005) Functionally distinct kinesin-13 family members cooperate to regulate microtubule dynamics during interphase. *Nat Cell Biol* **7**:235–245.
- [119] Maddox PS, Stemple JK, Satterwhite L, Salmon ED, Bloom K (2003) The minus end-directed motor Kar3 is required for coupling dynamic microtubule plus ends to the cortical shmoo tip in budding yeast. *Curr Biol* **13**:1423–1428.
- [120] Gard DL, Becker BE, Romney SJ (2004) MAPping the eukaryotic tree of life: structure, function, and evolution of the MAP215/Dis1 family of microtubule-associated proteins. *Int Rev Cytol* **239**:179–272.
- [121] Gard DL, Kirschner MW (1987) A microtubule-associated protein from *Xenopus* eggs that specifically promotes assembly at the plus-end. *J Cell Biol* **105**:2203–2215.
- [122] Vasquez RJ, Gard DL, Cassimeris L (1994) XMAP from *Xenopus* eggs promotes rapid plus end assembly of microtubules and rapid microtubule polymer turnover. *J Cell Biol* **127**:985–993.

- [123] Al-Bassam J, Larsen NA, Hyman AA, Harrison SC (2007) Crystal structure of a TOG domain: conserved features of XMAP215/Dis1-family TOG domains and implications for tubulin binding. *Structure* **15**:355–362.
- [124] Bieling P, Laan L, Schek HT III, Munteanu EL, Sandblad L, Dogterom M, Brunner D, Surrey T (2007) Reconstitution of a microtubule plus-end tracking system in vitro. *Nature* **450**:1100–1105.
- [125] Hayashi I, Wilde A, Mal TK, Ikura M (2005) Structural basis for the activation of microtubule assembly by the EB1 and p150<sup>Glued</sup> complex. *Mol Cell* **19**:449–460.
- [126] Ashkin A (1997) Optical trapping and manipulation of neutral particles using lasers. *Proc Natl Acad Sci* **94**:4853–4860.
- [127] Svoboda K, Block SM (1994) Biological applications of optical forces. *Annu Rev Biophys Biomol Struct* **23**:247–285.
- [128] Svoboda K, Schmidt CF, Schnapp BJ, Block SM (1993) Direct observation of kinesin stepping by optical trapping interferometry. *Nature* **365**:721–727.
- [129] Visscher K, Schnitzer MJ, Block SM (1999) Single kinesin molecules studied with a molecular force clamp. *Nature* **400**:184–189.
- [130] Carter NJ, Cross RA (2005) Mechanics of the kinesin step. *Nature* **435**:308–312.
- [131] Valentine MT, Fordyce PM, Krzysiak TC, Gilbert SP, Block SM (2006) Individual dimers of the mitotic kinesin motor Eg5 step processively and support substantial loads *in vitro*. *Nat Cell Biol* **8**:470–476.
- [132] Mallik R, Carter BC, Lex SA, King SJ, Gross SP (2004) Cytoplasmic dynein functions as a gear in response to load. *Nature* **427**:649–652.
- [133] Gennerich A, Carter AP, Reck-Peterson SL, Vale RD (2007) Force-induced bidirectional stepping of cytoplasmic dynein. *Cell* **131**:952–965.
- [134] Finer JT, Simmons RM, Spudich JA (1994) Single myosin molecule mechanics: piconewton forces and nanometer steps. *Nature* **368**:113–119.
- [135] Molloy JE, Burns JE, Kendrick-Jones J, Tregear RT, White DCS (1995) Movement and force produced by a single myosin head. *Nature* **378**:209–212.
- [136] Davenport RJ, Wuite GJ, Landick R, Bustamante C (2000) Single-molecule study of transcriptional pausing and arrest by *E. coli* RNA Polymerase. *Science* **287**:2497–2500.
- [137] Wuite GJ, Smith SB, Young M, Keller D, Bustamante C (2000) Single-molecule studies of the effect of template tension on T7 DNA polymerase activity. *Nature* **404**:103–106.

- 
- [138] Noom MC, van den Broek B, van Mameren J, Wuite GJL (2007) Visualizing single DNA-bound proteins using DNA as a scanning probe. *Nat Meth* **4**:1031–1036.
- [139] Kellermayer MSZ, Smith SB, Granzier HL, Bustamante C (1997) Folding-unfolding transitions in single titin molecules characterized with laser tweezers. *Science* **276**:1112–1116.
- [140] Cecconi C, Shank EA, Bustamante C, Marqusee S (2005) Direct observation of the three-state folding of a single protein molecule. *Science* **309**:2057–2060.
- [141] Bechtluft P, van Leeuwen RGH, Tyreman M, Tomkiewicz D, Nouwen N, Tepper HL, Driessen AJM, Tans SJ (2007) Direct observation of chaperone-induced changes in a protein folding pathway. *Science* **318**:1458–1461.
- [142] Kerssemakers JWJ, Janson ME, van der Horst A, Dogterom M (2003) Optical trap setup for measuring microtubule pushing forces. *Appl Phys Lett* **83**:4441–4443.
- [143] Kerssemakers JWJ, Munteanu EL, Laan L, Noetzel TL, Janson ME, Dogterom M (2006) Assembly dynamics of microtubules at molecular resolution. *Nature* **442**:709–712.
- [144] Schek HT, Hunt AJ (2005) Micropatterned structures for studying the mechanics of biological polymers. *Biomed Microdevices* **7**:41–46.
- [145] Gibbons IR, Fronk E (1979) A latent adenosine triphosphatase form of dynein 1 from sea urchin sperm flagella. *J Biol Chem* **254**:187–196.
- [146] Pierce DW, Vale RD (1998) Assaying processive movement of kinesin by fluorescence microscopy. *Methods Enzymol* **298**:154–171.
- [147] Tselutin K, Seigneurin F, Blesbois E (1999) Comparison of cryoprotectants and methods of cryopreservation of fowl spermatozoa. *Poult Sci* **78**:586–590.
- [148] Nicastro D, Schwartz C, Pierson J, Gaudette R, Porter ME, McIntosh JR (2006) The molecular architecture of axonemes revealed by cryoelectron tomography. *Science* **313**:944–948.
- [149] Landau L, Lifshitz E (1986) Theory of elasticity, volume 7. New York: Pergamon.
- [150] Schek HT III, Gardner MK, Cheng J, Odde DJ, Hunt AJ (2007) Microtubule assembly dynamics at the nanoscale. *Curr Biol* **17**:1445–1455.
- [151] Laan L, Husson J, Munteanu EL, Kerssemakers JWJ, Dogterom M (2008) Force-generation and dynamic instability of microtubule bundles. *Proc Natl Acad Sci* :accepted.

- [152] Dogterom M, Husson J, Laan L, Munteanu EL, Tischer C (2007) Microtubule forces and organization. In: Lenz P, editor, *Cell Motility*, Springer New York. pp. 93–115.
- [153] Kinoshita K, Arnal I, Desai A, Drechsel DN, Hyman AA (2001) Reconstitution of physiological microtubule dynamics using purified components. *Science* **294**:1340–1343.
- [154] Jánosi IM, Chrétien D, Flyvbjerg H (1998) Modeling elastic properties of microtubule tips and walls. *Eur Biophys J* **27**:501–513.
- [155] Howard J, Hyman AA (2003) Dynamics and mechanics of the microtubule plus end. *Nature* **422**:753–758.
- [156] Carter BC, Vershinin M, Gross SP (2008) A comparison of step-detection methods: how well can you do? *Biophys J* **94**:306–319.
- [157] Popov AV, Pozniakovskiy A, Arnal I, Antony C, Ashford AJ, Kinoshita K, Tournebise R, Hyman AA, Karsenti E (2001) XMAP215 regulates microtubule dynamics through two distinct domains. *EMBO J* **20**:397–410.
- [158] Waterman-Storer CM, Desai A, Bulinski JC, Salmon ED (1998) Fluorescent speckle microscopy, a method to visualize the dynamics of protein assemblies in living cells. *Curr Biol* **8**:1227–1230.
- [159] Danuser G, Waterman-Storer CM (2006) Quantitative fluorescent speckle microscopy of cytoskeleton dynamics. *Annu Rev Biophys Biomol Struct* **35**:361–387.
- [160] Waterman-Storer CM, Salmon ED (1998) How microtubules get fluorescent speckles. *Biophys J* **75**:2059–2069.
- [161] Waterman-Storer CM, Salmon ED (1999) Fluorescent speckle microscopy of microtubules: how low can you go? *FASEB J* **13**:S225–S230.
- [162] Danuser G, M WSC (2003) Quantitative fluorescent speckle microscopy: where it came from and where it is going. *J Microsc* **211**:191–207.
- [163] Hess ST, Huang S, Heikal AA, Webb WW (2002) Biological and chemical applications of fluorescence correlation spectroscopy: a review. *Biochemistry* **41**:697–705.
- [164] Rigler R, Mets U, Widengren J, Kask P (1993) Fluorescence correlation spectroscopy with high count rate and low background: Analysis of translational diffusion. *Eur Biophys J* **22**:169–175.
- [165] Tirado MM, López Martínez C, García de la Torre J (1984) Comparison of theories for the translational and rotational diffusion coefficients of rod-like macromolecules. Application to short DNA fragments. *J Chem Phys* **81**:2045–2052.

- 
- [166] Magde D, Elson EL, Webb WW (1974) Fluorescence correlation spectroscopy. II. An experimental realization. *Biopolymers* **13**:29–61.
- [167] Hess ST, Webb WW (2002) Focal volume optics and experimental artifacts in confocal fluorescence correlation spectroscopy. *Biophys J* **83**:2300–2317.
- [168] Krouglova T, Vercammen J, Engelborghs Y (2004) Correct diffusion coefficients of proteins in fluorescence correlation spectroscopy. Application to tubulin oligomers induced by  $Mg^{2+}$  and paclitaxel. *Biophys J* **87**:2635–2646.
- [169] Meseth U, Wohland T, Rigler R, Vogel H (1999) Resolution of fluorescence correlation measurements. *Biophys J* **76**:1619–1631.
- [170] Gaskin F, Cantor CR, Shelanski ML (1974) Turbidimetric studies of the *in vitro* assembly and disassembly of porcine neurotubules. *J Mol Biol* **89**:737–755.
- [171] Perez F, Diamantopoulos GS, Stalder R, Kreis TE (1999) CLIP-170 highlights growing microtubule ends *in vivo*. *Cell* **96**:517–527.
- [172] Mimori-Kiyosue Y, Shiina N, Tsukita S (2000) Adenomatous polyposis coli (APC) protein moves along microtubules and concentrates at their growing ends in epithelial cells. *J Cell Biol* **148**:505–518.
- [173] Mimori-Kiyosue Y, Shiina N, Tsukita S (2000) The dynamic behavior of the APC-binding protein EB1 on the distal ends of microtubules. *Curr Biol* **10**:865–868.
- [174] Akhmanova A, Hoogenraad CC, Drabek K, Stepanova T, Dortland B, Verkerk T, Vermeulen W, Burgering BM, De Zeeuw CI, Grosveld F, et al. (2001) CLASPs are CLIP-115 and -170 associating proteins involved in the regional regulation of microtubule dynamics in motile fibroblasts. *Cell* **104**:923–935.
- [175] Vaughan PS, Miura P, Henderson M, Byrne B, Vaughan KT (2002) A role for regulated binding of p150<sup>Glued</sup> to microtubule plus ends in organelle transport. *J Cell Biol* **158**:305–319.
- [176] Kodama A, Karakesisoglou I, Wong E, Vaezi A, Fuchs E (2003) ACF7: an essential integrator of microtubule dynamics. *Cell* **115**:343–354.
- [177] Ding DQ, Chikashige Y, Haraguchi T, Hiraoka Y (1998) Oscillatory nuclear movement in fission yeast meiotic prophase is driven by astral microtubules, as revealed by continuous observation of chromosomes and microtubules in living cells. *J Cell Sci* **111**:701–712.
- [178] Hayles J, Nurse P (2001) A journey into space. *Nat Rev Mol Cell Biol* **2**:647–656.
- [179] Brunner D, Nurse P (2000) New concepts in fission yeast morphogenesis. *Phil Trans R Soc Lond B* **355**:873–877.

- [180] Browning H, Hayles J, Mata J, Aveline L, Nurse P, McIntosh JR (2000) Tea2p is a kinesin-like protein required to generate polarized growth in fission yeast. *J Cell Biol* **151**:15–28.
- [181] Browning H, Hackney DD (2005) The EB1 homolog Mal3 stimulates the ATPase of the kinesin Tea2 by recruiting it to the microtubule. *J Biol Chem* **280**:12299–12304.
- [182] West RR, Malmstrom T, Troxell CL, McIntosh JR (2001) Two related kinesins, klp5(+) and klp6(+), foster microtubule disassembly and are required for meiosis in fission yeast. *Mol Biol Cell* **12**:3919–3932.
- [183] Ohkura H, Garcia MA, Toda T (2001) Dis1/TOG universal microtubule adaptors - one MAP for all? *J Cell Sci* **114**:3805–3812.
- [184] Lata S, Piehler J (2005) Stable and functional immobilization of histidine-tagged proteins via multivalent chelator headgroups on a molecular poly(ethylene glycol) brush. *Anal Chem* **77**:1096–1105.
- [185] Tirnauer JS, Salmon ED, Mitchison TJ (2004) Microtubule plus-end dynamics in *Xenopus* egg extract spindles. *Mol Biol Cell* **15**:1776–1784.
- [186] Gildersleeve RE, Cross AR, Cullen KE, Fagen AP, Williams RC Jr (1992) Microtubules grow and shorten at intrinsically variable rates. *J Biol Chem* **267**:7995–8006.
- [187] Vitre B, Coquelle FM, Heichette C, Garnier C, Chretien D, Arnal I (2008) EB1 regulates microtubule dynamics and tubulin sheet closure *in vitro*. *Nat Cell Biol* **10**:415–421.
- [188] Moudjou M, Bornens M (1994) Isolation of centrosomes from cultured animal cells. In: Celis JE, editor, *Cell biology: A laboratory handbook*, Academic Press, Inc. pp. 595–604.
- [189] Tran PT, Walker RA, Salmon ED (1997) A metastable intermediate state of microtubule dynamic instability that differs significantly between plus and minus ends. *J Cell Biol* **138**:105–117.
- [190] Chrétien D, Fuller SD (2000) Microtubules switch occasionally into unfavorable configurations during elongation. *J Mol Biol* **298**:663–676.



---

## Summary

Cell division, internal cell organization, and intracellular transport rely on dynamic properties of microtubules. In cells, microtubule dynamics is highly regulated both spatially and temporally by a wide family of microtubule associated proteins (MAPs). In this thesis, an *in vitro* approach was used in order to shed light on the molecular details of the microtubule self-assembly process itself, as well as the molecular mechanism by which representative MAPs interact with and influence microtubule dynamics. The advantage of the *in vitro* minimal system is the possibility it offers to uncouple the regulation of different MAPs.

To zoom in with molecular resolution on the dynamic processes at the microtubule tip, we developed a high resolution technique that integrates optical tweezers, micro-fabricated rigid barriers and high-resolution video tracking of microbeads (described in chapter 2). In our experiments, microtubules are grown from a naturally occurring microtubule bundle, an axoneme, to which a polystyrene bead is attached near one end. The bead-axoneme construct is suspended in a 'keyhole' optical trap and positioned in front of a rigid barrier. The keyhole trap is used to control both the position of the bead and the direction of the axoneme. The rigid barriers are used to obstruct microtubule growth. Therefore microtubule elongation results in bead displacement. By detecting the position of the bead we can follow microtubule polymerization with near molecular resolution (~10 nm as compared with ~200 nm, the resolution of light microscopy). The experimental method, the special features of the optical trap, and considerations regarding microtubules in the context of our set-up are presented in chapter 2.

In chapter 3, molecular details of microtubule growth are discussed and how this process is altered, on a molecular scale, by the microtubule associated protein XMAP215 that is known to dramatically enhance the microtubule growth speed. We found that microtubule assembly is sometimes accompanied by fast length increases that correspond, in length, to 2-3 tubulin dimers. In the presence of XMAP215, we measured fast length increases equivalent to 7-8 tubulin dimers, corresponding to the size of the XMAP215 protein itself. These observations indicate that microtubule assembly might not always occur simply by the addition of individual tubulin dimers. Rather, small oligomers (2-3 dimers) seem to be able to attach to growing microtubules as well, an effect enhanced by the XMAP215 protein. XMAP215 might promote elongation of a tubulin protofilament along its length or could facilitate formation of long tubulin oligomers in

solution.

We also investigated another particular class of MAPs, the +TIPs, proteins that are specialized in tracking the microtubule dynamic ends. Their localization at the microtubule end enables direct regulation of microtubule dynamics. We focused our study on the complex of three fission yeast +TIPs: the EB1 homologue Mal3, the kinesin Tea2 and the cargo Tip1 (chapters 4 and 5). Preserving the protein functionality *in vitro* is a crucial requirement. Therefore, we first reconstituted *in vitro* the end-tracking behavior of the three proteins. From this experiment, presented in chapter 4, a hierarchy among the three +TIPs became clear. Mal3 is an autonomous end-tracker by recognizing a specific structure at the ends of growing microtubules. Tea2 and Tip1 need each other and Mal3 to efficiently track growing plus-ends: Mal3 acts as a loading factor on the microtubule for the Tea2-Tip1 complex and Tea2 motor activity ensures processive transport of the Tea2-Tip1 complex to the microtubule ends, where both proteins accumulate.

EB1 protein family members were shown to influence microtubule dynamics and organization *in vivo*, but it is still unclear whether the EB proteins solely have an effect on microtubule dynamics. As Mal3 is able to localize at microtubule growing ends independently of other proteins, we asked whether the EB1 homologue alone has an influence on microtubule dynamics. The results are presented in chapter 5. The experiments include three independent techniques: DIC microscopy to quantify the microtubule dynamic instability parameters in the presence of Mal3, fluorescence microscopy to quantify the Mal3 localization on microtubules, and the optical tweezers based technique to investigate the modifications induced by Mal3 at the microtubule dynamic tip. Mal3 had a complex effect on microtubules both at the lattice and at the tip. At the tip Mal3 bound efficiently and altered the end-structure in such a way that promoted tubulin dimer net addition and the chance for a microtubule to switch from a growing to a shrinking phase. Using the optical tweezers based technique we could identify microtubule end-structures that frequently disassembled before having the chance to close into a regular microtubule lattice. At the microtubule lattice Mal3 bound less potently than at the tip. The presence of Mal3 at the lattice hampered microtubule disassembly and promoted rescues. Our observations suggest a mechanism for Mal3-regulation based on local modification of the microtubule properties, which might be a reflection of the molecular mechanism underlying Mal3-microtubule interaction. Most probably, Mal3-tubulin binding sites are hidden within the lattice due to the protofilament lateral contacts and therefore, only occasional binding of Mal3 occurs at the lattice. At the seam, these binding sites are better accessible and at the tip, the exposed protofilaments offer most optimal binding of Mal3. This mechanism of regulation takes advantage of the complex architecture of the microtubule and enables proteins like Mal3 to act differentially at different locations on a dynamic microtubule.

Chapter 6 focuses on microtubule catastrophes, the transitions from a growing to a shrinkage phase. Knowledge about a mechanism for catastrophes has been limited to

---

models based on structural details of the microtubule ends imaged with cryo electron-microscopy. Information about how MAPs act on a molecular level to regulate catastrophes is even less extensive. Using our optical tweezers based technique, we observed a microtubule length decrease of several tens of nanometers prior to microtubule disassembly. This suggests the loss of a stabilizing structure. Two possible scenarios can be envisioned: either i) the sheet-like structure present at the growing end depolymerizes, leaving an exposed blunt end that is unstable and quickly collapses or ii) the stalled microtubule has a closed, cylinder configuration that becomes unstable only when the lateral contacts between two or more protofilaments are lost. This 'opening' of the cylinder would appear as a length decrease in our measurement. It is possible that the events leading to a catastrophe comprise a sequence of both scenarios. MAPs could regulate both aspects involved in catastrophes. Mal3, for example, could be a MAP that affects first events in catastrophes by altering the microtubule end-structure.

Chapter 7 describes future directions of investigation naturally emerging from the experiments presented in this thesis. (i) It is known that in living cells usually +TIPs interact with each other to affect microtubule dynamics. We performed preliminary experiments on microtubule dynamics regulation by the Mal3-Tea2-Tip1 complex. We found that Tea2-Tip1 need each other and Mal3, not only to localize at the microtubule ends, but also to regulate microtubule dynamics. We observed that Tip1 has a stabilizing effect by reducing the Mal3-enhanced catastrophe rate. (ii) We show that mammalian EB3, homologue of the fission yeast Mal3, is also an autonomous microtubule end-tracker *in vitro*. However, the details of EB3-microtubule interaction might be different and need further investigation. EB3, lacking the C-terminus tail, bound with high affinity to the microtubule lattice and promoted growth of intrinsically curved microtubules. (iii) The presence of MAPs might effect the forces generated by dynamic microtubules. In cells, microtubule pushing and pulling forces are constantly generated and constitute the driving forces for intracellular movement and transport of cellular components. Using the optical tweezers we measured microtubule force generation in the presence of the MAPs investigated here, XMAP215 and Mal3. Both proteins seemed to have an effect. The maximum forces generated by microtubules in the presence of Mal3 were lower than in the absence of the protein. With XMAP215 high forces were generated independently of the microtubule growth speed. More experiments are needed to confirm our first observations.

In conclusion we have investigated aspects of microtubule assembly and dynamics in the absence and in the presence of two representative microtubule associated protein systems. Our high-resolution technique combined with an *in vitro* approach allowed us to dissect the regulation of microtubule dynamics by individual MAPs and identify possible mechanisms of regulation.



---

# Samenvatting

De interne organisatie van de cel en fundamentele processen als celdeling en intracellulair transport zijn afhankelijk van de dynamische eigenschappen van microtubuli. In de cel wordt de dynamica van de microtubuli zowel in de tijd als in de ruimte gereguleerd door een scala aan microtubulus-geassocieerde eiwitten (MAPs). In dit proefschrift is een *in vitro* methode gebruikt om licht te werpen op de moleculaire details van zowel het zelf-assemblage-proces van microtubuli, als het mechanisme waarmee representatieve MAPs de microtubulusdynamica beïnvloeden. Het voordeel van een *in vitro* minimaal systeem is de mogelijkheid tot ont koppeling van de regulatie-effecten van de verschillende MAPs.

Om met moleculaire resolutie in te zoomen op de dynamische processen aan het uiteinde van de microtubuli, hebben we een hoge-resolutie techniek ontwikkeld, waarin een optisch pincet, micro-gefabriceerde wanden en hoge-resolutie 'video-tracking' van micro-bolletjes geïntegreerd zijn (beschreven in hoofdstuk 2). In onze experimenten groeien microtubuli vanuit een natuurlijke microtubulusbundel, een axoneem, waaraan een polystyreen bolletje is bevestigd aan een uiteinde. Het construct van axoneem en bolletje wordt vastgehouden in een optisch pincet met een 'sleutelgat'-profiel en gepositioneerd voor een wand. Het sleutelgatprofiel wordt gebruikt om zowel de positie van het bolletje als de richting van het axoneem te controlleren. De wand wordt gebruikt om een groeiende microtubulus tegen te houden, zodat lengtetoenames resulteren in een verplaatsing van het bolletje. Door de positie van het bolletje te bepalen kunnen we microtubuluspolymerisatie volgen met schier moleculaire resolutie (resolutie is ca. 10 nm, veel lager dan de ca. 200 nm resolutie van lichtmicroscopie). De experimentele methode, de specifieke eigenschappen van het optisch pincet, en beschouwingen betreffende microtubuli in de context van onze opstelling worden gepresenteerd in hoofdstuk 2.

In hoofdstuk 3 worden de moleculaire bijzonderheden van microtubulusgroei besproken en hoe deze processen op een moleculaire schaal beïnvloed worden door het microtubulus-geassocieerde eiwit XMAP215, waarvan bekend is dat het de groeisnelheid van microtubuli drastisch verhoogt. We hebben gevonden dat de assemblage van microtubuli soms vergezeld gaat van snelle toenames in lengte, die corresponderen met meerdere (2-3) tubuline-dimeren. In aanwezigheid van XMAP215 hebben we snelle lengtetoenames gemeten, die overeenkomen met 7-8 tubuline-dimeren, wat

correspondeert met de afmetingen van het XMAP215 eiwit zelf. Deze observaties wijzen erop dat de assemblage van microtubuli niet altijd simpelweg berust op de toevoeging van individuele tubuline-dimeren. Het lijkt er eerder op dat kleine oligomeren (2-3 tubuline-dimeren) ook aan de groeiende microtubuli kunnen binden, en dat dit effect versterkt wordt door het XMAP215-eiwit. XMAP215 zou langs zijn lengte de verlenging van een tubuline-protofilament kunnen bevorderen, of de formatie van lange tubuline-oligomeren in oplossing mogelijk kunnen maken. Deze scenario's, die gebaseerd zijn op een lokale verhoging van tubuline-additie (mogelijk langs een enkel protofilament), zouden meer algemene mechanismen kunnen zijn die aangewend worden door versterkers van microtubulusgroei.

Een andere specifieke klasse van MAPs zijn de +TIPs, die gespecialiseerd zijn in het volgen van de dynamische microtubuli-uiteinden. Hun positie aan het uiteinde van microtubuli maakt directe regulatie van de microtubulusdynamica mogelijk. We hebben onze studie gefocuseerd op het complex van drie +TIPs uit gistcellen (*S. pombe*): Mal3 (homoloog van EB1), kinesine Tea2 en de cargo Tip1 (hoofdstukken 4 en 5). Het behoud van de eiwitfunctionaliteit *in vitro* is een essentiële vereiste. Daarom hebben we eerst *in vitro* het gedrag (het volgen van het uiteinde) gereconstrueerd. Uit dit experiment (hoofdstuk 4) kwam een hiërarchie onder de drie +TIPs naar voren. Mal3 is een autonome eind-volger, die een specifieke structuur herkent aan het uiteinde van microtubuli. Mal3 treedt ook op als een 'loading factor' op de microtubuli voor het Tea2-Tip1-complex. De motoractiviteit van Tea2 garandeert processief transport van het Tea2-Tip1-complex naar de uiteinden van microtubuli, waar beide eiwitten accumuleren.

Het is bekend dat de leden van de EB1 eiwitfamilie invloed hebben op de dynamica en organisatie van microtubuli *in vivo*, maar het is nog onduidelijk of de EB-eiwitten een direct effect hebben op de dynamica van microtubuli. Aangezien Mal3 in staat is te lokaliseren aan het uiteinde van groeiende microtubuli, vroegen we ons af of dit EB-homoloog individueel een invloed heeft op de dynamica van microtubuli. De resultaten worden gepresenteerd in hoofdstuk 5. Er zijn drie onafhankelijke technieken gebruikt: DIC-microscopie om de parameters te bepalen van de dynamische instabiliteit van de microtubuli, fluorescentie-microscopie om te lokaliseren van Mal3 op de microtubuli te kwantificeren, en een techniek gebaseerd op een optisch pincet om de veranderingen te onderzoeken die door Mal3 aan het dynamische uiteinde van de microtubulus geïnduceerd worden. Mal3 heeft een complex effect op de microtubuli, zowel op het rooster, als op het uiteinde. Mal3 bindt efficiënt aan het uiteinde en verandert de eindstructuur op zo'n manier dat de netto toevoeging van tubuline-dimeren bevordert wordt, alsmede de kans dat een microtubulus schakelt van een groei- naar een krimp-fase. Mal3 bindt minder goed aan het microtubulusrooster dan aan het uiteinde. De aanwezigheid van Mal3 belemmert het uiteenvallen van de microtubuli en bevordert 'rescues'. Onze observaties suggereren een mechanisme van Mal3-regulatie dat gebaseerd is op de lokale verandering van de eigenschappen van de microtubulus, die

---

een weerspiegeling kunnen zijn van het moleculaire mechanisme dat ten grondslag ligt aan de interactie tussen Mal3 en de microtubulus. Hoogstwaarschijnlijk zijn de Mal3-tubuline-bindingsplaatsen verborgen binnen het rooster als gevolg van de laterale contacten tussen de protofilamenten en bindt Mal3 daarom slechts incidenteel aan het rooster. Op de naad zijn deze bindingsplaatsen beter toegankelijk en aan het uiteinde bieden de vrije protofilamenten de meest optimale bindingsplaatsen voor Mal3. Dit regulatiemechanisme maakt gebruik van de complexe architectuur van de microtubulus en maakt het mogelijk dat eiwitten zoals Mal3 een verschillende werking hebben op verschillende plaatsen op de microtubulus.

Hoofdstuk 6 concentreert zich op microtubulus-'catastrofes', de overgangen van groei naar krimp. Kennis van het mechanisme van de catastrofes is tot nu toe beperkt tot modellen die gebaseerd zijn op de structurele eigenschappen van de uiteinden van microtubuli zoals afgebeeld met *cryo-electron-microscopy*. Informatie over hoe MAPs op een moleculair niveau de catastrofes reguleren, is nog gelimiteerder. Met onze techniek, die gebaseerd is op het optisch pincet, konden we de dynamische uiteinden van de microtubuli volgen met bijna moleculaire resolutie. Wij namen een daling waar van de microtubuluslengte van tientallen nanometers voorafgaand aan het uiteenvallen van de microtubuli. Dit suggereert het verlies van een stabiliserende structuur. Twee mogelijke scenario's zijn hier: (i) de bladvormige structuur aan het groeiende uiteinde depolymeriseert, wat een stomp uiteinde oplevert, dat instabiel is en snel uiteenvalt, of (ii) de geblokkeerde microtubulus heeft de vorm van een cilinder die die pas instabiel wordt wanneer de laterale contacten tussen twee of meer protofilamenten worden verbroken. Dit 'openen' van de cilinder zou waargenomen kunnen worden als een lengtevermindering in onze meting. Het is mogelijk dat bij de gebeurtenissen die leiden tot een catastrofe beide scenario's een rol spelen. MAPs zouden beide aspecten van de catastrofes kunnen reguleren. Mal3 zou bijvoorbeeld een MAP kunnen zijn die de initiële gebeurtenissen van catastrofes beïnvloedt door de eindstructuur van de microtubulus te veranderen.

Toekomstige richtingen binnen dit onderzoek vloeien direct voort uit de experimenten die gepresenteerd worden in dit proefschrift (hoofdstuk 7). (i) Het is bekend dat in de cel +TIPs wisselwerkingen met elkaar kunnen hebben waardoor de assemblage van microtubuli beïnvloed wordt. We hebben voorbereidende experimenten uitgevoerd aan de regulatie van de microtubulusdynamica door het Mal3-Tea2-Tip1-complex. We hebben daarbij gevonden dat Tea2 en Tip1 elkaar en Mal3 niet alleen nodig hebben om te lokaliseren aan de uiteinden van microtubuli, maar ook om de dynamica van de microtubuli te reguleren. We hebben waargenomen dat Tip1 een stabiliserend effect had door het verlagen van de door Mal3 geïnduceerde catastrofe-rate. (ii) We laten zien dat ook EB3 (afkomstig van zoogdieren en een homoloog van Mal3) *in vitro* autonoom het uiteinde van microtubuli kan volgen. Maar de details van de interactie tussen EB3 en de microtubulus zijn mogelijk anders en vergen verder onderzoek. EB3 waarvan de C-terminale einde verwijderd is, bindt met hoge affiniteit aan het mi-

crotubulusrooster en bevordert de groei van intrinsiek gebogen microtubuli. (iii) De aanwezigheid van MAPs zou de krachten die door de microtubuli gegenereerd worden kunnen beïnvloeden. In de cel worden duw- en trekkrachten voortdurend gegenereerd door microtubuli en benut voor de intracellulaire verplaatsing en transport van andere cellulaire onderdelen. Met het optisch pincet hebben we de krachtgeneratie van microtubuli gemeten in de aanwezigheid van de hier besproken MAPs, XMAP215 en Mal3. Beide eiwitten lijken een effect te hebben. De maximale kracht die gegenereerd wordt door microtubuli in aanwezigheid van Mal3 was lager dan in afwezigheid van het eiwit. Met XMAP215 werden hoge krachten gegenereerd, onafhankelijk van de groeisnelheid. Er zijn meer experimenten nodig om onze eerste observaties te bevestigen.

Concluderend: we hebben aspecten onderzocht van de assemblage en dynamica van microtubuli in af- en aanwezigheid van twee representatieve microtubulus-geassocieerde eiwitsystemen. Onze hoge-resolutie-techniek in combinatie met een *in vitro* aanpak maakte het mogelijk om de regulatie door individuele MAPs te ontleden en mogelijke regulatiemechanismen te identificeren.



---

## Acknowledgements

My journey started almost 30 years ago and during this time I had the fortune to meet and interact with many inspiring and supportive people. They taught me a lot and are still doing it. I am grateful to each of you, who influenced my path in life and in science.

One of the people that inspired me early on was my high-school physics teacher, Gheorghe Burghilea. I would like to thank him, in memoriam, for giving me the credit of an equal when solving problems or discussing physics. Many thanks to my informatics teacher, Cătălin Tănase, who always believed in my potential. I would also like to acknowledge here the many mathematics teachers and olympiad fellows who inspired me and infected me with the love for solving problems and for logical reasoning.

During the first university years, I learned from Dumitru Luca that estimating experimental errors is as important as measuring the data. He also encouraged me to undertake my own research projects. Gheorghe Singurel introduced me to lasers and mentioned the potential of optical tweezers. I would like to thank him and the group of Kirstine Berg-Sørensen and Lene Oddershede for offering me the opportunity to actually work with optical tweezers at the Niels Bohr Institute in Copenhagen. It was truly great to be in such a place full of history. There, Iva Maria Tolic-Nørrelykke introduced me to 'real' experimental research. Thank you Iva, working with you was an unforgettable and fruitful experience.

With this starting base I came at AMOLF to the group of Marileen Dogterom. The Dogterom group felt like a big family and help was always at hand. Special thanks to Jacob Kerssemakers with whom I really enjoyed working. Your knowledge on optical tweezers and microtubules was indispensable. I will not forget your witty and sharp humor when things were not working and the sincere enthusiasm when the first results on the XMAP215 appeared on the monitor. I am really honored that, now, you will be at my side as *paranimf*. I owe many thanks to Guillaume who taught me how to grow dynamic microtubules, Gerbrand who was patient to show me several times how to measure a power spectrum, and Astrid who made laser alignment look like an easy task. Successful experiments always involve learning from our own mistakes, but the success is faster when trials are supplemented with good advice. I would like to thank all the present and past group members for all the ideas born during group meetings, in the lab or at the coffee corner. I am grateful to the above mentioned and, further, to Christian, Gertjan, Julien, Liedewij, Paige, Svenja, Nienke, Tatiana, Martijn, Marco C-L,

Andrea, and especially Marileen. Christian, I would like to thank you for our scientific and non-scientific discussions. I learned a great deal from them. Thank you for carefully reading the Mal3 chapter. And finally, thank you for getting me into climbing (I will come back to that). Liedewij, we had a lot of great moments anxiously watching the monitor in the confocal room. Although our ideas on the next best experiment were not always the same, often our stubbornness led to the right experiment. Julien, what a great cover! Thank you for cheering up the atmosphere in the basement with jazzy French music. Svenja, thank you for the comments on the Mal3 chapter. Paige, it is great to have you around in the lab. Thank you for sharing your kinesin and for correcting the introduction. Thanks also for taking care of my looks and for being a good friend.

The great thing about AMOLF is the multidisciplinary environment it offers. I also took advantage of it and I would like to thank a couple of people from other groups. Special thanks to Sander Tans and Thomas Kalkbrenner whose expertise on FCS allowed me to perform new and interesting experiments. Thomas, working with you was really instructive. Thank you for your clear explanations and your meticulous and organized way of dealing with experiments. I totally enjoyed it. Rimco, it was insightful to see how mass spectrometry works and what are the limitations when measuring native proteins. Suckjoon, experimenting with nucleoids was quite fun. Sorin, your endless knowledge on mathematics and noise was useful for me too. Thank you for making calculations look so simple and clear. I always enjoy talking to you about anything from science to life in a foreign place and in Romania. Rosalind, Kostya, Sanne, Simon, and Rhoda, your theoretical background gave me new perspectives on microtubules.

My work involved several collaborations outside AMOLF. I would like to thank Tim Noetzel, Kazuhisa Kinoshita and Tony Hyman for kindly providing us with the XMAP215 protein. Tim, thank you also for our discussions and for answering my numerous questions about XMAP215. Matthew Footer was so kind to purify several times axonemes for us and ship them to Amsterdam all the way from the Californian coast. I will not forget your advice on time planning of an experiment: the real time an experiment takes is double the initial estimation, but on the next time scale. The collaboration with the groups of Thomas Surrey and Damian Brunner was very successful. Such a big collaboration was a great opportunity for me to learn about new scientific areas and how to work in a big team. I would like to thank all the people in both groups for kindly sharing the yeast +TIPs with us. I would like to acknowledge Peter, discussing with you was always insightful, and Linda, I owe you thanks not only for all the information on Mal3, but also for the time spent with me imaging microtubules and axonemes using the cryo-EM. Many thanks to the groups of Anna Akhmanova and Michel Steinmetz that shared knowledge and EB proteins with us. I would like to especially thank Susana and Shrini for discussions and for purifying and labeling the proteins. Susana, I enjoyed a lot the time we spent together experimenting or talking during a nice dinner.

The little things that happen every day in the lab or outside are often forgotten, but

---

those little things have a great impact on a researcher's work. Therefore I would like to thank all the lab buddies that were always open for helping or sharing their tricks. Daan, Jerien and Aileen, thank you for giving up time on the ImageToolbox when I need it for my analysis. Many thanks for everybody from the technical support, design department, workshop, E&I, magazijn, library, and reception. Special thanks to Henk for keeping the microscope heating control alive, Duncan for developing electronics, and Marco K, Johan, Niels, Hans and Marco S for the many programs we needed to control the trap and analyze our data. I would like to also mention the people from the administration and human resource departments. Thanks to them I could spend more of my time on experiments and less on worrying about bank accounts, health insurance, residency and so on.

Siebe and Siri, thank you for your company and music, especially during the late nights of thesis writing. Siri's enchanting clarinet tunes made the deserted AMOLF a surreal place. Thank you for those great moments. I would like to thank Ana, Sanne, Marco M, Behnaz, Maria, Ioana and my office mates who were patient to listen to my plans and worries on writing during these last few months. Ana, thank you for the help with my text. Not only colleagues, but also my good old friends lent me their ears and supported me. Special thanks to my good friend and paranimf Ramona, your words and jokes made me laugh so often when I was stressed and your advice was always wise. Thank you.

And then, there is the climbing. A true passion. Not only I discovered that action on 'la verticale' makes me totally relaxed, but I also learned a great deal about how to manage long term goals. It might not be obvious, but the way to a Doctor degree is similar to the way to the top of a difficult climb. It requires determination, patience, technique, endurance and you never stop learning. Therefore I would like to thank all the climbers that taught me something and held the other end of the rope, and especially you, my dear climbing friends Christian, Paige, Elena, Bebas, Maria, Bas, Iza, and Lacramioara.

My final words are for the most special people in my life. First, my parents Elena and Emil, my sister Cristina and my grandma Moni. Vă mulțumesc pentru suportul și încrederea acordată 'micului geniu'. Niciodată nu ați pus la îndoială reușita în ceea ce fac. And Frank! Thank you for so many great, fun and lovely moments. Thank you for listening and supporting me. I greatly value your sharp, but kind social sense and your point of view often helped me to better manage the multiple situations I encountered during my research. Your humor is equally sharp and I totally enjoy our duels and recurring gags. No need to mention my appreciation for your help with the thesis, correcting parts of it and translating the samenvatting. And finally, I am definitely looking forward to our adventures in the States.

LAURA MUNTEANU  
Amsterdam, May 2008



---

## Curriculum vitae

Emilia Laura Munteanu was born in Comănești, Romania on December 8<sup>th</sup>, 1978. From 1993 to 1997 she attended the theoretical high-school 'Spiru-Haret' in Moinești. Subsequently, she studied Biophysics / Medical Physics at 'Alexandru Ioan Cuza' University in Iași. For her undergraduate project she worked on Monte Carlo numerical simulations to model light propagation in biological media under the supervision of Prof. dr. Gheorghe Singurel. Starting September 2001, she pursued a Masters degree in Biophysics at the University of Copenhagen, Denmark through an Erasmus exchange program. Her Masters research focused on the intracytoplasmic micro-rheology of living fission yeast cells. This work was in collaboration with Dr. Iva Maria Tolic-Nørrelykke in the Optical Tweezers group of Prof. dr. Kirstine Berg-Sørensen and Prof. dr. Lene Oddershede at the 'Niels Bohr' Institute. After she obtained the Masters degree Cand. Scient. for Biophysics in 2003, she maintained the position of research assistant for two months with the same group. Since September 2003 she has been a Ph. D. candidate in the Bio-Assembly and Organization group at AMOLF under the supervision of Prof. dr. Marileen Dogterom. The results of her research are presented in this thesis.



PROPOSITIONS (STELLINGEN)  
accompanying the thesis  
**Dynamics and regulation at the tip:**  
**A high resolution view on microtubule assembly**

1. The optical tweezers technique described in this thesis allows us to unravel molecular details of the microtubule assembly process and how this process is altered, on a molecular scale, by microtubule associated proteins (MAPs). (*chapters 3, 5, and 6*)
2. An *in vitro* approach is necessary when trying to understand the effect of individual MAPs on microtubule dynamics. (*chapters 3-5, see also proposition 4*)
3. Mal3 is an autonomous microtubule tip-tracker: it recognizes a specific structure at the growing microtubule end. (*chapters 4 and 5*)
4. Surprisingly, Mal3 enhances microtubule catastrophes *in vitro* (*chapter 5*), as opposed to the *in vivo* observation. In cells, microtubule dynamics are regulated by the combined action of several MAPs.
5. Most microtubule plus-end-tracking proteins (+TIPs) bind tubulin weakly. Weak interactions together with close proximity of multiple binding sites might be a prerequisite to achieve specificity on a dynamic structure.
6. Care should be taken when generalizing results found in one model organism. For example, the end-tracking behaviors of CLIP170 homologs in fission and budding yeast are different (Busch et al (2004) *Curr Biol* **14**, Carvalho et al (2004) *Dev Cell* **6**).
7. Simple models are proposed to explain complex behaviors (e.g. interaction between MAPs and microtubules). Their value lies in understanding the behavior as a first approximation, but they should not be considered as a full description.
8. Which came first: the question or the answer? Novel experiments often require re-definition of the question upon initial results.
9. "Climbing can be a state of consciousness where there are no distractions or expectations, just the challenge" (*Lynn Hill*). Science would also benefit from such an attitude.
10. Electricity turns into a survival need for the modern *Homo sapiens*.
11. Living in a foreign culture teaches genuine tolerance.
12. Sure, the journey to the summit is more important than reaching the summit. It is then that one becomes a better and more skilled person. But, the journey should not replace the summit as a goal.